VOLUME 34 – NO. 3 (Completing Vol. 34) AUGUST 1993 MONTHLY ISSN: 0304-3894

JOURNAL OF HAZARDOUS MATERIALS

ELSEVIER

JOURNAL OF HAZARDOUS MATERIALS

Management — Handling — Disposal — Risk Assessment

Review papers, normal papers, project reports and short communications are published dealing with all aspects of hazardous materials arising from their inherent chemical or physical properties. The scope of the journal is wide, ranging from basic aspects of preparation and handling to risk assessment and the presentation of case histories of incidents involving real hazards to employees or the public.

The following list, though not exhaustive, gives a general outline of the scope:

Properties: toxicity, corrosiveness, flammability, explosiveness, radioactivity, information data banks, dose–response relationships

Safety and health hazards: manufacturing, processing, transport, storage, disposal, major hazards and hazardous installations

Legislation: international, national and local codes of practice, threshold values, standards

Incidents: prevention, control, clean-up, communication, labelling, sources of information and assistance, case histories

Assessment: economic and general risk assessment, insurance, test methods, technical aspects of risk assessment of industrial hazards, reliability and consequence modelling, decision-making in risk management

Announcement from the Publisher

Elsevier Science Publishers encourages submission of articles on floppy disk.

All manuscripts may now be submitted on computer disk, with the eventual aim of reducing production times still further.

- The preferred storage medium is a 5¼ or 3½ inch disk in MS-DOS format, although other systems are welcome, e.g. Macintosh.
- After final acceptance, your disk plus one final, printed and exactly matching version (as a printout) should be submitted together to the editor. It is **important that the file on disk and the printout are identical**. Both will then be forwarded by the editor to Elsevier.
- Illustrations should be provided in the usual manner.
- Please follow the general instructions on style/arrangement and, in particular, the reference style of this journal as given in 'Instructions to Authors'.
- Please label the disk with your name, the software & hardware used and the name of the file to be processed.

Contact the Publisher for further information:

Elsevier
Journal of Hazardous Materials
P.O. Box 330
1000 AH Amsterdam, The Netherlands
Phone: (+31-20) 5862 758 Fax: (+31-20) 5862 459

ELSEVIER SCIENCE PUBLISHERS

711\414\140\079\03

Journal of Hazardous Materials, 34 (1993) 271–293
Elsevier Science Publishers B.V., Amsterdam

Removal of slightly heavy gases from a valley by crosswinds

Ian P. Castro[a,*], Ajay Kumar[b], William H. Snyder[c,**] and S. Pal S. Arya[d]

[a] *Department of Mechanical Engineering, University of Surrey, Guildford, GU2 5XH (England)*
[b] *Sirrine Environmental Consultants, Cary, NC 27511 (USA)*
[c] *Atmospheric Sciences Modeling Division, National Oceanic and Atmospheric Administration, Research Triangle Park, NC 27711 (USA)*
[d] *Department of Marine, Earth and Atmospheric Sciences, North Carolina State University, Raleigh, NC 27612 (USA)*

(Received September 17, 1992; accepted in revised form February 19, 1993)

Abstract

Wind tunnel experiments made to determine how rapidly dense gas is removed from a topographical depression by a crosswind are reported. The density and flow rate of the gas (input at the bottom of a V-shaped valley in otherwise homogeneous, flat terrain) were together sufficiently low to prevent pooling of the gas on the valley floor. In terms of the earlier and complimentary work of Briggs et al. (*J. Hazardous Mater.*, 24 (1990) 1–33), who considered only pooling cases, the present work concentrates on cases for which the relevant Richardson numbers ($Ri_0 = gH\Delta\rho/(\rho U_0^2)$) are relatively low. A simple theory is described, based on assumptions about the way in which the (slightly) heavy gas is removed by turbulent entrainment from the separated flow in the valley. For the steady state case, the theoretical result $C_0/C_s = \varepsilon V_0 (1 + \alpha Ri_0^n)$ is shown to fit the data quite well, where C_0/C_s is the ratio of the average valley concentration to the source gas concentration, V_0 is the dimensionless source flow rate and ε, α and n are constants. For the transient experiments, in which the source was suddenly removed and the decay of valley concentration was measured, the data are shown to be reasonably consistent with the theory, for both neutral and heavy gas releases: $-\ln(C') + \alpha Ri_0^n (1 - C'^n)/n = t'/\tau$, where $C' = C(t)/C_s$ and τ is a decay time constant. Although Reynolds number effects are shown to be significant in certain cases, the results provide a framework for estimating how long a heavy gas spill will take to disperse from depressions which are sufficiently steep-sided to embody regions of separation in windy conditions aloft.

* To whom correspondence should be addressed.
** On assignment to the Atmospheric Research and Exposure Assessment Laboratory, US Environmental Protection Agency, Research Triangle Park, NC 27711 (USA).

1. Introduction

Many of the accidental releases of toxic chemicals into the atmosphere or oceans involve material that is denser than the environment. The dispersion of such releases is consequently dependent, in part, on fluid dynamical parameters involving the density difference. In general, the rate of dispersion measured at, say, a specific location downwind of the release will be reduced as this density difference increases and this will be particularly true if the release occurs in a topographical depression. In the latter case it is clear that more energy will be required to extract the material from the depression than in the case of a neutrally stable release — simply because the potential energy gain required of the dense material is greater than it would otherwise be.

If enough dense material is released sufficiently quickly, it may actually collect at the bottom of the depression, decouple from the wind aloft and form a 'pool' of some vertical thickness before it is entrained and thence removed by a crosswind. The initial entrainment process is then dominated by the nature of the interface between the pool and the region above it. There is a considerable literature on the general problem of mixing between a lighter fluid moving over a heavier one (see, for example, the review by Christodoulou [2]). Recently, Briggs et al. [1] (hereafter BTS) have also conducted a series of experiments whose purpose was to determine how rapidly dense gas trapped in a valley could be removed by a crosswind. Their experiments concentrated on cases in which pooling of dense gas occurred and the entrainment was therefore 'interface dominated'. They undertook both steady experiments, in which the pool height remained fixed because of a balance between the heavy gas emission rate at the valley bottom and the entrainment rate across the interface, and transient experiments, in which effectively the source was removed and the pool height then decreased with time. These latter experiments were shown to confirm predictions based on the steady-state results.

BTS did not address the question of how the dispersion rate changes under conditions where there is no pool. They found that, in the transient experiments, once the pool height had reduced to zero there was a sudden increase in the rate of removal of gas from the valley, but the experiments were not designed to study this latter phase of the dispersion process. This increased removal rate was almost certainly caused by the fact that there was no longer a clearly distinguishable interface between heavy and light fluids so that entrainment from the valley was then dominated by the rate at which fluid could be removed from the top of the recirculating flow region (which largely filled the valley), rather than the rate at which it could be fed into the bottom of the recirculating region via entrainment across a density interface. It is this 'slightly dense' gas dispersion process that is addressed in this paper. We consider only cases in which there is no dense gas pool, so that the concentration of heavy gas is everywhere significantly less than the source value. In practice, this could arise in cases of small gas releases, releases of slightly dense material, releases in relatively windy conditions, or some combination of

these. Despite the lack of a pool, one still expects reductions in the dispersion rate (compared with the neutral case); from a practical perspective, the problem is likely to be equally important, particularly for more toxic releases, when even very small concentrations can be extremely hazardous.

The practical problem is always likely to be most severe when the geometry is such that the release is contained in or near a recirculating region of flow. This is most common in the context of releases near buildings and the question of how long removal takes from a recirculating building wake has been addressed previously, for the case of neutral releases (e.g. Hunt and Castro [3]). It was found in that case that the rate of decay of neutrally-buoyant emissions from within the wake could be described solely in terms of the geometrical size of the recirculating region and a typical upstream velocity; it was largely independent of the presence of strong mean swirling motions generated by some building shapes and orientations. This is in contrast to the behaviour well downstream of the recirculating wake, where concentration levels can depend crucially on such motions (as shown by, for example, Peterka and Cermak [4] in the context of buildings and Castro and Snyder [5] in the context of hills). To our knowledge no work has been done on the corresponding cases when the effluent is heavier than air.

In the experiments described in this paper we retain the simple geometrical features of the V-shaped valley used by BTS, recognising that this might be in some respects a 'worst case' topographical situation because of the recirculation which exists in the valley (although even worse cases might be those associated with perpendicular-sided valleys, like street canyons). The work is therefore an extension of the earlier experiment — indeed, the measurements were undertaken in the same wind tunnel and many features of the experimental procedure were identical. In the following section some simple theoretical ideas are described. These take as their basis ideas originally discussed by Humphries and Vincent [6] and later applied by Vincent [7], Hunt and Castro [3] and Fackrell [8] in the context of dispersion of passive materials in building wakes. Relationships are derived governing both the steady-state concentration at a typical location within the valley in terms of source flow rate and Richardson number, and the rate at which the concentration falls when the source is removed. The experimental procedures are summarised in Section 3 and Section 4 presents and discusses the major results. Conclusions and a typical application of the results are given in the final section.

2. Theoretical considerations

Figure 1 is a sketch of the flow geometry considered in this paper. A valley of width W (in the flow direction), length L (in the spanwise direction) and depth H is located in an otherwise homogeneous terrain across which there is an ambient wind $U(z)$. We assume throughout this work that L/W is sufficiently large that the flow can for practical purposes be considered two-dimensional;

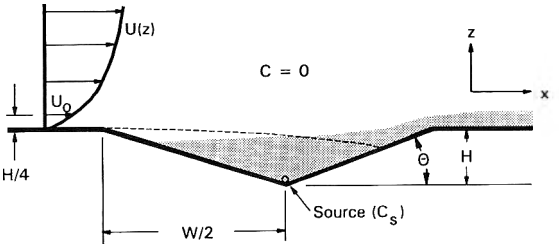

Fig. 1. Valley cross-section, definition sketch. Dotted line is postulated separation-reattachment streamline in (2D) neutral flow.

measurements (see Section 3) showed that even for L/W of only about 1.4, variations in mean concentration along a lateral line within the separation region varied by less than 10% within the central two-thirds of the span. Provided $H \gg z_0$, the roughness length of the upstream surface, the dynamics of the flow within the valley will not depend critically on z_0 and, if the valley sides are sufficiently steep, flow separation will occur near the upstream edge and the valley flow will be dominated by a large recirculation region. We imagine a source of gas at the bottom of the valley and therefore well within the recirculating flow. If the average volumetric concentration of the gas in the valley is C_0, then the volumetric flux, F, out of the valley will, on dimensional grounds, be given by:

$$F = k_1 A U_e C_0 \tag{1}$$

where k_1 is a constant and A is the area across which fluid is being entrained out of the valley at some average entrainment velocity, U_e. This argument is valid whether the flux is caused by turbulent transport or by direct advection or a mixture of the two processes. The constant k_1 represents the fact that the gas being extracted from the valley by entrainment will in general not have the same concentration as the valley-averaged value.

For a source of gas of concentration C_s and volumetric flow rate V_s/unit length, steady-state conditions require:

$$F = L V_s C_s = k_1 A U_e C_0, \tag{2}$$

where L is the valley cross-stream length, so that the steady state valley concentration can be expressed as:

$$C_0/C_s = (V_s/HU_e)/k_1 k_2, \tag{3}$$

in which the entrainment area, A, has been replaced by $k_2 HL$ (with k_2 depending on valley geometry). If the source is suddenly removed, the rate of change of the total quantity of gas, of average concentration C, in the valley is given by:

$$-\mathrm{d}(VC)/\mathrm{d}t = F = k_1 A U_e C, \tag{4}$$

where V is the volume of the valley.

In the case of a neutral gas release, the average entrainment velocity can be assumed, on dimensional grounds, to be some constant fraction of a typical velocity in the upstream flow, U_0, say (so that $U_e = k_3 U_0$). Then the steady-state concentration (C_0) is given from eq. (3) by:

$$C_0/C_s = V_0/(k_1 k_2 k_3), \tag{5}$$

where $V_0 = (V_s/HU_0)$ (and must clearly be less than $k_1 k_2 k_3$) and the variation of C with time after removal of the steady source is given from eq. (4) by:

$$-\ln(C/C_0) = (k_1 k_3/k_4)(tU_C/H), \tag{6}$$

in which the length scale, V/A, has been written as $k_4 H$, with, again, k_4 depending on valley geometry. C_0 is the initial value of C when the source is removed. (Note that eq. (5) can be written as $C_0 U_0 A/q = (k_1 k_2)^{-1} = \text{const.}$, with $q = C_s V_s L$, emphasising that for given source conditions and valley geometry, the steady concentration is inversely proportional to the upstream velocity.) Equation (6) suggests that the valley concentration will fall exponentially with time on removal of the source, at a non-dimensional rate dependent only on the constants, which depend on the particular valley geometry. In cases of neutral releases in recirculating building wakes, eq. (6) has been shown to describe the variation of wake concentration very well (e.g. Hunt and Castro [3]). There is no obvious reason why the above arguments should not hold equally well in the present case.

In the case of release of a (slightly) heavy gas, it is expected that the effective entrainment velocity, U_e, will depend on a Richardson number appropriate to the flow in the entrainment region. Assuming that this region can be characterised by some mixing layer of average thickness δ, a suitable Richardson number is given by $Ri = g(\Delta\rho/\rho_a)\delta/U_0^2$, where $\Delta\rho$ is an average density difference across the mixing region and ρ_a is the ambient air density. Recall that we are *not* considering the more extreme case in which there is a heavy gas pool, when the limiting entrainment process is at the pool interface, beneath the separated flow region. Here, we are assuming that the entrainment process is essentially the same as it is in the case of a neutral release, and therefore occurs largely in the mixing region just *above* the separated flow region but is somewhat damped by the nature of the density variation across the entrainment region. Density differences are related directly to gas concentrations and, assuming for the moment that the average valley concentration used earlier, C, can be taken as the value appropriate for the density ratio, Ri will be proportional to $(\gamma C_s g H/U_0^2)(\delta/H)(C/C_s)$, where γ is the factor relating the concentration to the density difference ($\gamma C_s = \Delta\rho_s/\rho_a$). A simple expression for the entrainment velocity might then be:

$$U_e/U_0 = k_3/\{1 + k_5[Ri_s(\delta/H)(C/C_s)]^n\}, \tag{7}$$

where $Ri_s = \gamma C_s g H/U_0^2$, a Richardson number appropriate to the source, and n and k_5 are constants. Note that $Ri_s = 1/Fr_0$, in the BTS terminology. Note also that with propane (or a propane/CO_2 mixture) as the source gas, which was the

case for all the heavy gas experiments, $\gamma C_s = (44-29)/29 = 0.52$. Equation (7) reduces to the relation used in the neutral case if $Ri_s = 0$ and implies a monotonic reduction in U_e as Ri_s rises. Use of this expression in eq. (3) leads to the steady-state result:

$$C_0/C_s = V_0[1 + k_5(Ri_0\delta/H)^n]/k_1k_2k_3, \tag{8}$$

and, in eq. (4), to the transient result:

$$-\ln(C') + (k_5/n)(Ri_0\delta/H)^n(1-C'^n) = (k_1k_3/k_4)t', \tag{9}$$

where $C' = C/C_0$, $t' = tU_0/H$ and $Ri_0 = Ri_sC_0/C_s$. Note that the arguments leading to these results for dense gas releases have ignored the possibility that some of the constants might, in fact, be functions of Ri. In deriving eq. (9) it has also been assumed that δ/H is constant with time.

With increasing Ri one would eventually expect some changes in the nature of the recirculating flow within the valley, which might lead to changes in k_1, k_2 and k_4 as well as in the average entrainment layer thickness, δ. Figure 14, discussed more fully in Section 5, shows that the steady-state concentration pattern within the valley for conditions near pooling is rather different from that for a neutral release. However, our experimental data will be analysed in terms of the above results on the basis that such effects will only be of second order, provided conditions near the valley bottom are not too close to pooling conditions. Regrouping constants and assuming $(\delta/H)^n$ is another constant allows eqs. (8) and (9) to be rewritten as:

$$C_0/C_s = \varepsilon V_0(1 + \alpha Ri_0^n) \tag{10}$$

and

$$-\ln(C') + \alpha Ri_0^n(1-C'^n)/n = t'/\tau, \tag{11}$$

respectively, where $\tau = k_4/(k_1k_3)$ (a non-dimensional time constant), $\varepsilon = 1/(k_1k_2k_3)$ and $\alpha = k_5(\delta/H)^n$. Neutral-release steady-state and transient experiments allow ε and τ, respectively, to be determined and heavy gas release experiments can then be used to see, first, whether steady-state conditions are modelled adequately by eq. (10) with appropriate values of α and n and then, second, whether or not (with the same constants) eq. (11) describes the transient behaviour. Equations (10) and (11) constitute the principal theoretical results of the present work.

Finally, it should be emphasised again that these results have all been obtained on the assumption that there is no heavy gas pooling in the valley. At a given windspeed, the source rate required to begin the pooling state will be a function only of Ri_s and, presumably, a Reynolds number — $Re_0 = U_0H/\nu$, say. In pooling cases, one of the implications of the data presented by BTS (who used the same valleys) is that for the limit of zero pool height,

$$V_0Ri_s = c(1 + 0.46/Re_f), \tag{12}$$

where c is a constant (0.00048) and $Re_f = (H/W)V_0 Re_0/Ri_s$. ($V_0 Ri_s = V'$ in the notation of BTS). Note that this is an extrapolation beyond the valid limit of the BTS data. Some initial experiments to determine the pooling criterion, in terms of the lowest tunnel speed required to prevent pool formation for a given source flow rate, will be compared with this result later. Note, however, that in the limit of zero wind speed, the above relationship fails, for it predicts that a pool will occur at *any* finite flow rate, whereas one expects that laminar diffusion will prevent a pool if the source rate is low enough. In that case, one could argue that, since vertical diffusion will occur across a layer of thickness d, say, pooling will begin when this thickness is such that the surface area (W', per unit spanwise length) of the top of the diffusing layer is just insufficient to allow enough total diffusion ($W'\kappa C_s/d$, where κ is the molecular diffusivity) to balance the input source rate ($V_s C_s$). For the triangular valley of the present case, $2d/W' = \tan\theta$, where θ is the valley side-wall slope, so that pooling will begin when

$$V_s = V_p = 2\kappa/\tan\theta. \tag{13}$$

3. Experimental procedures

All experiments were conducted in the Meteorological Wind Tunnel of the EPA Fluid Modeling Facility, fully described by Snyder [9]. The valley models were sunk into the floor of the wind tunnel and had the dimensions given in Table 1, with most measurements made using the larger of the two models. They did not span the entire working section, but steady-state measurements of concentration along a lateral line within the separation region showed variations within $\pm 10\%$ over the central two-thirds of the span. Two-dimensionality was always better in cases of heavy gas releases. The boundary layer used for all experiments was identical with that used by BTS and was developed over a rough surface comprising a homogeneous layer of stones (commercially known as Sanspray) with a mean diameter of about 1 cm. A tripping fence, 15.3 cm in height, was located 65 cm downstream from the test section entrance. This configuration lead to velocity and turbulence profiles, shown in

TABLE 1

Dimensions of valley models

Valley	Length (m) (crosswind)	Width (m) (along wind)	Depth (m)	Wall slope (°)
Large	2.0	1.4	0.254	20
Small	1.0	0.7	0.140	22

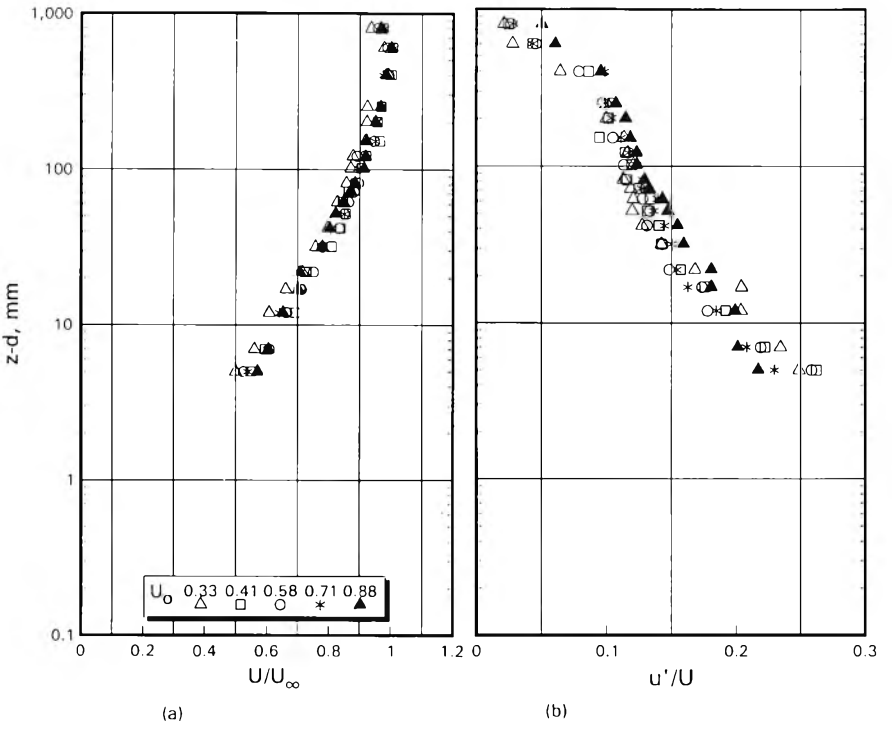

Fig. 2. Characteristics of upstream boundary layer. (a) Mean velocity profiles. (b) Turbulence intensity profiles.

Fig. 2, typical of a neutral atmospheric boundary layer. The roughness length, z_0, was in the range 0.05–0.15 mm which, at a scale of 1 : 1000 (based on the wind tunnel boundary layer depth of about 0.6 m and a typical full scale value of about 600 m), corresponds to a rural terrain with $z_0 = 5$–15 cm.

Low wind speeds were necessary for many of the experiments, although not as low as in some of the pooling experiments of BTS since, in the present case, lower Richardson numbers were generally required. Most experiments were undertaken at four ambient wind-tunnel speeds, corresponding to (nominal) U_0 values of 0.33, 0.58, 0.82 and 1.12 m/s. Since it is particularly difficult to measure velocities around 0.5 m/s or lower, uncertainties in the lowest reference velocity may be as high as $\pm 10\%$. As in the earlier experiments of BTS, the reference velocity, U_0, was taken throughout as the value at $z = H/4$, on the basis that this is more representative of the velocity field near the top of the valley and that in the recirculating flow within the valley than is the free-stream velocity.

The source-gas mixture was introduced into the valley through a perforated tube, laid spanwise along the valley floor. Source-gas flow rates were always sufficiently small to imply a negligible effect on the flow field within the valley. Even the maximum value of V_s, around 60,000 cm^3/min, implies a local injection

velocity over the 4 cm by 200 cm region just above the pipe of less than $0.04U_0$. In the transient experiments, a vacuum pump was switched into the line simultaneously with the supply being removed. A small volume of gas was thus removed from the valley but this procedure ensured that no further gas leaked into the valley. Mixtures of carbon dioxide (CO_2) and propane (C_3H_8) were used as the source in the heavy gas experiments. The propane was included as a tracer, with concentrations determined by drawing ambient samples through a rake of sampling tubes (2.4 mm o.d.) and passing these samples through hydrocarbon measurement systems (Beckman, model 400 flame ionisation detectors — FID's). The system response time was about one second, which was small enough to be acceptable even in the transient experiments, where typical valley 'flushing' times exceeded 20 seconds. For the neutral release experiments ethane (C_2H_6) was used as the tracer. The analysers have a linear response over a very wide dynamic range and were frequently calibrated with air and a 0.9% ethane mixture. Flow rates of each gas were measured and monitored using Meriam laminar flow elements, with a Brooks flow calibrator used to determine the set points for given pressure drops across them. In the transient runs the 'zero' points of the FID's were reset at the background concentration in the tunnel, which was measured frequently. Measured concentrations in all propane experiments were multiplied by a calibration factor of 0.745 (since ethane was used for analyser calibrations).

The output from each FID was digitised at typically 1–10 Hz and collected by a personal computer. Sampling durations were typically two minutes in the steady-state cases and up to about four minutes in the transient cases. Concentration measurements were generally found to be repeatable to within $\pm 5\%$.

In most experiments concentrations were measured simultaneously at five points within the valley, with sampling tubes mounted either on the three-directional traverse gear in the tunnel or through holes in the valley surface. It was found, not surprisingly, that the largest concentrations invariably occurred near the upwind wall of the valley; this location is deep within the separated flow region and consequently, when the source is removed, it is in this region that the concentration falls most slowly. In the transient experiments, the concentration was therefore measured at five points distributed on the valley upwind surface along a spanwise line about halfway up the valley. With the coordinate system shown in Fig. 1, the five points were at y-positions of 0, ± 0.35 and ± 0.74 (normalised by the valley half-length, $L/2$). In view of the large variability in any single realisation of concentration vs. time, the procedure employed by Hunt and Castro [3] was used. Each transient experiment was repeated 10–20 times, with the concentration at every measurement point then being ensemble-averaged. Figure 3 presents a typical result; variations of $C(t)/C_0$ are shown for each of the five sample locations, with $t=0$ being the time at which the source gas is shut off. Notice that the behaviour is largely independent of spanwise location and that after about 80 seconds, by which time the concentrations have fallen to 10% of their initial values, the

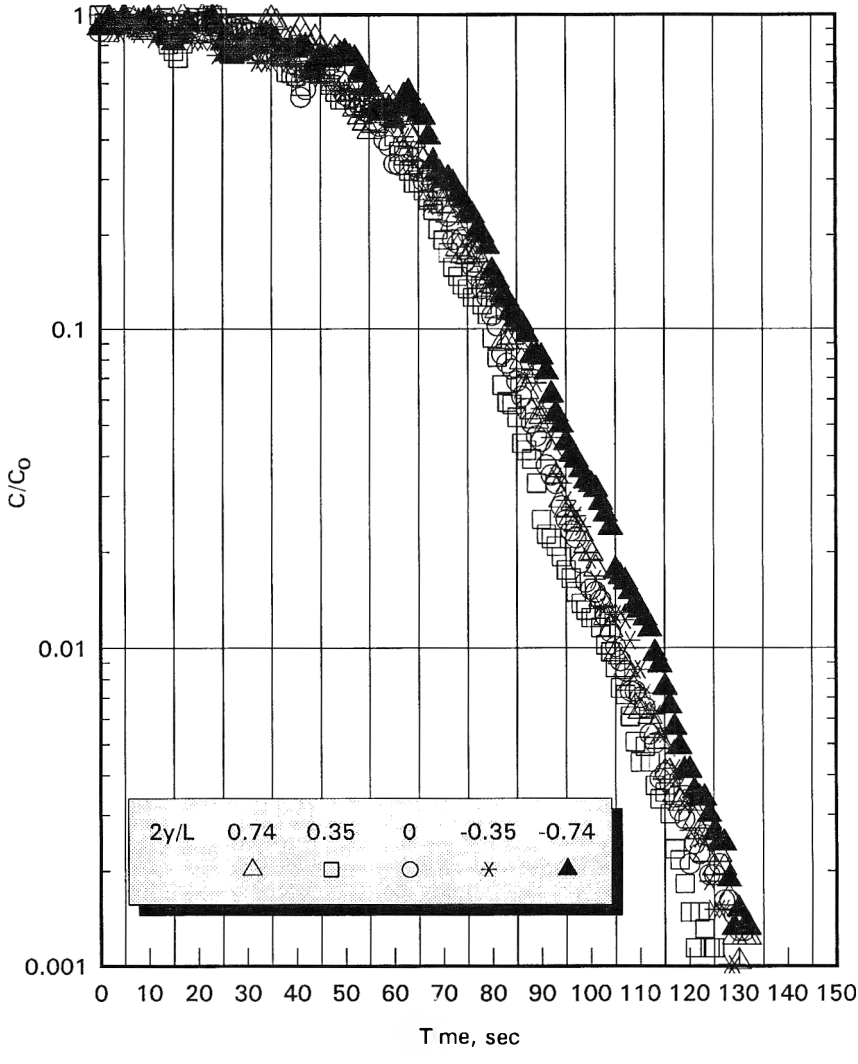

Fig. 3. Concentration decay of heavy gas at different spanwise locations in the large valley. $x = -380$ mm, $z = -105$ mm, $Ri_s = 11.9$.

fall-off in concentration is essentially exponential, as expected on the basis of the ideas discussed in Section 2 (e.g., eq. 9). In all the transient results presented later, data from these five spanwise points were averaged together to reduce the variability even further and, on the basis that three-dimensional effects were not significant, in determining the transient behaviour.

4. Experimental results and discussion

4.1 Pooling limits

Since the primary aim of the work was to study cases in which pooling did not occur, we began by determining, for a typical range of input source rates, the critical tunnel velocity at which pooling just began. Here, pooling is defined as the condition wherein heavy gas within the valley effectively decouples from the wind aloft, so that the heavy-gas concentration at the bottom of the valley equals the source concentration. As explained earlier, entrainment is thereafter (at lower tunnel speeds for the fixed source rate) limited by the processes at the interface between the dense gas pool and the flow above.

Sampling tubes were positioned both inside the source tube and just above it and the steady-state ratios of the two measured concentrations were obtained for fixed source flow rates and gradually increasing tunnel speed. The results are shown in Fig. 4. Figure 5a shows the resulting critical velocity, U_{0c}, taken as the velocity at which the concentration ratio is 0.95, as a function of V_s, the

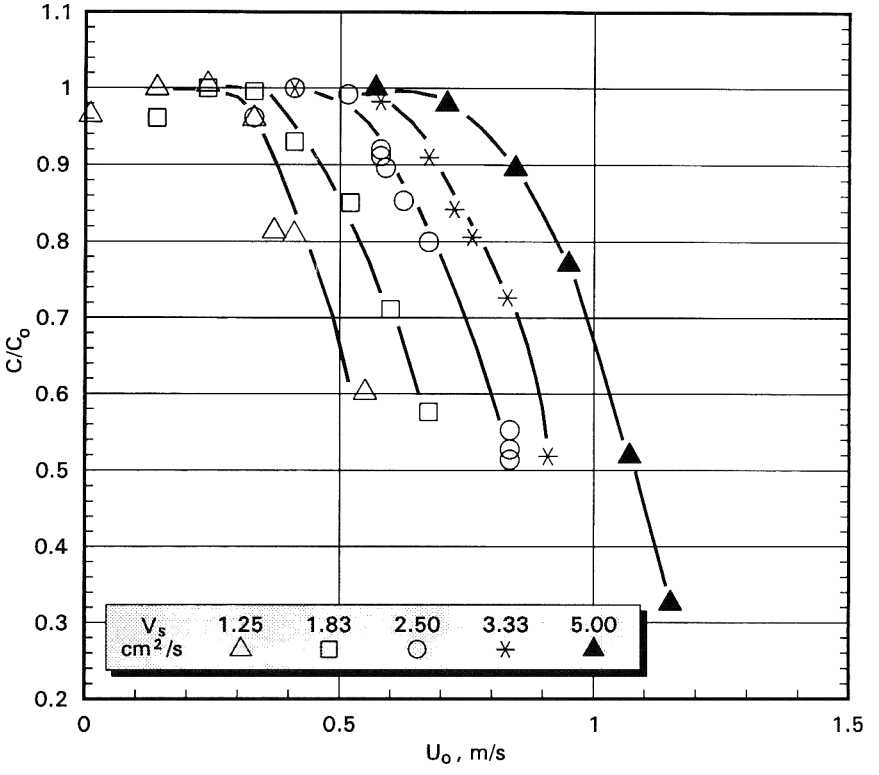

Fig. 4. Pooling condition in the large valley. Pooling begins when C/C_s reaches 0.95 as U_0 falls.

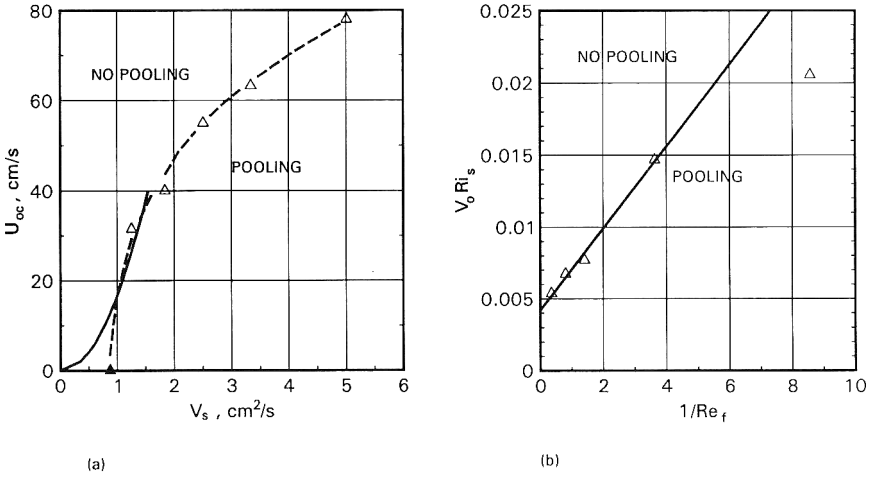

Fig. 5. Critical velocity for pooling conditions. (a) Dimensional plot. (▲) is from eq. (13). Solid line is low Re_f limit (eq. 14). (b) Non-dimensional plot. Solid line is eq. (14).

source flow rate. These results are replotted in Fig. 5b as $V_0\,Ri_s$ vs. $1/Re_f$ and it is evident that, apart from the lowest Re_f result, the pooling condition satisfies the form of eq. (12) quite well, that is,

$$V' = V_0 Ri_s = 0.0042(1 + 0.68/Re_f). \tag{14}$$

Note that although the constant 0.68 is not too far from the BTS value of 0.46, the other constant is larger by a factor of around nine. However, the arguments leading to eq. (12) were developed for cases in which the pool height, z_p, was large enough to ensure an interface fetch sufficiently long that entrainment was limited by the heaviness of the entrained fluid. The BTS work did not cover cases for which $z_p < 0.2H$ and the constant, c, in eq. (12) was obtained by extrapolating a curve of z_p vs. $V'^{1/3}$ to the case of zero pool height, giving $V'^{1/3} = 0.08$ for $z_p = 0$. As noted earlier, this is an extrapolation beyond the valid limits of the BTS result. The present data imply $V'^{1/3} = 0.16$, which is a factor of two higher than the BTS result; it should be emphasised that the physical processes determining when pooling begins ($z_p = 0$) may well be different from those describing the entrainment process for $z_p > 0.2$. None the less, one expects the pooling limit (V_0) to be a function only of Ri_s and Re_0, which is certainly confirmed by our data.

Note also that the low Re_f limit of eq. (14) can be expressed as $V_s^2 = 0.0029 W U_0 \nu$; this is included in Fig. 5a but, although it has the physically correct form for situations in which the entrainment is dominated by molecular processes (i.e. $Re_f \ll 1$, as discussed in BTS), it clearly is not correct for U_0 near zero. In that case, using $\kappa = 0.159$ cm²/s (for CO_2 in air), eq. (13) gives a pooling flow rate of about $V_s = 0.875$ cm²/s for the large valley. This result is

also included in Fig. 5a and is not inconsistent with an extrapolation of the data for small U_0.

4.2 Neutral releases

An initial series of experiments was undertaken in both valleys using ethane. Steady-state conditions were set up first and average concentrations (from the five sampling points, as discussed in Section 3) were obtained, before removing the source and obtaining concentrations as a function of time. Figure 6 shows C_0, the steady-state concentration, plotted against V_0. In the absence of Reynolds number effects one would expect a linear relationship, with a slope which would depend on the valley slopes and on the particular locations of the sample tubes. It is seen that the results are a reasonable fit to straight lines except those obtained at the lowest tunnel speed (U_0 values in brackets), which lie somewhat lower. Since the results are ensemble averages of very many measurements, these two points cannot be explained away on the basis of statistical scatter and we must conclude that Reynolds number effects were not entirely negligible at these very low tunnel velocities. Molecular diffusion is expected to make a significant contribution to the total dispersion, so one might expect a lower concentration at a given V_0; this is in line with the result in Fig. 6. The data suggest that ε (in eq. (10), with $Ri_0=0$ for neutral releases) has the value 16.7 for the large valley, if the lowest Reynolds number result is ignored. This latter data point implies the rather lower value of $\varepsilon=11.8$. Corresponding values for the small valley are some 30% higher; this must be due to the geometrical differences between the valleys (the small valley was proportionately deeper than the large one) and/or the differences in parameters like z_0/H and δ/H. We would expect increases in the latter parameters to cause a reduction in the valley concentration, which is the reverse of what the data indicate, so conclude that geometrical effects were probably dominant. These may have included small differences in the relative locations of the sampling tubes in the two cases.

Figure 7 shows the results of the corresponding transient runs for the large valley case. Concentrations have been normalised by the appropriate C_0 values and in each case it is clear that after an initial delay the decay rate is closely exponential. Denoting t_d as the time required for a fall in $C(t)$ of a factor of ten in this exponential region, Fig. 8a shows $1/t_d$ as a function of U_0; we again expect this to be linear in the absence of Reynolds number effects. At the lowest tunnel speeds the large valley results appear to deviate a little from linearity — this deviation might be expected, since even if one could force $U_0=0$ as soon as the source gas were removed, the ethane would gradually disperse via molecular diffusion, so that $1/t_d$ must remain non-zero for $U_0=0$. However, the small valley data do not show the same deviations. Figure 8b shows a plot of the dimensionless time constant, $\tau=U_0t_d/[H\cdot\ln(10)]$, against Reynolds number, U_0H/ν. (t_d is the time for a one-decade fall in concentration.) The plot includes data from the transient dense gas releases in the large valley, obtained by fitting straight lines through the low concentration regions

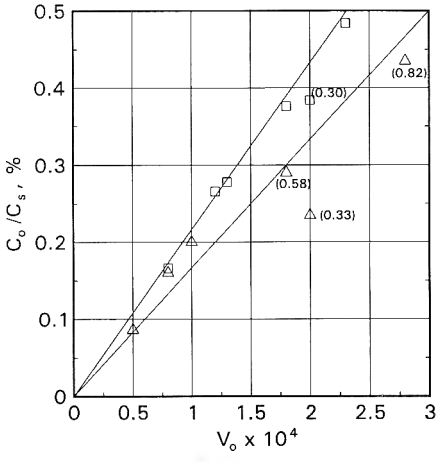

Fig. 6. Steady-state concentration versus source rate for neutral releases. (△) large valley, and (□) small valley. U_0 values shown in parentheses (m/s).

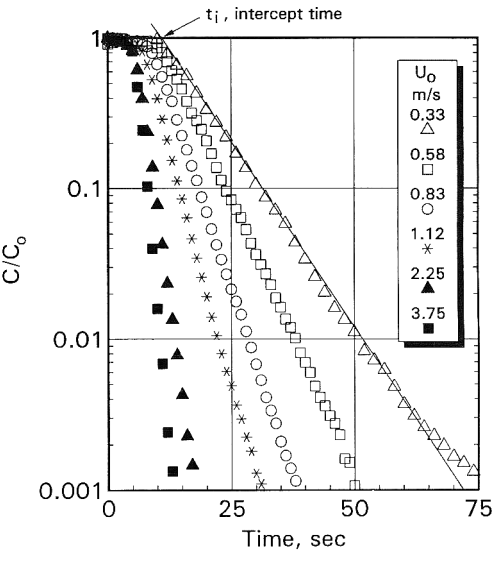

Fig. 7. Concentration decay for neutral releases at various U_0. (Large valley data.)

($C/C_0 \ll 1$), where the gas behaves as a passive release. A Reynolds number effect in the case of the large valley is only marginally evident above the scatter. The data suggest an average decay time constant, τ, of about 14.5.

These data (Figs. 6 and 8) are generally consistent with the theoretical arguments outlined in Section 2. Note that there is some inevitable uncertainty about when $C(t)$ first begins to fall. The gas samples take a few seconds to travel down the tubes to the FID's and, further, the concentration at the sample positions will not instantaneously follow those just above the source. Figure 9 shows the intercept time, t_i (see Fig. 7), as a function of $1/U_0$. The data are rather scattered, particularly in the large valley case, but are consistent with a 'sampling tube travel time', t_t, (i.e. t_i at $1/U_0 = 0$) of about 4.8 seconds. Provided the vacuum pumps drawing the samples through the system are reasonably stable, this travel time should be largely independent of any other experimental conditions. The distance between the source and the sampling position, divided by the (linear) slope through the data points in Fig. 9, is equivalent to a normalised 'advection' velocity, U_a/U_0; the results suggest $U_a/U_0 = 0.14$ and 0.41 in the large and small valley cases, respectively. These seem to be reasonable results but it should be emphasised that the advection velocity should more properly be thought of as a turbulent transport velocity, since the sampling position is on the surface, deep inside the recirculating region, where actual mean velocities are very low. (At the surface, of course, they are zero.) Note that the larger value (0.41) found for the small valley is

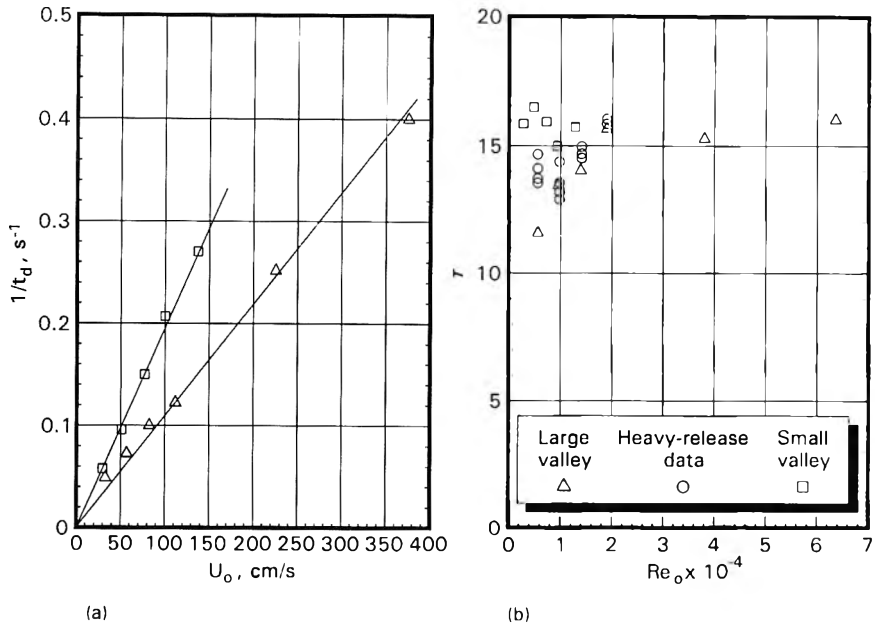

Fig. 8. Time constants of concentration decay for neutral releases. (a) One-decade decay time versus U_0. (b) Normalised time constant versus Re_0.

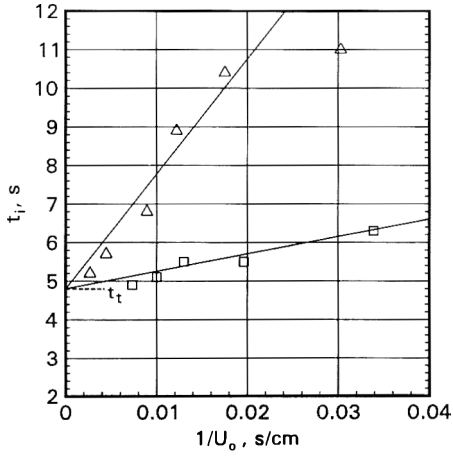

Fig. 9. Intercept time for neutral releases in: (△) large, and (□) small valleys.

qualitatively consistent with the larger z_0/H for this case, although the difference seems rather greater than can be accounted for by the relatively stronger turbulence effects. Again, geometrical differences are probably not insignificant.

4.3 Heavy gas releases

Releases of carbon dioxide and propane mixtures were made in the large valley with various flow rates at four different tunnel speeds, corresponding to $U_0 = 0.33$, 0.58, 0.82 and 1.12 m/s. Values of the governing variables (U_0 and V_s) and corresponding non-dimensional parameters (Re_0, Ri_s, Ri_0 and V_0) are given in Table 2, along with the principal results for both the steady-state averaged concentration at the sampling locations (C_0 and hence Ri_0) and the intercept time, t_i (and hence t_i'). The latter was deduced from the transient experiments by drawing a straight line through the $C' \ll 1$ region of the semi-log plots of $C'(t)$ vs. t, with a slope corresponding to the averaged decay time from Fig. 8b (14.5, as discussed in the previous section). A typical set of the transient results for fixed U_0 (0.58 m/s) is shown in Fig. 10. It is clear that as the flow rate increases, so that steady-state concentrations become larger, the initial decay is delayed, as expected. Eventually, however, the decay rate becomes identical with that of a neutral release at the same U_0, as expected.

It should be emphasised that the time dependence of the concentration was found not to be a strong function of the sampling location. This is demonstrated in Fig. 11, which shows a set of results for a particular, but typical, case ($U_0 = 0.58$ m/s, $Ri_s = 3.85$, $V_0 = 0.000565$). The sampling location corresponding to each curve is shown on the inset diagram and it is evident that only for the locations closer than about 0.2 H to the source does the measured concentration start to decay noticeably earlier than elsewhere. All sampling locations were within, or very close to, the mean separation region, except for one port just beyond the downstream edge of the valley. At this location the decay is delayed rather longer, as would be expected.

In accordance with eq. (10), the steady-state values of C_0 are plotted in Fig. 12 in the form $(C_0/(C_s \varepsilon V_0) - 1)$ vs. Ri_0, with the ε value implied from the earlier neutral release experiments (16.7 for the large valley, see previous section). It can be seen that data obtained at the lowest U_0 generally lie a little below the rest of the data, which is, again, almost certainly a Reynolds number effect. If the ε value for those particular points is adjusted to the value (11.8) implied by the $U_0 = 0.33$ m/s data point on Fig. 6, agreement is noticeably improved. The corrected points are included in Fig. 12 and most data cluster quite well around a straight line whose slope (n, in eq. 10) is about 0.5. (The exceptions are largely for cases in which the propane flow rates are at their lowest so that possible measurement inaccuracies are greatest.) These results would seem to provide reasonable confirmation of the assumed form of the entrainment relation (eq. 7).

Equation (11) implies that the intercept time, t_i', defined earlier, should satisfy the relation:

$$t_i'/\tau = (\alpha/n) Ri_0^n. \tag{15}$$

In Fig. 13 t_i'/τ is plotted against Ri_0 and a line of slope $n = 0.5$ (deduced earlier from the steady-state data, Fig. 12) is included in the figure. The sampling tube travel time (4.8 s), deduced from the neutral data (Fig. 9), has been subtracted

TABLE 2

Principal variables for heavy gas experiments

U_0 (m/s)	Re_0 (U_0H/ν)	Ri_s $[gH\Delta\rho_s/(\rho_a U_0^2)]$	V_s (cm^2/s)	C_0/C_s (%)	Ri_0 $(Ri_s \cdot C_0/C_s)$	$V_0 \times 10^4$ (V_s/U_0H)	$(t_i - t_t)$ (s)	t_i' $[U_0(t_i - t_t)/H]$
0.33	5588	11.9	0.152	0.330	0.0390	1.813	14.5	18.84
0.33	5588	11.9	0.425	1.870	0.2230	5.070	51.1	66.39
0.33	5588	11.9	0.667	3.510	0.4180	7.957	93.1	121.0
0.33	5588	11.9	0.917	5.410	0.6440	10.94	120.1	156.0
0.33	5588	11.9	1.167	6.900	0.8210	13.92	150.2	195.1
0.58	9821	3.85	0.125	0.198	0.0076	0.848	9.10	20.78
0.58	9821	3.85	0.833	2.200	0.0847	5.654	26.9	61.43
0.58	9821	3.85	1.500	4.270	0.1640	10.18	45.1	103.0
0.58	9821	3.85	2.125	6.760	0.2600	14.42	61.1	139.5
0.82	13885	1.93	0.083	0.092	0.00177	0.399	3.70	11.94
0.82	13885	1.93	0.250	0.252	0.00486	1.200	6.00	19.37
0.82	13885	1.93	0.833	1.070	0.0207	3.999	9.00	29.06
0.82	13885	1.93	1.667	2.290	0.0442	8.004	14.0	45.20
0.82	13885	1.93	2.500	3.120	0.0602	12.00	20.3	65.54
0.82	13885	1.93	3.500	6.500	0.1250	16.80	27.7	89.43
0.82	13885	1.93	4.500	8.110	0.1570	21.61	30.7	99.11
1.12	18965	1.033	2.208	3.120	0.0400	7.762	6.10	26.90
1.12	18965	1.033	4.458	5.870	0.0620	15.67	9.70	42.77

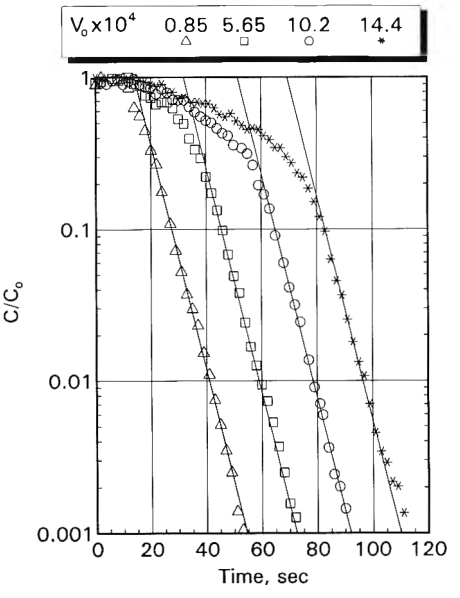

Fig. 10. Concentration decay for heavy gas releases. U_0 fixed at 0.58 m/s. Solid lines have slope measured for neutral release at same U_0.

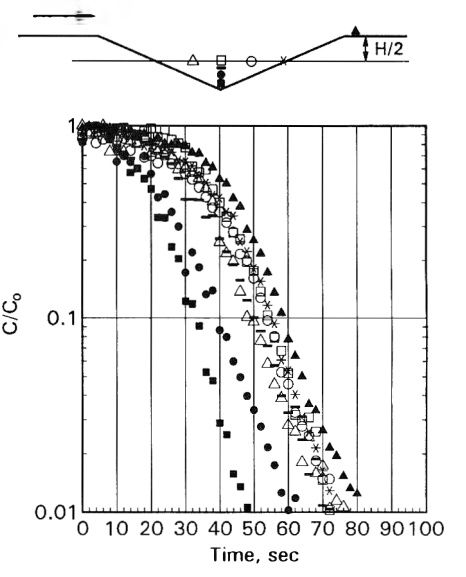

Fig. 11. Concentration decay for heavy-gas releases at different points in the valley. ($U_0 = 58$ cm/s, and $V_S = 0.83$ cm^3/s.)

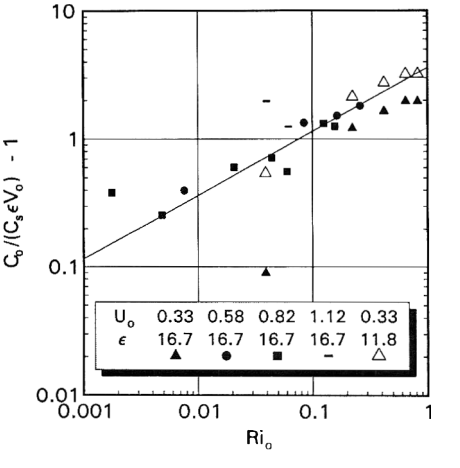

Fig. 12. Data fit to eq. (10). Line has slope of 1/2.

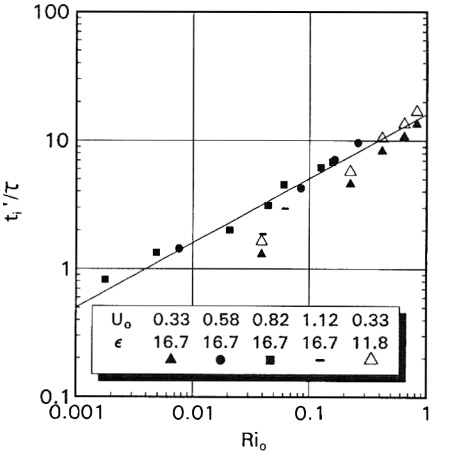

Fig. 13. Normalised intercept time as a function of Ri_0 (eq. 15). Line has slope of 1/2.

from the measured t_i. Again the data seem to be reasonably consistent with the expected form. Note that in this plot the average τ value (14.5) has been used as before, but data using $\tau = 11.6$ ($\varepsilon = 11.8$) for the lowest Reynolds number set is included; this improves the collapse somewhat. However, if an effective 'advection' time, accounting for the delay between $t = 4.8$ s (the tube travel time) and when the concentration at the sampling position begins to fall, is subtracted from the measured t_i data the results for the lowest U_0 case in Fig. 13 would again fall somewhat below the values shown. In fact, one might expect such an advection delay to increase somewhat for the larger values of Ri_s. We have made no attempt to account for this in comparisons with our theory since it would be inconsistent to do so without at the same time allowing some of the 'constants' used in the theory also to be functions of Ri.

5. Final discussion and application

We restate the major conclusions reached on the basis of the simple theoretical ideas discussed in Section 2. These are that the steady-state concentration in the valley satisfies

$$C_0/C_s = \varepsilon V_0(1 + \alpha Ri_0^n), \tag{10}$$

where $Ri_0 = C_0/C_s\, Ri_s$, $V_0 = V_s/U_0 H$ and α and ε are constants. If the source is removed, the concentration within the valley (inside the separated region) decays like

$$-\ln(C') + \alpha Ri_0^n (1 - C'^n)/n = t'/\tau, \tag{11}$$

where $C' = C(t)/C_s$ and τ is a decay time-constant. Our experimental data (for neutral releases and for heavy-gas releases after the initial effects of Ri have decayed) suggest that τ is about 15. Fackrell [8] found that for a rectangular building of breadth b and height h the decay time for dispersion of a release within the separated wake varied like

$$\tau = 11(b/h)^{1.5}/[1 + 0.6(b/h)^{1.5}]. \tag{16}$$

For the large valley, using L/H as the equivalent to b/h, this expression yields $\tau = 17$, which is not much greater than our measured values. Making some allowance for the fact that the separation region behind the building (with that b/h) is somewhat larger than the valley volume, there is encouraging agreement between these results. It seems that the relationship between 'residence time' and the separated region volume is close to that found by Fackrell (and by Hunt and Castro [3]) and is, therefore, dominated by turbulent dispersion rather than any mean flow features, as concluded in those earlier works. There is little reason to suppose that this result could not be extended to long valleys of other shapes, provided sensible estimates of the size of the recirculation region could be made.

Our data also follow the forms of eqs. (10) and (11) quite well, with $n = 0.5$ and $\varepsilon = 16.7$ (except at the lowest Reynolds number, where $\varepsilon = 11.8$ provides a better fit). In view of the various assumptions made this might seem rather surprising. Note, however, that the value of α differs by a factor of about two, depending on whether Fig. 12 (for the steady state result, eq. 10) or Fig. 13 (for the transient result, eq. 15) is used to deduce it. In the former case $\alpha = 3.7$ and in the latter, $\alpha = 7.9$. In this respect our data are *not* wholly consistent with the theory. It should be noted, however, that the α value from data fitted to eq. (10) will depend, to some extent, on the particular sample location used to obtain C_0. Although we chose a location within the recirculating, well-mixed region, use of a spatially averaged C_0 (over the whole of the separated flow) might yield closer agreement with the α obtained from eq. (15). Nonetheless, there are a number of assumptions inherent in the theory. The most dubious is probably that δ, the thickness of the mixing region, is not a function of Ri (and hence also not a function of time). We assumed $\alpha = k_5(\delta/H)^n = \text{constant}$. Figure 14 shows concentration contours in three cases — one for a neutral release (Fig. 14a), one for a typical dense gas release (Fig. 14b) and one for a dense gas release in which pooling is near occurring (Fig. 14c). It is clear that the nature of the flow is changed substantially in the pooling case, for which the mixing

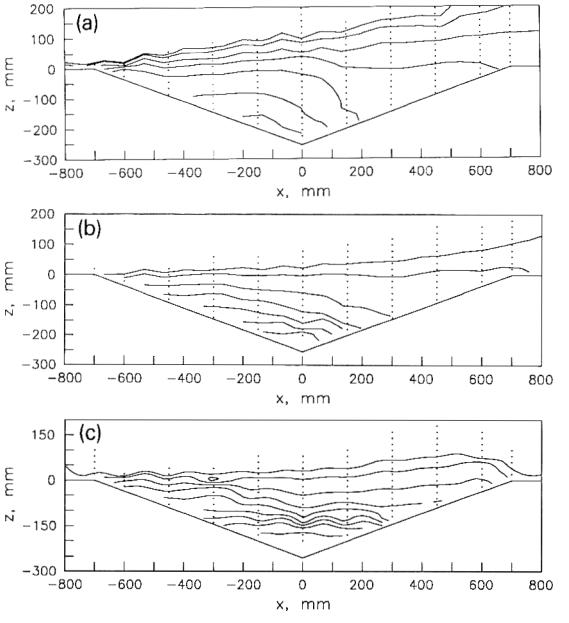

Fig. 14. Steady-state concentration contours (C/C_s in %) in large valley. Dots show locations of measurement points. (a) Neutrally bouyant release, $Ri_s = 0$, $V_0 = 0.345 \times 10^{-4}$, (b) Moderately heavy gas release, $Ri_s = 3.85$, $V_0 = 5.6 \times 10^{-4}$, and (c) Heavy gas release — near pooling conditions, $Ri_s = 3.85$, $V_0 = 14.3 \times 10^{-4}$.

region is essentially horizontal and the range of concentrations across the depth of the valley varies much more than it does for the neutral release. However, there are much weaker changes for the non-pooling heavy gas release; the contours in Fig. 14b have a very similar shape to those in the neutral case (Fig. 14a). Nonetheless one anticipates that α cannot be strictly constant over the entire range of (non-pooling) dense gas conditions.

It is difficult to construct a 'higher-order' theory in which α is allowed to vary with Ri_0; to begin with it is not clear what form such a dependence should take, but even if one were inserted the algebra rapidly becomes unwieldy. We believe, rather, that the sensible approach is to accept these limitations and use eqs. (10) and (11) as the basis of estimates of decay times for heavy gas releases, but employ the two different values of α as appropriate — i.e. 3.7 with eq. (10) to deduce Ri_0 and 7.9 with eq. (11) to deduce decay times. This procedure is relatively straightforward because $n=0.5$, which means that eq. (10) becomes a quadratic in $(C_0/C_s)^{0.5}$. A typical application will suffice as an example.

Assume that 60 tonnes of chlorine are released within an hour (i.e. around 1000 kg/min) over a 400 m span at the bottom of a valley of depth 50 m and width 250 m (similar proportions to the valleys in our experiments). Our pooling condition (eq. 14) then implies that provided the wind speed above the valley exceeds about 3.6 m/s pooling will not occur. If the wind is lighter than this, the BTS work should be used to estimate flushing times. Let us assume that there is a 4 m/s wind. V_0 and Ri_s have values of 7×10^{-5} and 44.4, respectively, and eq. (10) can then be solved, using $\varepsilon=16.7$ and $\alpha=3.7$, to give $C_0/C_s=0.00265$ and $Ri_0=0.118$. Use of eq. (11), with $\tau=15$ (to be conservative) and $\alpha=7.9$, then yields a time of about 27 min for the concentrations within the valley to decay to 100 ppm. This is still a highly dangerous concentration level[1]. Note that each additional decade of decay requires about a further 7 minutes — $(H\tau \ln(10)/U_0)$ — the neutral result. Release of a neutral gas under similar conditions (the same V_s) would lead to about a 10-minute decay to the 100 ppm level, so the heaviness of the chlorine has more than doubled the time required to flush the valley to 100 ppm. The original specification of a one-hour spill was chosen to ensure that effectively steady-state conditions occur before the release is stopped. Shorter releases at the same flow rate would lead to shorter decay times, of course.

6. Acknowledgements

We are grateful to the staff of the Fluid Modeling Facility, US Environmental Protection Agency, for making this research possible. IPC acknowledges the support of EPA Cooperative Agreements CR-814346 & CR-817931,

[1] A referee has pointed out that, of course, the dose (concentration integrated over exposure time) would in this case have been fatal long before the 100 ppm level was reached.

while a Visiting Professor at NC State University, AK is grateful for the advice and encouragement of Dr Gary Briggs and for the support of EPA Cooperative agreement CR-81434€ while a graduate student, and SPSA acknowledges support from both these EPA Agreements. This paper has been subjected to EPA review and approved for publication. Mention of trade names or commercial products does not constitute endorsement or recommendation for use.

Notation

A	area across which fluid is entrained out of the valley (L^2)
C_0	average volumetric concentration of gas in valley
C_s	source-gas concentration
C	spatially-averaged, time dependent gas concentration in valley
C'	C/C_0, dimensionless concentration
F	flux of concentration out of valley (L^3/T)
H	depth of valley (L)
$k_1 - k_5$	non-dimensional constants
L	spanwise length of valley (L)
n	dimensionless exponent (eq. 7)
Re_0	$U_0 H/\nu$, Reynolds number
Re_f	$(H/W)V_0 Re_0/Ri_s$, modified shear Reynolds number (eq. 12)
Ri	$g(\Delta\rho/\rho_a)\delta/U_0^2$, Richardson number
Ri_0	$Ri_s C_0/C_s$, steady-state valley Richardson number
Ri_s	$\gamma C_s g H/U_0^2$, source Richardson number
t	time (T)
t'	tU_0/H, dimensionless time
t_d	time for one-decade decay in concentration (T)
t_i	intercept time, i.e. time at $C'=1$ on linear extrapolation of exponential decay region (see Fig. 7) (T)
t_t	travel time of sample within tube leading to analyzer (T)
$U(z)$	ambient approach velocity (L/T)
U_e	entrainment velocity (L/T)
U_0	approach flow velocity at $z=H/4$ (L/T)
V	volume of valley (L^3)
V_s	volumetric flow rate of source gas, per unit cross-stream length (L^2/T)
V_0	V_s/HU_0, dimensionless source flow rate
V'	$V_0 Ri_S$
W	width of valley in flow direction (L)
W'	surface area (per unit width) of top of diffusing layer above heavy-gas pool (L)
x,y,z	Cartesian coordinates (axial, spanwise and vertical directions, respectively)
z_0	roughness length (L)

Greek

α	$k_5(\delta/H)^n$, dimensionless constant, (eq. 10)
γ	$(\Delta\rho_s/\rho_a)C_s$, factor relating concentration to density difference
δ	average entrainment layer thickness (L)
ε	$1/(k_1k_2k_3)$, dimensionless coefficient (eq. 10)
κ	molecular diffusivity (L^2/T)
ν	kinematic viscosity (L^2/T)
ρ_a	ambient air density (M/L^3)
ρ_s	source gas density (M/L^3)
$\Delta\rho_s$	density difference between source gas and ambient air (M/L^3)
θ	angle of valley side-wall slope
τ	$k_4/(k_1k_3)$ (eq. 11) $= U_0t_d/[H\ln(10)]$ (Fig. 8b), dimensionless decay time constant

References

1 G.A. Briggs, R.S. Thompson and W.H. Snyder, Dense gas removal from a valley by crosswinds, J. Hazardous Mater., 24 (1990) 1–38.
2 G.C. Christodoulou, Interfacial mixing in stratified flows, J. Hydraulic Res., 24 (1986) 77–92.
3 A. Hunt and I.P. Castro, Scalar dispersion in model building wakes, J. Wind Eng. Ind. Aerodyn., 17 (1984) 89–115.
4 J.A. Peterka and J.E. Cermak, Turbulence in building wakes, 4th Int. Conf. on Wind Effects on Buildings and Structures, London, Sept. 8–12th, 1975.
5 I.P. Castro and W.H. Snyder, A wind tunnel study of dispersion from sources downwind of three-dimensional hills, Atmos. Environ., 16 (1982) 1869–1887.
6 W. Humphries and J.H. Vincent, Experiments to investigate the transport processes in the near wake of discs in turbulent airflow, J. Fluid Mech., 75 (1976) 737–749.
7 J.H. Vincent, Scalar transport in the near aerodynamic wakes of surface-mounted cubes, Atmos. Environ., 12 (1978) 1319–1322.
8 J.E. Fackrell, Parameters characterising dispersion in the near wake of buildings, J. Wind Eng. Ind. Aerodyn., 16 (1984) 97–118.
9 W.H. Snyder, The EPA Meteorological Wind Tunnel: Its design, construction and operating characteristics, Report No. EPA-600/4-79-051. U.S. Environmental Protection Agency, Research Triangle Park, NC, 1979, 78 pp.

Journal of Hazardous Materials, 34 (1993) 295–311
Elsevier Science Publishers B.V., Amsterdam

Benzene vapor transport in unsaturated soil: Adequacy of the diffusion equation

Evangelos A. Voudrias and Chiayang Li*

School of Civil Engineering, Georgia Institute of Technology, Atlanta, GA 30332 (USA)

(Received October 7, 1992; accepted in revised form February 15, 1993)

Abstract

Experimental data for unsteady state benzene vapor transport in large (10.5 cm × 100 cm) columns packed with dry and wet soil were used to evaluate the adequacy of the diffusion equation. It was shown that the diffusion equation and local equilibrium, accounting for water phase partitioning and linear sorption, adequately described vapor transport in dry soil. In wet soil, however, possible benzene biodegradation resulted in deviation of the diffusion equation from the experimental data. At steady-state, the dimensionless vapor concentration versus distance profile for the dry soil was linear, as opposed to the same profile in the wet soil column The best fit retardation factor of benzene vapor for wet soil ($R = 12$) was lower than that for dry soil ($R = 46$), because of a reduction in vapor sorption capacity, due to competition with water molecules. A vapor phase sorption coefficient, $K'_d = 5.05\ cm^3/g$, was computed for the dry soil and $K'_d = 0$ for the wet soil.

Introduction

Volatile Organic Chemicals (VOCs) can be introduced in the subsurface environment as Non-Aqueous Phase Liquids (NAPLs) in a variety of ways. These include Leaking Underground Storage Tanks (LUSTs) and pipelines, accidental spills, land disposal sites, and industrial waste impoundments. Volatilization of NAPLs may result in significant mass transport of organic vapors away from the NAPL source. Since vapor migration is important with respect to very practical problems, such as site remediation by soil venting, leak detection from LUSTs, and contamination of clean groundwater, it is essential to understand the processes affecting vapor transport.

In most modeling studies, the simulation of vapor diffusive fluxes was quantified by Fick's laws of diffusion [1–5]. With a few exceptions [6], most models assumed local equilibrium for mathematical simplicity. Thus, mass transfer

*To whom correspondence should be addressed at: Holton and Dycus, Inc., 9724 Kingston Pike, Suite 800, Knoxville, TN 37922, Phone: 615-539-1863, Fax: 615-539-1865.

processes between different phases were described by partition coefficients, such as Henry's constant and linear solid–liquid and solid–gas sorption coefficients [3, 4]. Most of the models developed for vapor phase diffusion lack laboratory or field studies to verify their validity. Some experimental studies exist, which were conducted in 3 cm × 2 cm × 10 cm volatilization cells [7, 8], or 1.5 cm × 7.5 cm volatilization columns [9].

The objectives of this work were to assess the adequacy of the diffusion equation in describing non-steady-state experimental diffusion data for benzene vapor in unsaturated soil. The diffusion equation accounting for water phase partitioning and linear sorption isotherm was fitted to experimental concentration profiles of benzene vapor for dry and wet soil. Best fit retardation factors were used to determine linear vapor phase sorption coefficients, which were then used to assess the effect of moisture on gas phase sorption.

Benzene was used because of its significant water solubility (1780 mg/L), volatility (vapor pressure of 10.1 kPa), high toxicity, and abundance in subsurface contaminated sites, as a common component of gasoline and other petroleum products. Diffusion experiments were conducted using large columns (10.5 cm × 100 cm) packed with dry and wet soil. Experimental concentration profiles were established by analyzing vapor samples at different times and distances from the vapor source. There are several advantages in using large size diffusion columns. For example, a larger and more representative soil sample can be used. It is easier and more accurate tc observe vapor concentration profiles along the column length in larger than in smaller columns. Compared to small breakthrough columns with advective transport, the large diffusion columns provide longer residence times and are less likely to be subject to mass transfer limitations or practical flow problems in high clay, low permeability soils. To our knowledge, non-steady-state experimental diffusion data in large scale columns packed with soil other than sand have not been published in the peer-reviewed literature.

Materials and methods

Soil characterization

Soil used in this research was from a wooded depression, south of Waycross, Georgia. The soil was collected from a depth of 20–50 cm and was stored in black plastic bags at 7 °C. Representative aliquots were employed for determination of soil composition, particle-size distribution, moisture content, particle density, surface area, and organic carbon content. From the above results water-filled porosity, air-filled porosity, and total porosity were calculated.

The soil was taken out of the 7 °C room and spread on large plastic sheets to remove part of the moisture under room temperature. Then, it was passed through a 0.85 mm sieve (ASTM Sieve Number 20) to remove large debris. For wet soil column experiments, the soil was completely mixed and partially

air-dried at room temperature, whereas for dry soil column experiments the soil was completely mixed and oven-dried for 12 hours at 80 °C.

Particle size distribution was obtained by passing the soil through a series of sieves [10]. Moisture content was determined according to Gardner [11], by heating a soil sample of known size at 103 °C until constant weight. The particle density of each soil used was determined according to Blake and Hartge [12], by measuring the mass and the volume of the soil sample. The surface area was determined by using a single point BET method using N_2 and was an external surface area instead of total surface area [13].

Organic carbon of the soil was determined from the difference of total carbon and inorganic carbon content using the Total Carbon Apparatus (Model 5020, Coulometrics, Inc., Golden, CO). The carbon dioxide produced from combustion of a soil sample in an oxygen atmosphere was determined using a microcoulometer and was converted in percentage total carbon. Inorganic carbon was determined by acidification of the sample in a heated vessel, purging, trapping, and measuring carbon dioxide of inorganic origin.

After soil columns were packed, bulk density and porosities were determined using the following equations:

$$\rho_b = W/V \tag{1}$$

$$\varepsilon_T = 1 - \rho_b/\rho_p \tag{2}$$

$$\varepsilon_w = M\rho_b/\rho_w \tag{3}$$

$$\varepsilon_a = \varepsilon_T - \varepsilon_w \tag{4}$$

where ρ_b is the bulk density on dry weight basis (g/cm^3), W is the mass of oven-dried soil packed in column (g), V is the total volume occupied by soil (cm^3), ε_T is the total porosity, ρ_p is the particle density (g/cm^3), ε_w is the water-filled porosity, M is the moisture content (mass of water/mass of oven-dried soil), ρ_w is the water density (g/cm^3), and ε_a is the air-filled porosity.

Column experiments

Glass columns 10.5 cm i.d. and 100 cm long were used for the soil column experiments. Each column was equipped with six sampling ports located along the column axis at distances 0, 8.6, 18.4, 38.6, 58.4, and 78.3 cm, respectively, from the inlet end, as shown in Fig. 1. Each sampling port included a cylindrical glass septum holder, 5 mm i.d. and 10 mm high. A teflon-lined septum (HGC-138, Analabs, Inc., New Haven, CT) was placed into each septum holder. Then, a perforated 10 cm long 18 gauge stainless steel needle was inserted through the septum of each sampling port. A cleaning wire was kept inside the needle to prevent entrance of soil during the insertion step. The Luer hub of each needle was plugged with a two-way Mininert Teflon Valve (Alltech Associates, Inc., Deerfield, IL) which, when open, allowed the insertion of a gas-tight syringe for vapor sampling. Two layers of a 80 mesh stainless steel screen supported on a 1.2 cm thick and 1 cm wide circular aluminum ring were

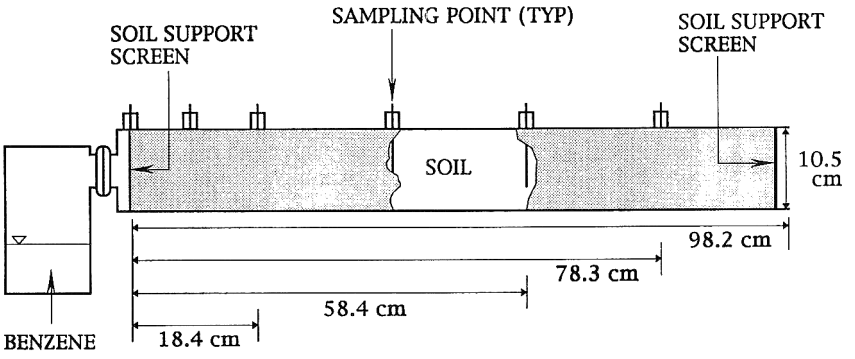

Fig. 1. Experimental column setup for benzene vapor transport experiments.

used on each end of the glass column to support the soil. The inlets of all soil columns were connected to a reservoir containing approximately 200 mL of benzene. Prior to starting each vapor experiment, the benzene reservoir was connected to a different but similar soil column to allow the establishment of steady-state vapor concentration, i.e., constant source strength at sampling port #1. Then, the reservoir was connected to the actual soil column and measurement of time was started. All experiments were conducted in a 20 °C constant temperature room. The column outlet was open and the soil was exposed in the atmosphere of the constant temperature room.

Each column was packed by adding soil in portions of 100 cm^3 at the surface of previously added soil, using a scoop attached to the end of a 100 cm aluminum rod. After each soil addition, the column was compacted by hand in a uniform fashion using a 3 cm diameter and 120 cm long wooden rod. This procedure minimized the stratification of soil in the column. The experimental conditions and particle size distribution of the soil used in both columns are summarized in Tables 1 and 2. A water-filled micromanometer was used in an attempt to measure pressure gradients within the soil column. Such gradients could result from sample withdrawing or barometric pressure fluctuations at the open end of the column. No measurable pressure gradients were observed, however.

Vapor sample analysis

Benzene vapor samples, 0.1 mL in volume were taken with a gastight syringe (Hamilton, Reno, NV) and periodically analyzed by gas chromatography (GC). Such sample size would prevent overloading of the GC detector and account for total gas volume withdrawn by all samples during the course of the experiment, of less then 1% of the total void space of each soil column.

All benzene vapor samples taken from column experiments were analyzed by GC (Model 5710A, Hewlett Packard) equipped with flame ionization detector and an integrator (Model 3380A, Hewlett Packard). A DB-1 capillary column 30 m long and 0.55 mm in diameter (J and W Scientific, Inc., Folsom, CA) was

TABLE 1

Experimental conditions for the soil columns

Condition	Benzene	
	Dry soil	Wet soil
Volume of NAPL, mL	200	200
Temperature, °C	20	20
Column diameter, cm	10.5	10.4
Column length, cm	97.1	97.1
Mass of soil[a], g	12,649	12,629
Moisture content[b], %	0.067 (0.005)[c]	8.86 (0.03)
Organic carbon[b], %	1.54 (0.022)	1.54 (0.022)
Bulk density[b], g/cm^3	1.50	1.40
Particle density[b], g/cm^3	2.51 (0.003)	2.44 (0.04)
Total porosity	0.400	0.428
Air-filled porosity	0.399	0.304
Water-filled porosity	0.001	0.124
External surface area[b], m^2/g	1.45	1.45

[a] Wet mass basis,
[b] Dry mass basis,
[c] Numbers in parentheses represent standard deviation.

TABLE 2

Particle size distribution of soil used in column experiments

Particle size (mm)	% Mass	
	Dry soil	Wet soil
>0.85	1.1	1.1
0.85–0.425	20.0	19.0
0.425–0.25	22.2	20.9
0.25–0.15	19.4	19.1
0.15–0.106	17.6	18.3
0.106–0.075	12.4	13.1
<0.075	7.3	8.5

used. The GC was operated under an isothermal temperature of 100 °C. Injection port and detector temperatures were 150 and 200 °C, respectively. In all experiments, vapor samples were injected with a 250-μL gastight syringe (Hamilton, Reno, NV) equipped with a two-way valve and side-port needle

(Hamilton, Reno, NV). Instrument response versus concentration curves were generated each day vapor samples were to be analyzed.

Transport model for the unsaturated soil columns

Diffusion equation

The one-dimensional conservation of mass equation with no chemical or biological reactions for benzene in isothermal, isotropic, and homogeneous unsaturated soil, without gas and liquid phase advection, takes the form of the well known diffusion eq. [3]:

$$\frac{\partial G}{\partial t} = D\frac{\partial^2 G}{\partial x^2} \tag{5}$$

where G is the benzene vapor concentration in air (g/cm^3), t is the time (s), x is the distance (cm), and D is the overall diffusion coefficient for benzene (cm^2/s).

Using the local equilibrium assumption to describe vapor distribution between the water, air, and soil phases, D can be calculated from the following equations [3]:

$$D = \frac{D_w/K_H + D_a}{\varepsilon_a R} \tag{6}$$

$$D_w = D_w^b \varepsilon_w \tau_w \tag{7}$$

$$D_a = D_a^b \varepsilon_a \tau_a \tag{8}$$

$$\tau_w = \frac{\varepsilon_w^{7/3}}{\varepsilon_T^2} \tag{9}$$

$$\tau_a = \frac{\varepsilon_a^{7/3}}{\varepsilon_T^2} \tag{10}$$

$$K_H = G/C \tag{11}$$

$$R = 1 + \left(\frac{1}{\varepsilon_a K_H}\right)(\varepsilon_w + K_{obs}\rho_b K_H) \tag{12}$$

where D_w, D_a are the effective diffusion coefficients of benzene in water and air, respectively, in the porous medium (cm^2/s); D_w^b, D_a^b are the molecular diffusion coefficients of benzene in bulk water and bulk air, respectively (cm^2/s); K_H is the air–water partition coefficient (Henry's constant); τ_w, τ_a are the water phase and air phase tortuosity, respectively; C is the benzene concentration dissolved in water (g/cm^3); K_{obs} is the overall linear sorption coefficient, accounting for both liquid and vapor phase sorption (cm^3/g); and R is the retardation factor.

In eq. (12), R can be interpreted as a retardation factor for the vapor plume taking into account both liquid and vapor phase sorption. The importance of

vapor phase sorption was discussed by Shoemaker et al. [4]. In order to include vapor phase sorption, we propose eq. (13), assuming a linear sorption isotherm:

$$S = K_{obs} G = K'_d G + \frac{K_d}{K_H} G \tag{13}$$

with

$$K_{obs} = K'_d + \frac{K_d}{K_H} \tag{14}$$

where S denotes the benzene concentration sorbed by soil (g/g), K'_d the linear sorption coefficient for vapor phase sorption, strong function of ε_w (cm^3/g), and K_d the linear soil–water partition or sorption coefficient (cm^3/g).

Depending on the soil moisture conditions, the values of K_d and K'_d may be determined as follows: At high moisture contents, ranging from soil surface coverage with more than five layers of water molecules to water retention capacity of the soil, $K'_d = 0$ and $K_{obs} = K_d/K_H$ [14, 15]. At intermediate moisture contents, corresponding to soil surface coverage with one to five layers of water molecules, K'_d decreases with increasing ε_w. K'_d corresponds to vapor sorption onto surface bound water, limited vapor dissolution into sorbed water [14, 15], and direct vapor sorption onto mineral surfaces, assuming the existence of such surfaces not covered by water molecules, due to soil heterogeneity. For this moisture region, we assumed that K_d is not a function of ε_w, although, in reality, K_d is expected to decrease, once ε_w drops below a critical value, ε_{wc} [16]. At extremely low ε_w, corresponding to soil surface coverage with less than one water layer, it is assumed that $K_d = 0$ and $K_{obs} = K'_d$, which is a strong function of ε_w.

The constants K_{obs}, K_d, and K'_d must be measured experimentally — K_d can also be computed from empirical correlations. Equation (15) (see Curtis et al. [17] and references therein) was used whenever an independent estimate for the liquid phase sorption coefficient was necessary:

$$K_d = K_{oc} f_{oc} \tag{15}$$

where K_{oc} is the organic carbon partition coefficient (cm^3/g), and f_{oc} the organic carbon fraction of soil.

Henry's constant, K_H, was calculated from eq. (11), using benzene solubility of 1780 mg/L [18] and saturated vapor concentration above liquid benzene of 325 mg/L calculated from ideal gas law and vapor pressure of 10.1 kPa [19]. The calculated value $K_H = 0.183$ is in close agreement with that measured by Mackay et al. [20], after temperature correction and unit conversion. The parameters of ε_T, ε_w, and ε_a were determined from eqs. (2), (3), and (4), respectively. Air and water phase tortuosities, τ_a and τ_w, were determined from eqs. (9) and (10), the Millington–Quirk model [21]. The value for D_a^b was taken as 9.32×10^{-2} cm^2/s [22]. This value is in close agreement with that determined by the Wilke–Lee equation [23], $D_a^b = 9.33 \times 10^{-2}$ cm^2/s.

TABLE 3

Input parameters to diffusion model for benzene

Parameter	Value	Equation or reference
G	325 mg/L	Weast [19]
C	1780 mg/L	Mackay and Shiu [18]
V_m	96 cm^3/mol	Lyman et al. [23]
ϕ_w	2.6	Lyman et al. [23]
K_H	0.183	Eq. (11)
τ_w	6.25×10^{-7} (dry soil)	Eq. (9)
τ_w	0.0419 (wet soil)	Eq. (9)
τ_a	0.733 (dry soil)	Eq. (10)
τ_a	0.340 (wet soil)	Eq. (10)
D_w^b	9.59×10^{-6} cm^2/s	Eq. (16)
D_a^b	9.32×10^{-2} cm^2/s	Lugg [22]
D_w	4.80×10^{-9} cm^2/s (dry soil)	Eq. (7)
D_w	5.93×10^{-7} cm^2/s (wet soil)	Eq. (7)
D_a	2.73×10^{-2} cm^2/s (dry soil)	Eq. (8)
D_a	9.63×10^{-3} cm^2/s (wet soil)	Eq. (8)

Bulk diffusivity in water was calculated from the Wilke–Chang equation [23] (Table 3):

$$D_w^b = \frac{7.4 \times 10^{-8} \ (\phi_w M_w)^{0.5} \ T}{\mu V_m^{0.6}} \tag{16}$$

where ϕ_w is the solution association constant (2.6 was used for aqueous solution), M_w is the molecular weight of water (g/mol), T is the temperature (K), μ is the solution viscosity (cP, or mPa s), and V_m is the benzene molal volume at normal boiling point (cm^3/mol).

Solution of the diffusion equation

The initial and boundary conditions for the column system (Fig. 1) are:

$$\text{I.C.} \quad G=0, \ t=0, \quad x>0 \tag{17}$$

$$\text{B.C.s} \quad G=G_0, \ t>0, \quad x=0 \tag{18}$$

$$G=0, \ t>0, \quad x=L \tag{19}$$

where G_0 is the saturated vapor concentration (g/cm^3), and L the soil column length (cm).

The solution to eq. (5) for the above initial and boundary conditions is given by eq. (20), which was derived from an equation given by Crank [24]:

$$\frac{G}{G_0}=1-\frac{x}{L}-\frac{2}{\pi}\sum_{n=1}^{\infty}\frac{1}{n}\sin\left(\frac{n\pi x}{L}\right)\exp\left(\frac{-Dn^2\pi^2 t}{L^2}\right) \tag{20}$$

To fit the diffusion model (eq. 20) to the experimental data, the fitting criterion FMIN for all distances was minimized. FMIN is related to the sum of squares of deviations of measured from predicted G/G_0 ratios according to the following equation [25]:

$$\text{FMIN}=\left\{\frac{1}{N}\sum_{i=1}^{N}\left[\left(\frac{G}{G_0}\right)_{mi}-\left(\frac{G}{G_0}\right)_{ci}\right]^2\right\}^{0.5} \tag{21}$$

where N denotes the number of data points for all distances, $(G/G_0)_{mi}$ is the experimentally measured concentration ratio, and $(G/G_0)_{ci}$ the model computed concentration ratio.

The best fit retardation factor corresponded to the minimum value of the fitting criterion FMIN.

Results and discussion

Adequacy of the diffusion equation and local equilibrium

It was assumed that benzene volatalized from the reservoir (Fig. 1) and moved inside the soil column only by diffusion. Experimental profiles of vapor concentration with respect to time or distance were analyzed using eq. (20). The initial condition (eq. 17) was satisfied, because benzene-free soil ($G=0$) was used. Similarly, eq. (18) was valid, because measured vapor concentrations, G_0, at sampling port #1 were constant within experimental error, after steady-state had been established, due to equilibrium with 200 mL of liquid benzene in the reservoir (Figs. 2 and 3). Equation (19) was valid, because of large volume dilution resulting from exposure of the column outlet in the atmosphere of a large (2.41 m × 1.62 m × 2.84 m) constant temperature room, which was continuously circulated by fans, providing a flow rate of 0.34 m^3/s. Taking into account the air exchange in the room due to the door opening for sampling, checking room temperature and column condition, it was calculated that the steady-state benzene concentration in the room was below 0.03 mg/L. This value is higher than the actual benzene concentration in the room, because it did not take into account the amount of benzene sorbed by the soil. In any case, it is well below the GC detection limit, which was 3.0 mg/L at a sampling volume of 100 μL.

Vapor samples were taken from sampling ports #1, #3, #4, #5, and #6 (Fig. 1) and analyzed by GC. The vapor concentration, G, divided by the average concentration for the same day in sampling port #1, G_0, was equal to the vapor concentration ratio, G/G_0. The ratios were plotted as a function of

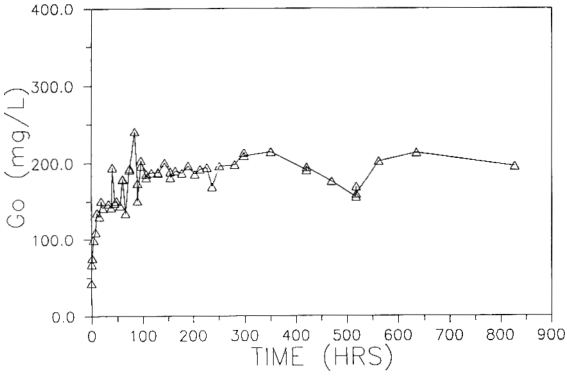

Fig. 2. Concentration of benzene vapor, G_0, at the inlet ($x=0$) of the dry soil column.

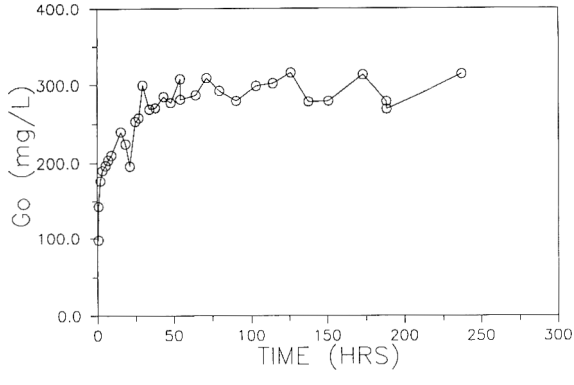

Fig. 3. Concentration of benzene vapor, G_0, at the inlet ($x=0$) of the wet soil column.

time for sampling ports #3, #4, #5, and #6 and are shown in Figs. 4 and 5, for dry and wet soil, respectively. The solid lines in the figures are the best fit curves of eq. 20, superimposed on the experimental data points. Tables 1 and 3 list all input parameters that were used for model simulations.

Minimization of FMIN (eq. 21) for every individual distance from the column inlet resulted in R values slightly different for each distance (Table 4). This difference could be due to experimental error, slight heterogeneities within the system, or combination of both. In order to determine a single R value for each column, FMIN was minimized for the pooled data from all distances and resulted in $R=46$ for the dry soil (Fig. 4, Table 4) and $R=12$ for the wet soil column (Fig. 5, Table 4). To assess the goodness of fit of Fick's law to the experimental data, the means of residuals $[(G/G_0)_{mi}-(G/G_0)_{ci}]$ and FMIN values for each distance were computed and are listed in Table 4. Mean

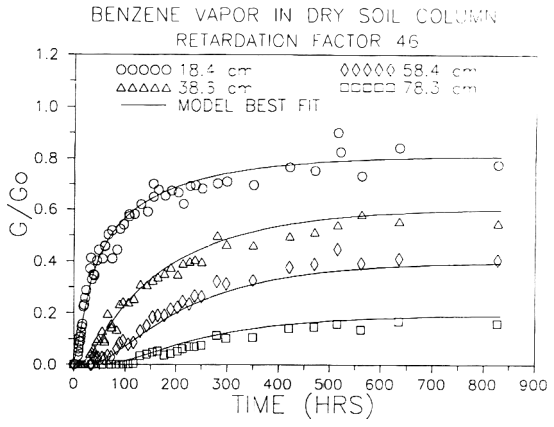

Fig. 4. Experimental and computed concentration profiles for benzene vapor in dry soil column.

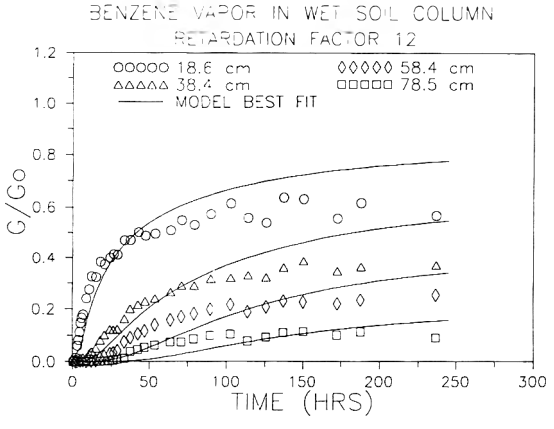

Fig. 5. Experimental and computed concentration profiles for benzene vapor in wet soil column.

residual values for both dry and wet soil columns were very close to zero, indicating that the model was not biased. FMIN values were smaller by more than a factor of 2 for the dry soil column, indicating a better model fit for the dry than the wet soil column. Visual inspection of Figs. 4 and 5 revealed a satisfactory fit for the dry soil and a rather poor one for the wet soil data.

The good agreement between eq. (20) and experimental data (Fig. 4) suggests that the diffusion equation was an adequate model in describing benzene vapor diffusion in dry soil. The local equilibrium assumption used to describe the vapor sorption by the soil was appropriate.

TABLE 4

Mean residual[a] and FMIN values for benzene vapor in dry and wet soil

Dry soil				Wet soil			
Distance (cm)	Best fit R	Mean residual	FMIN	Distance (cm)	Best fit R	Mean residual	FMIN
18.4	46	0.00101	0.03637	18.6	13	0.00186	0.08402
38.6	48	0.00102	0.02169	38.4	14	−0.00918	0.05476
58.4	39	−0.00217	0.01396	58.4	11	−0.00735	0.03864
78.3	55	0.02561	0.008151	78.5	10	−0.00483	0.02390
Overall	46	0.00449	0.02484	Overall	12	−0.00465	0.05649

[a] Residuals were computed from: $\text{Res} = [(G/G_0)_{mi} - (G/G_0)_{ci}]$.

The experimental data in Fig. 5 showed some early breakthrough, which may be indicative of a rate-limited mass exchange between the water and gas phases, followed by leveling off at lower than predicted concentrations, which may indicate biological degradation. Biological activity in the dry soil experiment was not significant, because the soil was treated by heating at 80 °C for 12 hours prior to exposure in benzene vapor. The wet soil columns, however, could support biological activity, under aerobic conditions, assuming that the organic soil could provide sufficient nutrients. Although it is very likely that biodegradation contributed to the poor model fit in Fig. 5, this does not constitute a proof, because the bacterial count of the soil and the oxygen consumption were not monitored throughout the experiment. The data analysis in Figs. 4 and 5 did not consider any density driven flow for benzene. This was based on identical concentration values from vapor samples obtained from the uppermost and lowermost points of the soil columns.

Figures 4 and 5 show that benzene concentrations reached steady- state after approximately 350 hours for the dry and 100 hours for the wet soil column. The average steady-state vapor concentration ratios $\pm$ one standard deviation for ports #1, #3, #4, #5, and #6 for the dry soil column were: 1.0 ± 0.1, 0.80 ± 0.07, 0.55 ± 0.06, 0.41 ± 0.03, and 0.15 ± 0.02, respectively. The respective concentration ratios for the wet soil column were: 1.0 ± 0.06, 0.59 ± 0.01, 0.35 ± 0.04, 0.22 ± 0.02, and 0.10 ± 0.008. As the distance from the source (port #1) increased, vapor concentration decreased. This can be explained on the basis of eq. (5), which at steady-state becomes:

$$\frac{d^2G}{dx^2} = 0 \tag{22}$$

Using the boundary conditions (eqs. 18, 19), the solution of eq. (22) is:

$$G = G_0\left(1 - \frac{x}{L}\right) \tag{23}$$

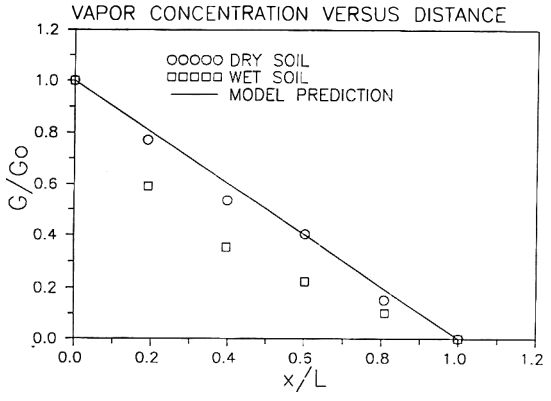

Fig. 6. Steady-state concentration profiles of benzene vapor versus distance for dry and wet soil columns.

Figure 6 shows that the concentration at steady-state decreased linearly with increasing distance in the dry soil column, in agreement with eq. (23). In the wet soil column, the concentration decrease with distance was not linear, probably because of benzene vapor biodegradation (Fig. 5). Field scale biodegradation of vapors in unsaturated soil was also reported by Ostendorf and Kampbell [26]. The concentration ratio, G/G_0, for the wet soil column did not increase much between 100 and 250 hours and averaged at approximately 0.6 at the distance of 18.6 cm. The theoretical concentration ratio at steady-state at the same distance, based on Fick's law, should be equal to 0.81, however.

The tortuosity values used in this study were determined according to eqs. (9) and (10) and were applied to all experimental data simulations. An error in the estimate of tortuosity would be reflected in the values of D_w and D_a (eqs. 7 and 8). A sensitivity analysis for τ_w in the 0.1–0.9 range showed no difference in the computed concentration profiles, indicating that eq. (20) is insensitive to τ_w. A sensitivity analysis for τ_a in the 0.1–0.9 range is presented in Fig. 7 for the dry soil column. Increase of τ_a by 25% ($\tau_a = 0.916$) resulted in small difference in the computed concentration versus time curve. In contrast, decrease of τ_a by 25% ($\tau_a = 0.550$) or 50% ($\tau_a = 0.367$) resulted in a much larger difference in the same curve, indicating that the diffusion model was more sensitive to $\tau_a < 0.733$ (computed from eq. 10). Sensitivity analysis for the wet soil column was not conducted because of the poor model fit.

The experimental data of the dry soil column at $x = 58.4$ cm, were compared with model predictions (eq. 20) for different R values, in Fig. 8. The results showed that the diffusion model was very sensitive with respect to R at low R values ($R < 30$) and less sensitive at higher R values ($R > 40$). Sensitivity analysis for the wet soil column was not conducted because of the poor model fit.

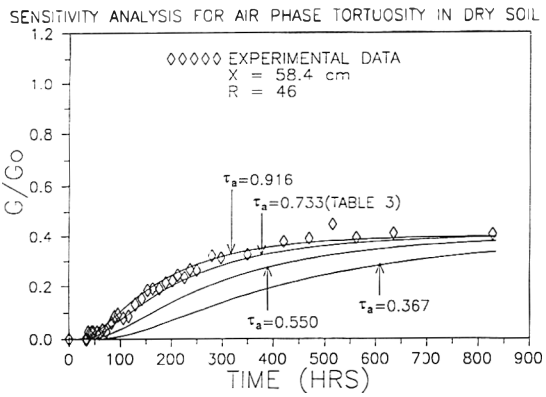

Fig. 7. Sensitivity analysis of benzene vapor in dry soil for different values of air-phase tortuosity.

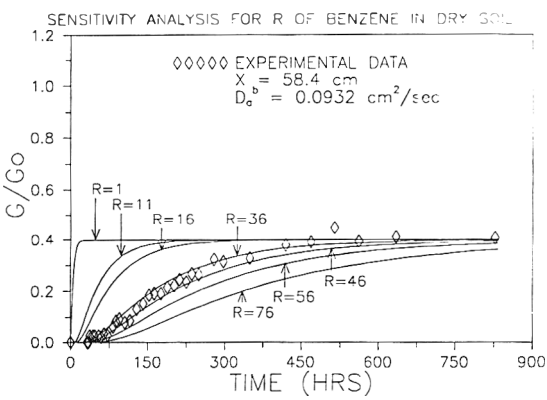

Fig. 8. Sensitivity analysis of benzene vapor in dry soil for different values of retardation factor.

Sorption coefficients

The best fit retardation factors of benzene vapor were 46 and 12 for dry and wet soil, respectively. This is consistent with results from previous studies, which showed a significant reduction in sorption capacity with increasing moisture because of competition by water molecules [27]. A lower sorption capacity for benzene would result in a smaller K_{obs} value for wet soil, or a smaller R, according to eq. (12).

The best fit retardation factors were used to calculate an overall sorption coefficient, K_{obs}, using eq. (12). K_{obs} values of benzene for dry and wet soil were 12 and 1.9 cm^3/g, respectively. For the dry soil area of 1.45 m^2/g, bulk density of 1.5 g/cm^3 (Table 1), and water surface area of 11.4 $Å^2$/molecule [28], a moisture content required for monolayer coverage of the soil of 0.00057 mL H_2O/cm^3 of

TABLE 5

Vapor phase sorption coefficients from column experiments

Soil	R	K_{obs} (cm^3/g)	K'_d [a] (cm^3/g)	K_d [a] (cm^3/g)
Dry	46	12	5.3	1.2[b]
Wet	12	1.9	0	0.35

[a] Computed from eq. (14).
[b] Computed from eq. (15).

soil was calculated. For $\theta_w = 0.001$, the overall coverage of dry soil was less than two layers of water molecules. To calculate the benzene gas phase sorption coefficient, K'_d, from K_{obs}, at this water coverage, eq. (14) was used, which assumes no effect of moisture content on K_d, even at very low moisture contents. Therefore, a saturated system $K_d = K_{oc} f_{oc} = 1.23\ cm^3/g$ was used, where $K_{oc} = 80\ cm^3/g$ [29] and $f_{oc} = 0.0154$ (Table 1). Thus, the gas phase sorption coefficient for the dry soil column was calculated as $5.3\ cm^3/g$ (Table 5). For the wet soil, $K'_d = 0$ [14, 15]. Therefore, $K_d = K_{obs}$ $K_H = 0.35\ cm^3/g$. This would correspond, however, to a $K_{oc} = 0.35/0.0154 \approx 23\ cm^3/g$, almost four times lower than the $K_{oc} = 80\ cm^3/g$ reported [29]. This difference, however, is within the expected accuracy of eq. (15).

Conclusions

The results of this study showed that the diffusion equation, accounting for water phase partitioning and linear sorption isotherm, adequately described the experimental concentration profiles of benzene vapor in a dry soil column. However, its applicability to benzene vapor in the wet soil column resulted in poor data fit, which was attributed to possible biodegradation [26]. Due to experimental difficulties, the assumption of isotherm linearity could not be independently confirmed. However, linear isotherms are expected in wet soil systems and, in general, at low vapor concentrations [27].

Best fit retardation factors for benzene vapor were 46 and 12 for the dry and wet soil column, respectively. The lower R value for the wet soil column is consistent with results from previous studies, which showed a significant reduction in sorption capacity with increasing moisture, because of competition by water molecules [27]. The higher sorption capacity for benzene vapor in dry soil resulted in a higher K_{obs} value or larger R, according to eq. (12). However, because of the poor fit of diffusion equation to experimental data, it was not possible to determine a reliable K_{obs} value for wet soil, and the retardation factor ($R = 12$) must be used with caution. Sensitivity analysis of the diffusion model was performed only on dry soil and showed that the model

was very sensitive with respect to R for low R values ($R < 30$), and less sensitive for high R values ($R > 40$). It was also very sensitive with respect to τ_a for $\tau_a < 0.733$ and less sensitive for $\tau_a > 0.733$.

Acknowledgments

We thank Mr. Allen Rigdon, scientist of the Soil Conservation Service, Waycross, Georgia, for assisting us in soil collection. We also thank Dr. A. Horowitz of U.S.G.S., Doraville, Georgia, for determining the soil surface area.

References

1 W.A. Jury, W.F. Spenser and W.F. Farmer, Behavior assessment model for trace organics in soil, I. Model description, J. Environ. Qual., 12(4) (1983) 558–564.
2 A.L. Baehr and M.Y. Corapcioglu, A compositional multiphase model for groundwater contamination by petroleum products, 2, Numerical solution, Water Resour. Res., 23(1) (1987) 201–213.
3 A.L. Baehr, Selective transport of hydrocarbons in the unsaturated zone due to aqueous and vapor phase partitioning, Water Resour. Res., 23(10) (1987) 1926–1938.
4 C.A. Shoemaker, T.B. Culver, L.W. Lion and M.G. Peterson, Analytical models of the impact of two-phase sorption on subsurface transport of volatile chemicals, Water Resour. Res., 26(4) (1990) 745–758.
5 T.B. Culver, C.A. Shoemaker and L.W. Lion, Impact of vapor sorption on the subsurface transport of volatile organic compounds: A numerical model and analysis, Water Resour. Res., 27(9) (1991) 2259–2270.
6 B.E. Sleep and J.F. Sykes, Modeling the transport of volatile organics in variably saturated media, Water Resour. Res., 25(1) (1989) 81–92.
7 A.A. Karimi, W.J. Farmer and M.M. Cliath, Vapor-phase diffusion of benzene in soil, J. Environ. Qual., 16(1) (1987) 38–43.
8 W.J. Farmer, M.S. Yang, J. Letey and W.F. Spencer, Hexachlorobenzene: Its vapor pressure and vapor phase diffusion in soil, Soil Sci. Soc. Am. J., 44 (1980) 676–680.
9 Ts. Galin, Z. Gerstl and B. Yaron, Soil pollution by petroleum products, III. Kerosene stability in soil columns as affected by volatilization, J. Contam. Hydrol., 5 (1990) 375–385.
10 ASTM, Standard method for particle-size analysis of soils, In: Annual Book of ASTM Standards, Part 19, Natural Building Stones; Soil and Rock; Peats, Mosses, and Humus. American Society for Testing and Materials, Philadelphia, PA, 1979, pp. 112–122.
11 W.H. Gardner, Water content, In: A. Klute (Ed.), Methods of Soil Analysis, Part 1, Physical and Mineralogical Methods. American Society of Agronomy, 2nd edn., Madison, WI, 1986.
12 G.R. Blake and K.H. Hartge, Particle density, In: A. Klute (Ed.), Methods of Soil Analysis, Part 1, Physical and Mineralogical Methods. American Society of Agronomy, 2nd edn., Madison, WI, 1986.
13 A. Horowitz and K. Elrick, The relation of stream sediment surface area, grain size and composition to trace element chemistry, Appl. Geochem., 2 (1987) 437–451.
14 S.K. Ong and L.W. Lion, Effects of soil properties and moisture on the sorption of trichloroethylene vapor, Water Res., 25(1) (1991) 29–36.
15 S.K. Ong and L.W. Lion, Mechanisms for trichloroethylene vapor sorption onto soil minerals, J. Environ. Qual., 20 (1991) 180–188.

16 P.A. Ryan and Y. Cohen, Diffusion of sorbed solutes in gas and liquid phases of low-moisture soils, Soil Sci. Soc. Am. J., 54 (1990) 341–346.
17 G.P. Curtis, M. Reinhard and P.V. Roberts, Sorption of hydrophobic organic compounds by sediments, In: J.A. Davis and K.F. Hayes (Eds.), ACS Symp. Series 323, Geochemical Processes at Mineral Surfaces, 1986, pp. 191–216.
18 D. Mackay and W. Y. Shiu, A critical review of Henry's law constants for chemicals of environmental interest, J. Phys. Chem. Ref. Data, 10(4) (1981) 1175–1199.
19 R.C. Weast (Ed.) CRC Handbook of Chemistry and Physics, 66th edn. CRC Press, Boca Raton, FL, 1985.
20 D. Mackay, W.Y. Shiu and R.P. Sutherland, Determination of air–water Henry's law constants for hydrophobic pollutants, Environ. Sci. Technol., 13(3) (1979) 333–337.
21 R.J. Millington and J.P. Quirk, Permeability of porous solids, Trans. Faraday Soc., 57 (1961) 1200–1207.
22 G.A. Lugg, Diffusion coefficients of some organic and other vapors in air, Anal. Chem., 40(7) (1968) 1072–1077.
23 W.J. Lyman, W.F. Reehl and D.H. Rosenblatt, Handbook of Chemical Property Estimation Methods. McGraw-Hill, New York, 1982.
24 J. Crank, The Mathematics of Diffusion, 2nd edn. Clarendon Press, Oxford, 1975.
25 W.E. Thacker, V.L. Snoeyink and J.C. Crittenden, Modeling of activated carbon and coal gasification char adsorbents in single-solute and bisolute systems, Water Resources Research Report 161, University of Illinois, Urbana, IL, 1981.
26 D.W. Ostendorf and D.H. Kampbell, Biodegradation of hydrocarbon vapors in the unsaturated zone, Water Resour. Res., 27(4) (1991) 453–462.
27 C.T. Chiou and T.D. Shoup, Soil sorption of organic vapors and effects of humidity on sorptive mechanism and capacity, Environ. Sci. Technol., 19 (1985) 1196–1200.
28 M.S. Peterson, L.W. Lion and C.A. Shoemaker, Influence of vapor phase sorption and diffusion on the fate of trichloroethylene in an unsaturated aquifer system, Environ. Sci. Technol., 22 (1988) 571–578.
29 W.A. Jury, D. Russo, G. Streile and H. El Abd, Evaluation of volatilization by organic chemicals residing below the soil surface, Water Resour. Res., 26(1) (1990) 13–20.

Journal of Hazardous Materials, 34 (1993) 313–333
Elsevier Science Publishers B.V., Amsterdam

Stochastic modeling of flow and transport in deep-well injection disposal systems

Seung-Whee Rhee[a,*], Danny D. Reible[a] and W. David Constant[b]

[a]*Department of Chemical Engineering, Louisiana State University, Baton Rouge, LA 70803 (USA)*
[b]*Hazardous Waste Research Center, Louisiana State University, Baton Rouge, LA 70803 (USA)*

(Received July 15, 1992; accepted in revised form December 24, 1992)

Abstract

The migration of deep-well injected waste in heterogeneous confining layers is evaluated using numerical simulation. Of primary concern is the migration potential through permeable sand paths between less permeable shale. The configuration of the predominantly shale confining layers was defined by Monte Carlo techniques assuming a binary random structure composed of pure sand and pure shale. Three-dimensional flow simulations using MODFLOW, a finite difference model, indicated that essentially continuous sand paths and unacceptably rapid transport might exist through confining layers with an average shale fractions of less than about 0 65 and that two and three dimensional flow simulations were essentially equivalent for high (>0.6–0.7) or low (<0.4–0.5) shale fractions. Diffusion and advection–dispersion in the configurations with a shale fraction greater than 0.65 were estimated via a two-dimensional finite element model. Interaction between organic constituents of the waste and the soil media is represented by linear sorption. The model was applied to an example in which dilute aqueous solutions of acrylonitrile were deep-well injected. Advective penetration of a representative confining layer over 10,000 years was found to be small (<3 m assuming injection pressures were maintained throughout the period). Even including diffusion and dispersion, concentrations in excess of drinking water criteria did not extend beyond the confining layers after simulation for 10,000 years.

Introduction

Disposal of liquid hazardous waste by subsurface injection has come into favor as a means of waste disposal because of its relatively low cost. In 1981, about 60 percent of all hazardous wastes in the U.S. were disposed of by deep-well injection [1]. Most injected wastes are mineral acids or water contaminated by small amount of hazardous materials. The wastes are injected into relatively permeable formations confined by adjacent low permeability

*To whom correspondence should be addressed.

shales. As increasing volumes of hazardous materials have been injected into the subsurface, concern for contamination of underground sources of drinking water has grown. Much of the concern regarding deep-well injection arises from the lack of information available on the transport and ultimate fate of hazardous materials after injection

The Resource Conservation and Recovery Act of 1976 (RCRA, U.S. Public Law 94-580) suggested that all deep-well injection projects be banned by August 1988 unless they were shown to be protective of human health and the environment. The U.S. Environmental Protection Agency (EPA) proposed that hazardous waste disposal by deep-well injection be banned unless it can be shown that the injected waste will be rendered non-hazardous in the disposal zone or that the waste will remain confined for at least 10,000 years [2].

Modeling is required to predict underground waste movement and the ultimate fate of the waste over this time period. Due to uncertainties in the subsurface fate processes, most efforts in support of petitions for deep-well injection have focused on demonstrating negligible migration through the confining layers. In general, such petitions have assumed that the shale confining layers are essentially homogeneous, low permeability strata and that diffusion is the most important migration mechanism. In the present work, the effect of heterogeneities in the sand shale system will be considered. In particular, the effect of high permeability sand inclusions on the waste migration potential will be evaluated through numerical simulation of flow and transport in stochastically generated representations of the confining layer structure.

Fogg [3] discussed the topic of sand-body interconnectedness in the Wilcox aquifer system, Texas. He found that the channel-fill sand bodies appeared to be laterally interconnected where sand percent exceeded 20% and disconnected where sand percent was less than 20%. Even though there were virtually no data on the vertical interconnection of sand-body, anisotropy ratio of hydraulic conductivity was reasonably 10^{-4}. Hence, it could be expected that vertical interconnection in sand bodies be much more difficult than lateral interconnection.

Since most natural subsurface formations display a significant variation in permeability due to heterogeneity, considerable effort has been devoted to the problem of estimating the effective permeability when the local permeability is spatially variable. Two main stochastic approaches are available for estimating effective permeabilities in heterogeneous porous media: numerical methods based on Monte Carlo simulations [4–7] and analytical methods based on perturbation theory [8–10]. While the most desirable estimate of subsurface flow is obtained using an analytical solution, a spectral analysis method based on small perturbations in permeability is inappropriate for the assessment of problems in which the input variables have a large variance.

Several researchers [7, 9, 11] found that the most probable behavior of a heterogeneous system approaches that of a homogeneous system with an effective permeability expressed by the geometric mean of the individual permeabilities. Desbarats [12] numerically estimated effective permeabilities in a sand–shale

formation under steady state uniform flow conditions. His simulations were limited to a sand–shale permeability ratio of 10^4 to 1, although this ratio is of the order of 10^7 to 1 in the region of interest here. He found that the effective permeability was a function of the shale volume fraction, the spatial correlation structure, and the flow field dimensionality. For the case of binary permeability distribution and an isotropic formation, Desbarats' numerical results were found to agree fairly well with a self-consistent formula for effective permeability derived by Dagan [13]. Kramers et al. [14] used petrographic image analysis to characterize the structure of low shale fraction gas reservoir systems. They showed that the shale significantly reduces the permeability of these zones.

To estimate the effective horizontal and vertical permeability, Haldorsen and Lake [15] developed an analytical expression based on a stream tube concept for each grid block in the simplified flow field. The stream tube approach relates effective permeability to the tortuosity of flow paths through the medium. Begg et al. [16] revised this approach to get effective vertical permeability without generating a synthetic subsurface formation. Desbarats [12] suggested that the stream tube approach had reasonable results only at low shale fraction because the approach contained an implicit shale noninteraction assumption which was violated even at moderate shale fraction.

The estimation of flow or effective permeability in the above studies is limited to low shale fraction formations or low contrast between sand and shale permeability. These limitations are relaxed herein. In addition, since the primary quantity of interest is chemical transport of the injected wastes and not bulk flow, transport modeling is also addressed.

Dispersion in heterogeneous porous media occurs because of the spatial variability in the velocity field, which in turn, is primarily due to the variability in hydraulic conductivity. This spatial variability is explicitly modeled herein at a distance scale greater than or equal to the height of the shale zones. At smaller scales, Fickian dispersion is assumed. Scale dependent dispersion at smaller scales [11, 17] is not modeled but this effect has been suggested to be minimal at long times [18, 19]. Fickian models have also been used previously to model dispersion in heterogeneous media [10, 20–23]. Recently, for low shale fractions, it has been shown that macrodispersive transport in sand–shale sequences cannot be represented by Fickian models because of channeling [24].

The current approach uses a numerical simulation of the flow and transport in a Monte Carlo generated sand–shale formation. By generating large numbers of configurations, the statistics of the waste migration potential can be defined. The confinement zone was modeled as a combination of binary random structures composed of either pure sand or pure shale. The effective permeability of each hypothetical configuration was evaluated by solving the steady-state, incompressible ground-water flow equation via a finite element method. The expected value and 95% confidence limits for effective permeability in the actual subsurface configuration were assumed represented by the statistics of the ensemble of hypothetical configurations.

The penetration of wastes into the confining layer is obtained by solving the transient advection–dispersion equation for solute transport via a finite element method [14, 25]. In the solute transport equation, the velocity field from the flow modeling is used to solve the concentration profile. Because of the coupled nature of flow and transport equations, the transport simulations were limited to two-dimensional simulations in a particular subsurface configuration. The transport simulations were limited to high shale fractions, where the flow modeling suggested that the effective permeability was not sensitive to the particular subsurface configuration. From the concentrations predicted by the numerical simulations, concentration isopleths are generated within the hypothetical confining layers and mean concentration profiles are obtained as a function of shale fraction. Finally, the penetration distance of a weakly sorbing contaminant, acrylonitrile, was estimated.

Generation of subsurface formations

An empirical shale fraction profile as a function of depth in subsurface formations can be determined at a specified site from observed well log data using gamma ray and spontaneous potential–resistivity logs. The well log can also identify layers and layer thickness. The focus of this study is on the flow and transport through the shale confining layers that represent the primary resistance to migration of injected wastes. A confining layer is assumed to be composed of a random sequence of sand and shale in proportion to the average shale content of that layer as defined by well logs. Well log information is also used to estimate the thickness of a particular layer. Confining strata are assumed to exhibit no fractures and faults.

In order to generate the configuration of confining layers, statistics of shale thickness, shale width and shale fraction are needed. Since the lateral dimension of the shale regions remain unknown except for nearby wells, individual shale zone positions and their width are randomly selected from a distribution function under an assumption that each shale zone is independent of all other shale zones. For simplicity, the shale width distribution is assumed defined by a triangular distribution function which can be specified by a maximum, a minimum and a most probable value. Random placement of the shale zones within an initially sand-filled media is continued until the shale fraction in the layer reaches the level estimated by well log data. Overlapping shale zones are possible in the random placement algorithm and the shale fraction was corrected to avoid double-counting of this shale.

Haldorsen and Lake [15] suggested a similar approach that generated a configuration of 2D sand–shale formations with a specified fraction of shale using statistical techniques. In their work, the thickness and width of shale were sampled from an empirical cumulative distribution, while the position of shale was assigned randomly. It is necessary to employ a large number of elements to determine the configuration of the subsurface formation with their techniques.

In this study, we modify their technique to reduce the number of elements and to allow for lateral overlapping. The thickness of confining layers is inferred from the actual well log data while the thickness of shale is assumed to be uniform within a given confining layer. The position and width of shale are assigned randomly.

At low shale fractions, permeable sand veins are essentially continuous, allowing potentially rapid vertical transport. At high shale fractions, however, sand zones are isolated by shale regions so that transport paths through high permeability sand veins may not exist. As expected, the degree of lateral overlapping and the number of isolated sand zones increases as the shale fraction and the aspect ratio of the shale zones, defined by the ratio of width to thickness of shale zone, increase. The lateral dimensions (length and width) of sand or shale zones are typically much greater than their vertical dimension (thickness) [26]. The effective vertical permeability of a formation increases as the aspect ratio decreases [14, 27]. The effective horizontal permeability is almost independent of the aspect ratio [12, 27]. An aspect ratio of unity provides a reasonable upper bound to the effective vertical permeability.

Hypothetical confining strata for shale fractions of 0.66 and 0.88 are shown in Figs. 1 and 2, respectively, for the particular case of uniform thickness shale layers. In these configurations, white and dark spaces represent sand and shale

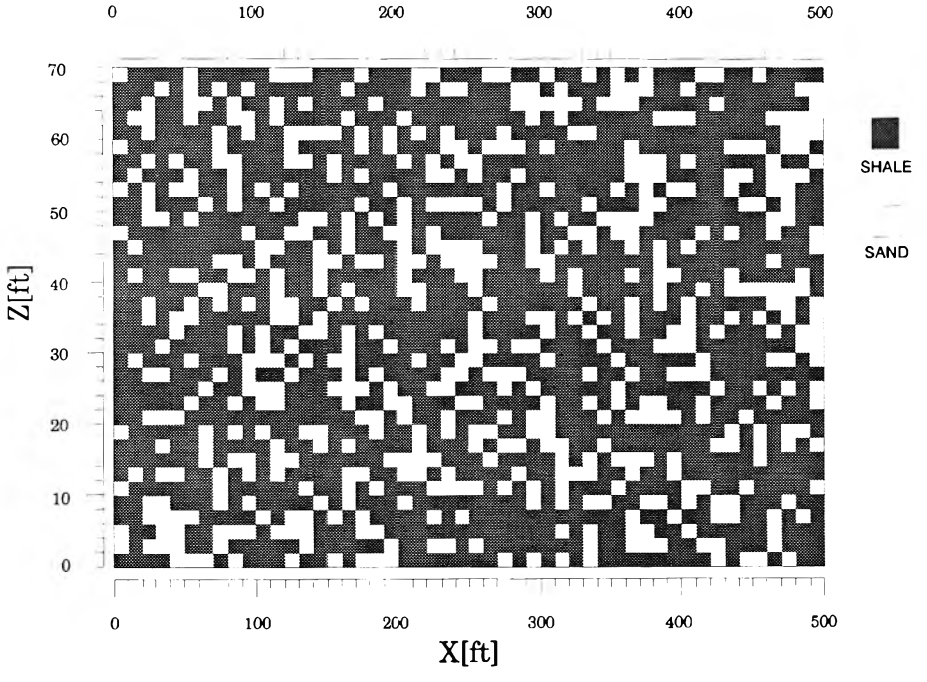

Fig. 1. Hypothetical confining strata at shale fraction 0.66. (Note that the vertical scale is exaggerated with respect to the horizontal scale.)

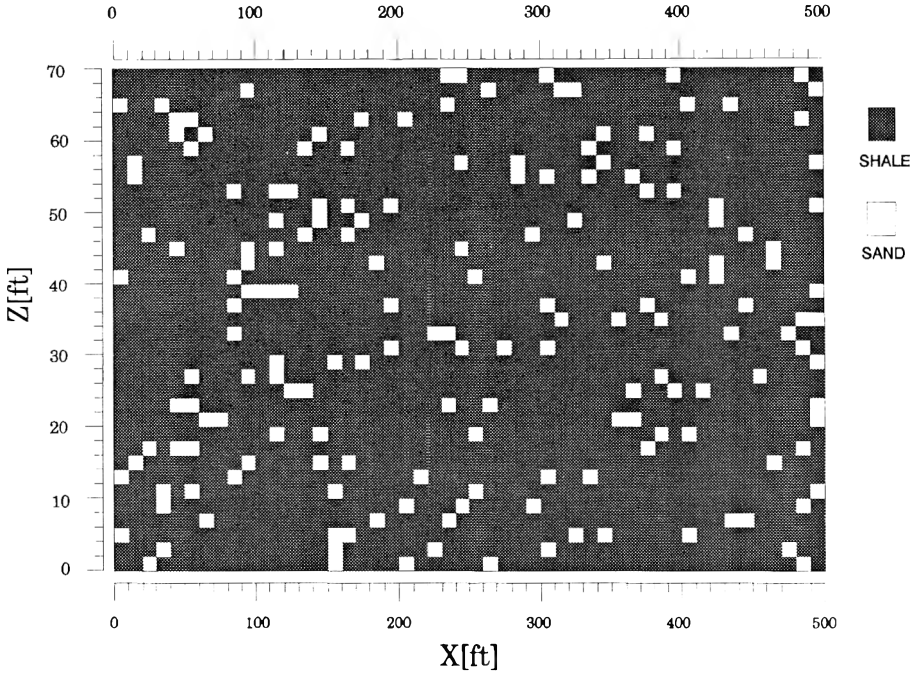

Fig. 2. Hypothetical confining strata at shale fraction 0.88. (Note that the vertical scale is exaggerated with respect to the horizontal scale.)

regions, respectively. These figures represent only a part of the configuration (i.e. 70 ft [21.34 m] of the total simulated confining layer depth of 300 ft (91.44 m). For all shale fractions greater than about 0.65, sand zones are isolated by shale regions.

For a 2D configuration of confining layers, the shales are continuous in the third dimension so that the flow may be blocked by continuous shales in that direction. If shales are not continuous in the third direction, the availability of permeable flow paths may increase. A preliminary 3D modeling effort was initiated to examine the potential for enhanced flow in a 3D system. The same principles as those utilized in the 2D descriptions were used to generate the configuration in the third-dimension. The 3D configuration is generated by combining each 2D independent configuration laterally. In the 3D configuration, the aspect ratio of width to thickness of shale zone was fixed at 1. The potential for continuous permeable sand veins and therefore a high vertical permeability is maximized with this aspect ratio.

Numerical simulation of flow in confining layers

Subsurface flow in confining layers depends mainly on the sand distribution because of the low permeability of shale. According to Freeze and Cherry [28],

the range of shale permeability is from 0.00001 mdarcy to 0.1 mdarcy. These shale permeabilities are typically several orders of magnitude lower than the intrinsic sand permeability. In this study, shale permeability is assumed to be of the order of 0.0001 mdarcy and sand permeability of order 1000 mdarcy a ratio of 10^7. This is the magnitude of the permeabilities measured by Constant and Clark [29] using samples of shale from disposal wells in Jefferson Parish, Louisiana. The modeled confining layer configuration of randomly placed sand and shale zones is extremely heterogeneous. A non-uniform finite element grid is used to perform the flow simulation in the heterogeneous porous media. Previous work by Desbarats [12] was limited to a sand–shale permeability ratio of 10^4.

The 3D steady-state subsurface flow in an incompressible saturated confining layer is governed by [28]:

$$\frac{\partial}{\partial x}\left(K_x \frac{\partial h}{\partial x}\right)+\frac{\partial}{\partial y}\left(K_y \frac{\partial h}{\partial y}\right)+\frac{\partial}{\partial z}\left(K_z \frac{\partial h}{\partial z}\right)=0, \tag{1}$$

where K_i represents hydraulic conductivity in ith direction and h is the hydraulic head. Constant head boundary conditions are specified in the mean (vertical) direction of flow, and no flow conditions are imposed on side boundaries.

The finite element method based on the Galerkin technique is used to formulate the model of the two-dimensional movement of hazardous wastes in confining layers. The numerical model utilizes linear triangular elements. Even though a Monte Carlo technique is applied to generate the confining layer configuration, any individual configuration is deterministic. The Monte Carlo technique is used to generate an ensemble of configurations, and the deterministic model is used to solve the flow problem for each configuration. The means and variances of the hydraulic head and effective permeability obtained from the set of deterministic solutions should indicate the expected value and uncertainty in these parameters in the real subsurface formation.

The flow calculation and determination of the effective permeability is repeated for each generated configuration of the confinement zone. Reduced effective vertical permeabilities for each configuration are defined by dividing the effective vertical permeabilities by sand permeability. To get the expected value of the effective vertical permeability of the confinement zone, the geometric mean permeability of up to 600 different configurations is used at the same shale fractions. If the expected value of effective vertical permeability is estimated by arithmetic mean, the expected value is extremely overestimated. After 300 configurations there is little change in the expected value of effective vertical permeability with the number of configurations. The 95% confidence limits are determined directly from the observed distribution of the calculated effective permeabilities.

Since the range of possible effective permeability may increase in higher dimensions, the three-dimensional flow problems were investigated by using the Finite Difference Method computer tool MODFLOW [30]. The flow system is discretized by a block-centered, and $30 \times 40 \times 30$ nodal grid. The flow equation, which is approximated by a standard seven-point finite difference scheme, is solved by using slice successive overrelaxation (SSOR).

Numerical simulation of solute transport

The general governing equation describing the two-dimensional solute transport in a saturated, essentially incompressible porous medium is [31]

$$R_f \frac{\partial C}{\partial t} + \frac{\partial}{\partial x}(v_x C) + \frac{\partial}{\partial z}(v_z C) = \frac{\partial}{\partial x}\left(D_x \frac{\partial C}{\partial x}\right) + \frac{\partial}{\partial z}\left(D_z \frac{\partial C}{\partial z}\right) \tag{2}$$

where C represents the constituent concentration in solution, R_f is retardation factor, t is time, v_i is the velocity in the ith direction, D_i is the hydrodynamic dispersion coefficient in the ith direction. Initial condition is zero concentration in the domain of confining strata. No flux boundary conditions are imposed in the x-direction and constant concentration boundary conditions were specified in the z-direction. Since the horizontal hydraulic head difference is much less than the vertical hydraulic head difference in the results of the flow simulations, horizontal advection is negligible under the conditions simulated.

The components of the dispersion tensor have contributions from both mechanical dispersion and molecular diffusion. The principal values of the dispersion tensor **D** are given by

$$D_x = \alpha_T v_z + D_{eff}, \tag{3a}$$

$$D_z = \alpha_L v_z + D_{eff}, \tag{3b}$$

where α_L is the longitudinal (vertical) dispersivity, α_T is the transverse (lateral) dispersivity, and D_{eff} is the effective diffusivity. The longitudinal dispersivity or dispersivity in the direction of travel usually scales with the characteristic size of the heterogeneities of the media.

For advection dominated transport (Peclet number, $Pe \approx v\Delta z/D_{eff} > 1$), a conventional finite element model is generally inappropriate. In this case, however, the maximum value of the Peclet number, which represented the ratio of advection to diffusion, varied from 0.33 to 0.85 as the shale fraction was decreased from 0.88 to 0.66. Since the Peclet number is of order of unity or less at these high shale fractions, the advection–diffusion model of solute transport is solved using the Galerkin finite element method with the distribution of real velocity fields obtained from the steady state flow equation. The Galerkin finite element calculation procedure employed for flow and transport equations is an

adaptation of that described by Smith and Griffiths [32]. A fully implicit backward difference scheme is employed for the time derivative.

The size of the hypothetical configuration of confining strata was 200 ft (60.96 m) in depth and 500 ft (152.4 m) in width. In the numerical simulation of flow and transport in the hypothetical formation, an irregular array of nodal points were assigned to conform to the complex geometry of the medium. Due to computational limitations, only a single generated configuration at each shale fraction was used in the transport modeling. At the high shale fractions used, however, flow modeling suggested that the effective permeability or average flow was insensitive to the particular subsurface configuration. The transport field was discretized by a 100×50 nodal grid. Numerical simulations were performed for four hypothetical configurations with 0.66, 0.7, 0.8 and 0.88 shale fraction over 10,000 years.

Recently, Neuman [33] investigated the universal scaling of dispersivities in geological media. He showed that the dispersivity data from laboratory and field tracer studies in porous and fractured media increased with the distance traveled. He suggested the following formulation for the universal dispersivity as a function of the characteristic length for travel distance, L_s:

$$\alpha = 0.017\, L_s^{1.5}, \tag{4}$$

where L_s is in meters. The formula is limited to $L_s < 100$ m. Maximum travel distances of contaminant concentrations within an order of magnitude of that at the injection point are of the order of 10–20 m. Equation (4) suggests a travel distance of 15 m corresponds to a dispersivity of about 1 m. This should be a reasonable upper bound for dispersivity in that the dispersion attributable to heterogeneities at the layer depth scale and larger is explicitly modeled. Only the subgrid scale should be modeled with an effective dispersion coefficient.

The effective diffusivity in the sand was estimated from the model of Millington and Quirk [34]. The effective diffusivity in the shale was as estimated by Berner [35]. The effective diffusivity for shale, corrected for tortuosity, assumed in this study is the same as that used by Ranganathan and Hanor [36]

$$D_{\text{eff}} = D_{\text{m}} \varepsilon^3 \tag{5}$$

and for sand [34]

$$D_{\text{eff}} = D_{\text{m}} \varepsilon^{1/3}, \tag{6}$$

where D_{m} is molecular diffusivity and ε is the porosity. For comparison, the diffusion controlled problem was also investigated by neglecting the advection term in the solute transport equation.

In eq. (2) it has been assumed that the chemical interaction of contaminant and subsurface soils is limited to linear, reversible sorption. If local linear

equilibrium is assumed, a retardation factor due to sorption can be defined as [28]

$$R_f = 1 + \rho_b K_d / \varepsilon, \tag{7}$$

where ρ_b is the bulk mass density of the porous medium, and K_d is the partition coefficient. The retardation factor, R_f, represents the velocity of the subsurface fluid relative to that of the primary constituent and results from the accumulation of contaminant in the immobile as well as mobile phase. For a partition coefficient that is orders of magnitude larger than unity, the solute is essentially immobile [28]. Since the sorption of hydrophobic compounds (e.g. aromatic hydrocarbons and chlorinated hydrocarbons) in sand is much smaller than that in silt and clay [37], sorption in sand regions is assumed to be negligible in these simulations ($R_f = 1$). The content of organic carbon in shale is typically less than 0.3%. For organic carbon contents greater than 0.1%, partitioning is typically dominated by organic carbon. Thus, an organic carbon based partition coefficient can be used to estimate sorption [38]. The partition coefficient for any given soil is the product of the organic carbon based partition coefficient K_{oc} and the weight fraction of organic carbon f_{oc} in the soil (i.e. $K_d = K_{oc}\, f_{oc}$). Among the compounds that have been observed as trace components of a particular deep-well injected waste are acrylonitrile ($K_{oc} = 0.85$), 1,2-dichloroethane (EDC, $K_{oc} = 14$), and methylmethacrylate ($K_{oc} = 840$) [39]. Assuming 0.3% (w/w) organic carbon, the partition coefficients of these compounds range from 0.0026 for acrylonitrile to 2.52 for methylmethacrylate. The range of the shale partition coefficient employed in the model was thus varied from 0 to 3 and the retardation factor from 1 to 17.7.

Acrylonitrile will be used here as an example for the purposes of estimating solute transport. A particular deep well injection stream contains acrylonitrile with a concentration of 760 mg/L while the drinking water standard is 5.8×10^{-5} mg/L. Hence, the required dilution ratio for which containment must be demonstrated over the 10,000 year period is 7.6×10^{-8} [40]. The free-water diffusivity of acrylonitrile is 1.66×10^{-5} cm/s at assumed down-hole conditions of temperature 110 °F (43.3 °C) and pressure 1100 psi (74.83 atm) [41].

Results and discussion

Subsurface flow

Figure 3 shows the 95% confidence limits on effective vertical permeabilities in the case of an isotropic two-dimensional formation with unit shale aspect ratio at various shale fractions. These confidence limits are based on a statistical analysis of the 600 simulations conducted at each shale fraction and indicate the sensitivity of the effective permeability to a particular subsurface configuration. In the case of high shale fractions, the flow path remains blocked for all sand–shale configurations. Conversely, at low shale fractions,

there is always a connecting sand flow path through the hypothetical confinement zone. At these two extremes of shale fraction, the uncertainty or variability in the effective vertical permeability is small and the effective permeability is independent of the particular configuration of the sand–shale formation. Since the blocking of flow paths depends on the particular configuration when the shale fraction is between about 0.5 and 0.6, the uncertainty or variability in the effective vertical permeability is largest in this case.

Estimates of effective vertical permeability in individual three-dimensional flow systems are also presented in Fig. 3. As the shale fraction of the confining layers increases, the number of iterations required for convergence in the predicted hydraulic head field increases due to flow blockage by the low permeability shale. Convergence is generally not obtained at high shale fractions unless the ratio of sand to shale permeability is much smaller [24]. In general, the effective vertical permeability for a three-dimensional flow system is within the range of uncertainty of the two-dimensional flow simulations. At low shale fraction there was little difference between the two dimensional and three dimensional simulations. At shale fractions above 0.70, shale blocking of

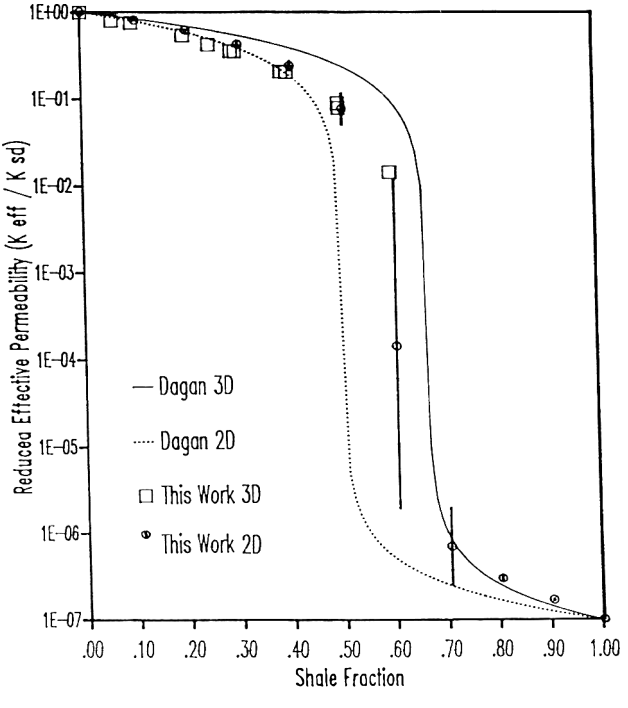

Fig. 3. Comparison of effective permeability between numerical results and Dagan's solutions. (Solid vertical lines associated with 2D numerical results represent 95% confidence limits.)

transport paths occurred and the effective permeability of the medium effectively approached that of pure shale. Only for intermediate shale fractions is there a potential effect of three dimensional versus two dimensional formation behavior.

This is also shown by examining the theoretical results of Dagan [13]. He employed the self-consistent approximation in which the media surrounding a certain element are treated as homogeneous with the global effective permeability. For the binary distribution and isotropic formation, the self-consistent formula of effective permeability from Dagan's paper reduces to

$$K_{\text{eff}} = \frac{1}{m}\left[\frac{F_{\text{sd}}}{(m-1)K_{\text{eff}} + K_{\text{sd}}} + \frac{F_{\text{sh}}}{(m-1)K_{\text{eff}} + K_{\text{sh}}}\right]^{-1}, \tag{8}$$

where K_{eff} is the effective permeability, K_{sh}, F_{sh} and K_{sd}, F_{sd} represent permeability and fraction of medium respectively for shale and sand, and m is 2 or 3 for two- and three-dimensional flows, respectively. In Fig. 3, the dotted line represents effective permeabilities for a two-dimensional flow system and the solid line represents effective permeabilities for a three-dimensional flow system. For $K_{\text{sd}} \gg K_{\text{eff}} \gg K_{\text{sh}}$ and $F_{\text{sd}} \sim F_{\text{sh}}$, Dagan's model suggests the effective permeability of a 3D system is much higher than that of a 2D system. Agreement between Dagan's analytical results and the simulations is satisfactory for shale fractions of less than about 0.5 or greater than 0.7.

Using information from a hazardous waste disposal well in Jefferson Parish, Louisiana as a field example, effective vertical permeabilities were calculated based on well log data. In this calculation, measured shale permeabilities were about 0.0005 mdarcy. The average shale fraction of the confining layer was 82%. Effective porosity was assumed to be 0.3. Isotropy was assumed to provide a higher than expected estimate of vertical migration. The mean vertical velocity of injected hazardous wastes was calculated from the expected value of the effective vertical permeability by using Darcy's law and the surface injection pressure as an upper bound to the actual driving pressure. The estimated mean vertical velocity was 0.03 cm/year. Over 10,000 years, therefore, the waste would be expected to penetrate only 3 m on average [27].

Contaminant transport

The maximum pressure difference across the confining layer was estimated by the injection pressure at 15.5 atm. As an upper bound to advective transport, waste injection and therefore injection pressure was assumed constant for the entire 10,000 years. If the injection of hazardous wastes was only continued for a finite time, the driving pressure would decrease and advective transport would result only from natural hydraulic head differences. Simulations assuming an injection period of less than 100 years yielded results after 10,000 years essentially identical to those assuming only diffusion was operative.

Desbarats [24] showed that vertical macrodispersive spreading is slightly greater in the stratified case than in the isotropic case. The effective vertical permeability and therefore the mean flow velocity, however, would decrease significantly as the aspect ratio increased, offsetting this effect [14, 27]. Hence, the choice of a shale aspect ratio of one provides an upper bound to flow and solute transport.

For steady-state flow and transient solute transport conditions, the two-dimensional Galerkin finite element method was applied to get individual concentrations in an isotropic formation. From the individual concentrations at each node, concentration isopleths were developed for the formations exhibiting shale fractions of 0.66, 0.7, 0.8 and 0.88. Concentration isopleths in the hypothetical confining layer were estimated at 10,000 years subject to both advection–dispersion and diffusion alone. The concentration isopleths for diffusion cases are represented in Figs. 4(a) and 5(a) and the concentration isopleths for advection–dispersion cases are shown in Figs. 4(b) and 5(b). The concentration isopleths generally matched the sand distribution in the configuration, that is, significant penetration of the confining layer was noted only where sand streaks existed. Schematic representations of hypothetical confining layers with different shale fractions have been described in Figs. 1 and 2.

The degree of horizontal non-uniformity of concentrations in the confining layer decreased as shale fraction increased. The degree of the non-uniformity of concentration also decreased as penetration of the confining layer increased. Over 10,000 years at a shale fraction of 0.66, the maximum vertical penetration of concentrations exceeding 0.1 (i.e 10% of injection concentration) by diffusion is 43 ft (13.11 m), while for advection–dispersion assuming a 10,000 year injection period is 61 ft (18.59 m). In these cases, the retardation factor was assumed to be unity in order to obtain the upper bound of vertical penetration. The difference in concentration between diffusion cases and advection–dispersion cases decreased as shale fraction was increased.

Mean concentration profile

The mean concentration profiles with depth were obtained for the diffusion case and advection–dispersion case using simple averaging along the width. As indicated above, the horizontal fluctuations from the mean decreased with depth into the confining layer. Figure 6 compares the mean concentration profiles for diffusion only with those for advection–dispersion at shale fraction 0.8. There is little difference in the mean concentration profiles before 1,000 years. At 10,000 years, however, the mean concentration results of advection–dispersion case are higher than those of the diffusion case. Since the vertical interstitial velocity was very small, solute transport was not affected by advection at shorter times. Results show the travel distance of acrylonitrile to a location where concentrations were 10 percent of that injected is about 41 ft (12.5 m).

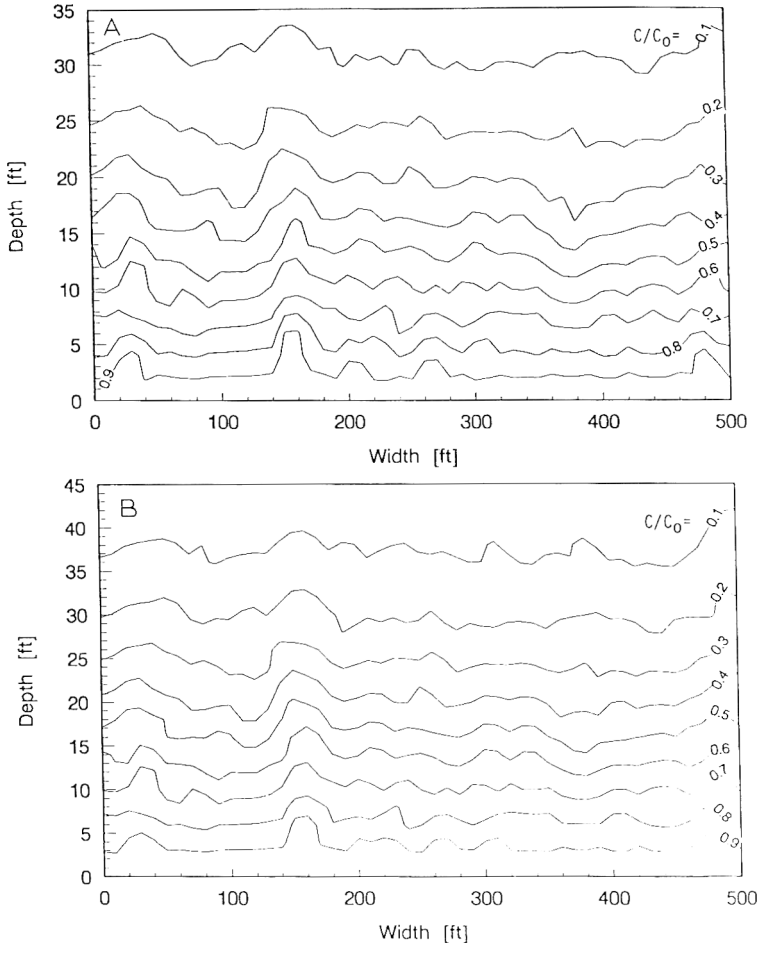

Fig. 4(A). Concentration isopleth for diffusion at shale fraction 0.66 after 10,000 years. (B) Concentration isopleth for advection–dispersion at shale fraction 0.66 after 10,000 years.

In order to investigate the effect of sorption related retardation on transport in confining layers, partition coefficients of 0, 0.25, 0.5, 1, and 3 were used in the advection–dispersion equation. In this case, the shale fraction was 0.66. Since there was little interaction between hazardous wastes and sand, a partition coefficient was only applied to the shale regions. In shale zones, the bulk density of the solid phase and the porosity in shale were assumed to be 1.67 and 0.3, respectively. The retardation factor was changed from 1 to 17.7 as a result of the variation of the partition coefficient between 0 and 3. Figure 7 illustrates the effect of partition coefficients on the mean concentration profile after 10,000 years. The travel distance in the direction of mean flow at dimensionless concentration 0.5 is inversely proportional to $\sqrt{R_f}$. Even though the retardation factor was only applied to randomly placed shale zones, the trend of this

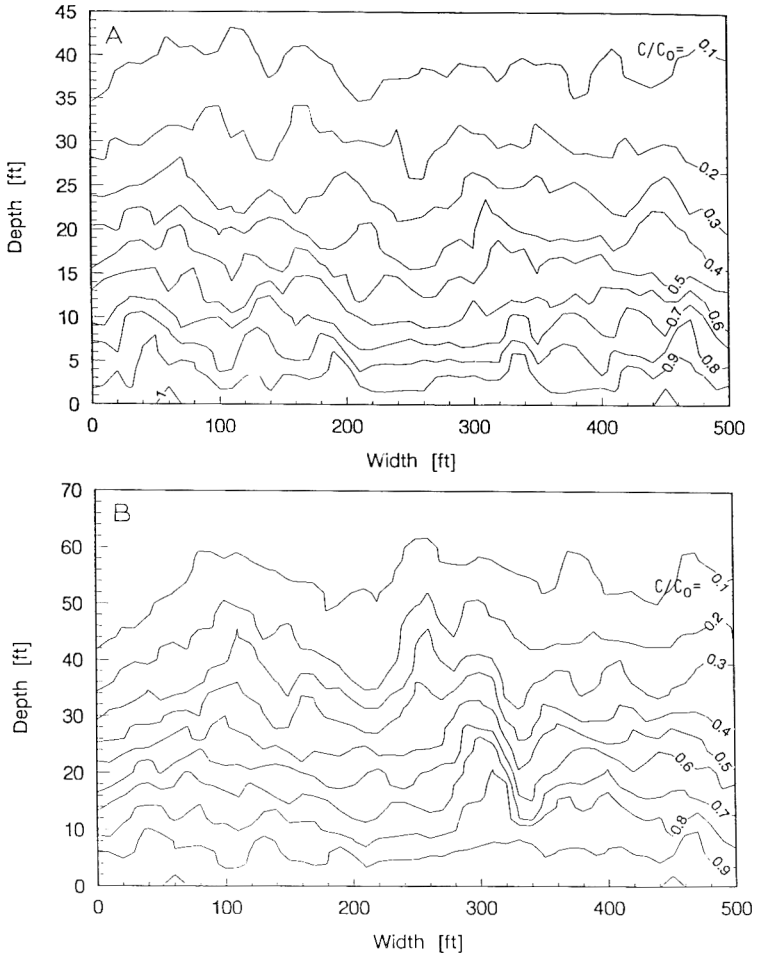

Fig. 5(A). Concentration isopleth for diffusion at shale fraction 0.88 after 10,000 years. (B) Concentration isopleth for advection–dispersion at shale fraction 0.88 after 10,000 years.

result is identical to that expected for pure shale formations. Hence, the model again illustrates that solute transport through the sand–shale formation was dominated by the hydrodynamic properties of shale regions in higher shale fractions.

Penetration depth

To insure containment of the injected wastes, it is desired to estimate the depth of penetration of concentrations exceeding drinking water standards. The distance to achieve a given dilution ratio for various shale fractions is shown in Fig. 8. The required dilution ratio to achieve drinking water standards for acrylonitrile is 7.6×10^{-8} in the example waste stream. Table 1 presents the mean penetration depth based on meeting the required dilution for

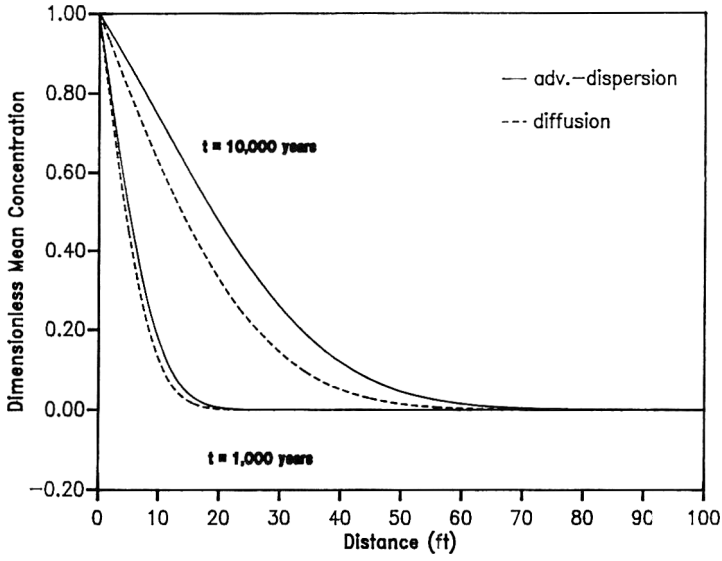

Fig. 6. Comparison of mean concentration between diffusion and advection–dispersion with time at shale fraction 0.8.

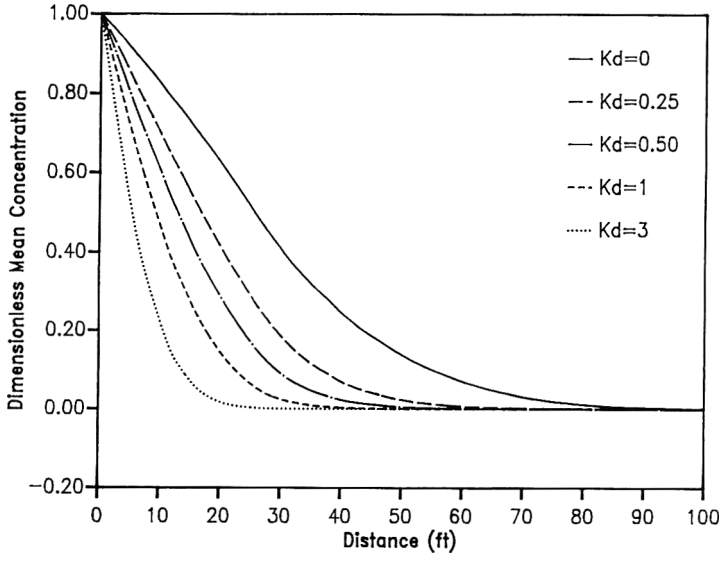

Fig. 7. Effect of partition coefficient to mean concentration at shale fraction 0.66 after 10,000 years.

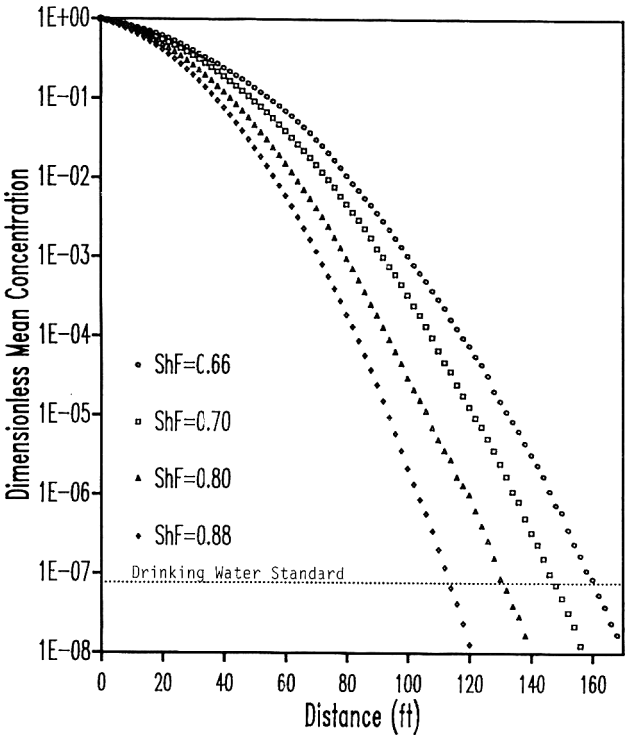

Fig. 8. Mean concentration profiles for advection–dispersion with shale fraction after 10,000 years.

TABLE 1

Mean penetration depth for advection–dispersion and diffusion with the change of shale fraction in 10,000 years

Shale fraction	Mean penetration depth (m)	
	Advection–dispersion[a]	Diffusion
0.66	48.4	38.9
0.70	44.6	37.7
0.80	38.8	33.9
0.88	34.6	31.0

[a] Injection for entire 10,000 year period.

both diffusion and advection–dispersion after 10,000 years. The mean penetration depth was inversely proportional to the shale fraction in both advection–dispersion and diffusion. Lateral variability led to deeper penetration in some areas than in others. Table 2 shows the equivalent maximum penetration depths based on the mean concentration profiles plus two standard deviations.

TABLE 2

Maximum penetration depth for advection–dispersion and diffusion with the change of shale fraction 10,000 years

Shale fraction	Maximum penetration depth (m)	
	Advection–dispersion[a]	Diffusion
0.66	53.0	42.5
0.70	48.5	41.0
0.80	44.0	37.6
0.88	37.1	33.0

[a] Injection for entire 10,000 year period.

The maximum penetration depth for advection–dispersion after 10,000 years is less than 200 ft (60.96 m).

The simulation suggests that the injected hazardous wastes will be confined in the disposal zone for the EPA required 10,000 years. This analysis does not consider, however, the effect of loss of integrity of the injection well resulting in injection outside of the confining layer or the effect of non-random artificial penetrations of the confining layers such as unsealed inactive oil production wells. In addition, estimates with a lower than 50% shale fraction confining layer suggested that deep-well injection in such a geology could result in waste penetration of the 200 ft confining layer within 500 years if the injection pressure were maintained throughout. These results are also dependent on the accuracy of the estimated diffusion coefficient. An error by an order of magnitude in effective diffusion coefficient would change the effective penetration depth by diffusion alone by a factor of three.

Summary and conclusions

Hypothetical confining layers were modeled as a combination of binary random structures composed of either pure sand or pure shale. Monte Carlo techniques were used to generate the configuration of confining layers. Flow and solute transport assuming a constant pressure driving force over 10,000 years, 100 years and with diffusion alone were investigated by using the Galerkin finite element method for four hypothetical configurations with shasle fractions of 0.66, 0.7, 0.8, and 0.88.

At low shale fractions, less than 0.4, the effective permeability of the formation was essentially that of pure sand. At high shale fractions, greater than 0.65–0.7, the effective permeability of the formation was essentially that of pure shale. At either of these extremes, the effective permeability and the average flow and transport behavior was insensitive to the particular sub-surface configuration. Two- and three-dimensional estimates of effective

permeability of the subsurface formation are also similar at low shale fraction.

Transport modeling showed deeper penetration of deep-well injected contaminants in local sand veins. Since sand veins were not continuous throughout the modeled confining layer at high shale fractions, the maximum penetration was still small for the confining layer structures considered. The degree of horizontal non-uniformity of concentrations decreased as shale fraction or depth into confining layer increased.

Comparison between an advection–dispersion model and a diffusion only model showed differences that increased with time. These differences decreased as shale fraction increased because advection decreased with increasing shale fraction. Sorption in the heterogeneous confining layer significantly retarded the movement of a compound, despite the assumption that only limited sorption occurred primarily in shale zones.

In a particular injected waste and subsurface geology, the mean and the maximum penetration depths of waste water containing acrylonitrile concentrations in excess of drinking water standards over 10,000 years were less than 200 ft (60.96 m). These penetration depths were less than the thickness of the confining layers, which were usually greater than 300 ft (91.44 m).

Acknowledgment

This research was supported in part by members of the Louisiana Chemical Association in an unrestricted grant through the Hazardous Waste Research Center and the LSU Foundation at Louisiana State University.

References

1 W. Gordon and J. Bloom, Limits to underground injection as a hazardous waste disposal method, Hazard. Waste Hazard. Mater., 2(4) (1985) 411–451.
2 Federal Register, 40 CFR 124, 144, 148, 52(166), Washington, DC, August, 1987.
3 G.E. Fogg, Groundwater flow and sand body interconnectedness in a thick, multiple-aquifer system, Water Resour. Res., 22(5) (1986) 679–694.
4 S.E. Silliman and A.L. Wright, Stochastic analysis of paths of high hydraulic conductivity in porous media, Water Resour. Res., 24(11) (1988) 1901–1910.
5 L. Smith and R.A. Freeze, Stochastic analysis of steady state groundwater flow in a bounded domain. 1. One-dimensional simulation, Water Resour. Res., 15(6) (1979) 521–528.
6 L. Smith and R.A. Freeze, Stochastic analysis of steady state groundwater flow in a bounded domain. 2. Two-dimensional simulation, Water Resour. Res., 15(6) (1979) 1543–1559.
7 J.E. Warren and H.S. Price, Flow in heterogeneous porous media, Soc. Pet. Eng. J., 1 (1961) 153–169.
8 A.A. Bakr, L.W. Gelhar, A.L. Gutjahr and J.R. McMillan, Stochastic analysis of spatial variability in subsurface flow. 1. Comparison of one- and three-dimensional flows, Water Resour. Res., 14(2) (1978) 263–271.

9 A.L. Gutjahr, L.W. Gelhar, A.A. Bakr and J.R. McMillan, Stochastic analysis of spatial variability in subsurface flow. 2. Evaluation and application, Water Resour. Res., 14(5) (1978) 953–959.
10 L.W. Gelhar and C.L. Axness, Three-dimensional stochastic analysis of macrodispersion in aquifers, Water Resour. Res., 19(1) (1983) 161–180.
11 G. Matheron, Composition des permeabilities en milieu poreux hétérogène: Méthode de Schwydler et règles de ponderation, Rev. Inst. Fr. Pet., 22 (1967) 443–466.
12 A.J. Desbarats, Numerical estimation of effective permeability in sand-shale formations, Water Resour. Res., 23(2) (1987) 273–286.
13 G. Dagan, Models of groundwater flow in statistically homogeneous porous formations, Water Resour. Res., 15(1) (1979) 47–63.
14 J.W. Kramers, S. Bachu, D.L. Cuthiell, M.E. Prentice and L.P. Yuan, A multidisciplinary approach to reservoir characterization: the Provost upper Mannville B pool, J. Can. Pet. Technol., 28(3) (1989) 1–11.
15 H.H. Haldorsen and L.W. Lake, A new approach to shale management in field scale methods, Soc. Pet. Eng. J., August (1984) 447–457.
16 S.H. Begg, D.M. Chang and H.H. Haldorsen, A simple statistical method of calculating the effective vertical permeability of a reservoir containing discontinuous shales, In: Proc. 60th Annu. Tech. Conf., Soc. of Pet. Eng., Las Vegas, NV, Sept. 1985 pp. 22–25.
17 L.W. Gelhar, A.L. Gutjahr and R.L. Naff, Stochastic analysis of macrodispersion in a stratified aquifer, Water Resour. Res., 15(6) (1979) 1387–1397.
18 J.F. Pickens and G.E. Grisak, Scale-dependent dispersion in a stratified granular aquifer, Water Resour. Res., 17(4) (1981) 1191–1211.
19 G. Dagan, Time-dependent macrodispersion for solute transport in anisotropic heterogeneous aquifers, Water Resour. Res., 24(9) (1988) 1491–1500.
20 G. Dagan, Solute transport in heterogeneous porous formations, J. Fluid Mech., 145 (1984) 151–177.
21 G. Dagan, Statistical theory of groundwater flow and transport: Pore to laboratory, laboratory to formation, and formation to regional scale, Water Resour. Res., 22(9) (1986) 120s–134s.
22 S.P. Neuman, C.L. Winter and C.M. Newman, Stochastic theory of field-scale Fickian dispersion in anisotropic porous media, Water Resour. Res., 23(3) (1987) 453–466.
23 A.F.B. Tompson and L.W. Gelhar, Numerical simulation of solute transport in three-dimensional, randomly heterogeneous porous media, Water Resour. Res., 26(10) (1990) 2541–2562.
24 A.J. Desbarats, Macrodispersion in sand-shale sequences, Water Resour. Res., 26(1) (1990) 153–163.
25 G. Segol, G.F. Pinder and W.G. Gray, A Galerkin-finite element technique for calculating the transient position of the saltwater front, Water Resour. Res., 11(2) (1975) 343–347.
26 W.E. Galloway, D.K. Hobday and K. Magara, Frio formation of the Texas Gulf Coast Basin — Depositional systems, structural framework, and hydrocarbon origin, migration, distribution, and exploration potential, Report of Investigations No. 122, University of Texas at Austin, Bureau of Economic Geology, Austin, TX, 1982, p. 78.
27 S.W. Rhee, D.D. Reible and W.D. Constant, Simulation of the effects of shale heterogeneities on effective permeability in deep-well injection disposal systems, Fluid/Particle Sep. J., 4(4) (1991) 204–210.
28 R.A. Freeze and J.A. Cherry, Groundwater, Prentice-Hall, Englewood Cliffs, NJ, 1979.
29 W.D. Constant and D.A. Clark, Experimental evaluation of containment properties for shale associated with deep-well hazardous waste injection zone, Proc. 6th Conf. and Exhibition on Hazardous Waste and Hazardous Material, New Orleans, LA, April 1989, pp. 182–187.

30 M.G. McDonald and A.W. Harbaugh, A modular three-dimensional finite difference ground-water flow model U.S. Geological Survey, Ruston, VA, 1988.
31 J. Bear, Dynamics of Fluids in Porous Media, Elsevier, New York, 1972.
32 I.M. Smith and D.V. Griffiths, Programming the Finite Element Method, 2edn., Wiley, New York, 1988.
33 S.P. Neuman, Universal scaling of hydraulic conductivities and dispersivities in geologic media, Water Resour. Res., 26(8) (1990) 1749–1758.
34 R.J. Millington and J P. Quirk, Permeability of porous solids, Trans. Faraday Soc., 57 (1961) 1200–1207.
35 R.A. Berner, Early Diagenesis: A Theoretical Approach, Princeton University Press, Princeton, NJ, 1980.
36 V. Ranganathan and J.S. Hanor, Density-driven groundwater flow near salt domes, Chem. Geol., 74 (1988) 173–188.
37 S.W. Karickhoff, D.S. Brown and T.A. Scott, Sorption of hydrophobic pollutants on natural sediments, Water Res., 13 (1979) 241–248.
38 W.J. Green, G.F. Lee, R.A. Jones and T. Pallt, Interaction of clay soils with water and organic solvents: Implications for the disposal of hazardous wastes, Environ. Sci. Technol., 17 (1983) 278–282.
39 U.S. EPA., Superfund public health evaluation manual. Draft. Prepared by ICF, Inc. for the Policy Analysis Staff, Office of Emergency and Remedial Response, Washington, DC. U.S. Environmental Protection Agency, October 1, 1985.
40 INTERA Technologies, Inc., Mathematical modeling for the American Cyanamid Fortier Facility, Austin, TX, 1988.
41 W. Hayduk and H. Laudie, Prediction of diffusion coefficients for nonelectrolytes in dilute aqueous solutions, AIChE J., 20 (1974) 611–615.

Journal of Hazardous Materials, 34 (1993) 335–361
Elsevier Science Publishers B.V., Amsterdam

Evaluation of volumetric leak detection systems for large underground tanks

Joseph W. Maresca, Jr[a,*], James W. Starr[a], Richard F. Wise[b], Robert W. Hillger[b] and Anthony N. Tafuri[b]

[a] *Vista Research, Inc., Mountain View, CA 94042 (USA)*
[b] *Risk Reduction Engineering Laboratory, U.S. Environmental Protection Agency, Edison, NJ 08837 (USA)*

(Received May 10, 1991; accepted in revised form December 2, 1992)

Abstract

The performance standard for tank tightness testing established by the U.S. Environmental Protection Agency (EPA) regulation requires that the systems used to test underground storage tanks be able to detect leaks as small as 0.38 L/h (0.1 gal/h) with a probability of detection of 0.95 and a probability of false alarm of 0.05. This standard was developed to address tanks nominally 30,000 to 38,000 L (8,000 to 10,000 gal) in capacity or less, but also applies to tanks as large as 190 000 L (50,000 gal). The accuracy of detecting leaks in tanks as large as 190,000 L (50,000 gal) is not well known, and very little data from which to make an assessment are available. To meet EPA's regulatory standards for tank tightness testing of petroleum fuel tanks, volumetric leak detection systems must be able to accurately compensate for thermally induced volume changes in the stored fuel. A field study was done to investigate the magnitude of these volume changes. Three 24-h experiments were conducted in two partially filled, 190,000-L (50,000-gal) tanks in upstate New York during late August 1990; product was either added to or removed from the tank to initiate each experiment. The study showed that the procedures used to compensate for the thermally induced volume changes that occur during a tightness test performed on small tanks are not adequate for tanks as large as 190,000 L (50,000 gal). The volume of product in such tanks is large enough to cause significant errors in the estimates of the thermally induced volume changes required for compensation; these errors stem from the presence of horizontal and vertical gradients in the rate of change of temperature. In smaller tanks, the average rate of change of volume due to horizontal gradients is negligible, and a single vertical array of five temperature sensors is sufficient to compensate for the effects of thermal expansion of the product in a 1- to 2-h test. In larger tanks, however, a single array of temperature sensors does not suffice unless certain conditions are met. First, the number of sensors must be increased to at least 10 to ensure that the vertical gradients are accurately measured. Second, an adequate time (at least 24 h) must be allowed for the horizontal gradients to dissipate. Third, the duration of a test must be increased to at least 4 h so that the instrumentation and ambient volume fluctuations can be averaged. Fourth, the average rate of change of temperature in any one layer or in the tank as a whole must be small enough to allow accurate temperature compensation. Finally, an accurate experimental estimate of the constants necessary for converting level and temperature changes to volume must be made. Based on these experiments, a procedure has been developed for temperature compensation in tanks with capacities of 190,000 L (50,000 gal).

*To whom correspondence should be addressed.

Introduction

The United States Environmental Protection Agency (EPA) regulation for underground storage tanks (USTs), published on 23 September 1988, specifies the technical standards and a variety of release detection options for minimizing the environmental impact of tank leakage [1]. The regulation states that any volumetric leak detection system used as a tank tightness test must be able to detect leaks as small as 0.38 L/h (0.10 gal/h) with a probability of detection (P_D) of at least 0.95 and a probability of false alarm (P_{FA}) of 0.05 or better. Volumetric leak detection systems used as monthly tests, such as automatic tank gauging systems, must be able to detect leaks as small as 0.76 L/h (0.2 gal/h) with a P_D of 0.95 and a P_{FA} of 0.05. With several exceptions, the regulation applies to *shop-assembled* tanks, which range in size from small (a few hundred gallons in capacity) to very large, with no clearly defined upper limit.

The regulatory standards were based on the results of an extensive program of experiments conducted by the American Petroleum Institute (API) on 38,000-L (10,000-gal) tanks at retail stations to evaluate the performance of automatic tank gauging systems [2] and by the EPA on 30,000-L (8,000-gal) tanks at the EPA's UST Test Apparatus in Edison, New Jersey, to evaluate volumetric tank tightness tests [3–8]. Tanks found at many retail service stations are typically 30,000- to 38,000-L (8,000- to 10,000-gal) in capacity. Unfortunately, there is not enough information to determine whether volumetric leak detection systems can meet the regulatory standards when tests are conducted on tanks as large as 190,000-L (50,000-gal). The number of large tanks (defined as those between 57,000 and 190,000 L (15,000 and 50,000 gal) in capacity) represents a small but important portion of the total tank population. This number is increasing because of the preference of tank owners/operators for a smaller number of larger tanks to meet storage needs. Many large-volume storage facilities have tanks that are nominally 190,000 L (50,000 gal) in capacity.

Accurate tests are not possible unless the volume changes due to the thermal expansion or contraction of the product can be compensated for. Experiments conducted on the tanks at the UST Test Apparatus showed that a 1- to 2-h test with an array of five or more equally spaced temperature sensors, each weighted by the volume of product in the layer surrounding it, was sufficient to compensate for thermally induced volume changes providing that adequate waiting periods were observed after any addition of product to the tank. These waiting periods allow the large temperature fluctuations associated with any product addition (or removal) to subside, so that a single array of temperature sensors suffices to make an accurate estimate of the mean rate of change of temperature. As a means of minimizing the effect of these thermal inhomogeneities, waiting periods of at least 3 h after topping (as required when testing an overfilled tank) and 4 to 6 h or longer after a delivery were recommended; many leak detection systems use a 6- to 12-h waiting period after

a delivery to allow the deformation-induced volume changes to become negligible. Since a 190,000-L (50,000-gal) tank contains more than five times the volume of a 30,000- to 38,000-L (8,000- to 10,000-gal) tank, the error in temperature compensation will be at least five times greater than in a smaller tank.

A set of experiments was conducted on two partially filled, 190,000-L (50,000-gal) underground storage tanks to determine if the method used to compensate for the thermal expansion and contraction of the product in 30,000- to 38,000-L (8,000- to 10,000-gal) tanks could be applied to these larger tanks. The results of these experiments are summarized here; additional details can be found in [9].

Temperature compensation

It is normally assumed that a leak detection test will result in an accurate estimate of the leak rate (1) after the volume changes due to deformation, product temperature fluctuations, and evaporation and condensation produced by addition or removal of product preparatory to a test have subsided, and (2) after the thermal expansion or contraction of the product in the tank has been compensated for. For a partially filled tank, this assumption is valid provided that during a test the effects of evaporation and condensation at the vapor/product interface and at the wall/product/vapor interface are minimal. For an overfilled tank, the assumption is valid if the volume of trapped vapor is negligible.

Accurate temperature compensation requires a correct estimate of the average rate of change of temperature of the product in the tank. A single array of temperature sensors suffices provided that two conditions are met. The horizontal gradients in the rate of change of product temperature throughout the tank must be negligible, and the vertical spacing between sensors must be dense enough to permit an accurate estimate of the average rate of change in the layer of product surrounding each sensor. Assuming that the temperature field is horizontally uniform, each layer will then be thin enough that the change in temperature is linear within that layer, and a temperature sensor positioned in the middle of the layer will accurately measure the average rate of change of temperature throughout that layer. If the rate of change of temperature is not horizontally uniform at each level in the tank, even a very dense spacing of sensors will not provide accurate compensation.

The recommended practice for compensating for the thermal expansion and contraction of the product in a tank during a leak detection test is to estimate the average thermally induced volume change using an array of temperature sensors that measure the change in temperature at many levels in the tank. The thermally induced volume change, Δv, is usually estimated by means of the following equation:

$$\Delta v = \Sigma \Delta v_i = C_e \Sigma (V_i \Delta T_i) \quad (1)$$

The product in the tank is divided into n layers, and the thermally induced volume changes, Δv_i, produced by the temperature change, ΔT_i, in each layer, i, are summed, as indicated by the summation Σ, from $i=1$ to $i=n$. The temperature sensors are uniformly spaced from the top to the bottom of the tank, and each layer is centered on a temperature sensor; thus, each layer has the same vertical dimension. Normally, only one value for the coefficient of thermal expansion, C_e, is used in the calculation. A tank chart is used to estimate the volume of product in each layer, V_i, where the total volume of the product in the tank $V=\Sigma V_i$. The coefficient of thermal expansion is estimated from a table by means of API gravity measurements made with product samples taken from the tank.

Equation (1) indicates that, in estimating the thermally induced volume changes in the product inside a tank, the error due to any miscalculation of the value of C_e or ΔT_i will increase proportionally with the volume of product in each layer and the number of layers in the tank. Errors in temperature compensation that are negligible in 30,000- to 38,000-L (8,000- to 10,000-gal) tanks may be significant in tanks as large as 190,000 L (50,000 gal). The key to accurate temperature compensation is to divide the tank into enough layers that the uncertainty in the thermally induced rate of change of volume estimated in each layer is small, and to wait until any horizontal differences in temperature within the layer are negligible. This is particularly important in large tanks, in which the volume of product can be substantial. As shown in Table 1, the volume of product in a 31-cm (12-in.) layer can exceed 22,700 L (6,000 gal), an amount nearly as large as the entire capacity of the typical tank on which volumetric leak detection systems are normally used.

TABLE 1

Summary of the volume of product surrounding each thermistor on Arrays A and B

Thermistor channel		Thermistor height (cm (in.))	Volume of product (L (gal))
Array A	Array B		
13	0	125 (318)	14,703 (3,884)
11	9	113 (287)	13,859 (3,661)
10	6	101 (257)	16,922 (4,470)
17	5	89 (226)	20,942 (5,532)
18	19	77 (196)	22,430 (5,925)
16	2	65 (165)	22,998 (6,075)
14	1	53 (135)	22,714 (6,000)
24	8	41 (104)	21,548 (5,692)
23	7	29 (74)	19,341 (5,109)
22	4	17 (43)	15,631 (4,129)
20	3	5 (13)	8,097 (2,139)

The API tables [10] used to estimate the coefficient of thermal expansion were generated from measurements of the specific gravity of a large number of products. The coefficient is based not on a specific product but on many types of products having similar properties (e.g., different kinds of gasoline fuels). The tables have a one-standard-deviation uncertainty of 3.6%; therefore, the method used to estimate the coefficient of thermal expansion is accurate to 3.6%. Assuming that there is a 3.6% error in the coefficient, the error associated with a 0.01 °C/h change in the temperature of JP-4 fuel as measured by a thermistor in a 31-cm (12-in.) layer located at the center of a 190,000-L (50,000-gal) tank would be 0.009 L/h (0.0023 gal/h). This translates into a 0.072-L (0.019-gal/h) error if the tank is completely filled. By comparison, when tests are done in 30,000- to 38,000-L (8,000- to 10,000-gal) tanks, the rate of change of temperature can be measured and compensated for with an accuracy that is five to six times better.

In addition, the tank chart used to estimate volume can have an uncertainty of as much as 5%, primarily because the actual length or diameter of the tank may differ somewhat from the nominal dimensions used to generate the chart. This 5% uncertainty corresponds to an error of 0.098 L/h (0.026 gal/h) if the residual temperature changes are 0.01 °C/h. In practice, there are inherent errors in measuring the coefficient of thermal expansion and the volume of product used for compensation, and these errors cannot be reduced without significant effort or cost. The best way to minimize such errors is to avoid testing until the average rate of change of temperature has decreased acceptably.

The shaded portions in Fig. 1 indicate schematically those regions of the tank subject to the largest errors in estimating thermally induced volume changes by means of a single temperature array. In these regions, large horizontal or vertical gradients in the rate of change of temperature, or an insufficient number of temperature sensors for measuring these gradients, can produce errors large enough to affect the accuracy of temperature compensation.

The product's rate of change of temperature is controlled by the heat transfer (1) between the product inside the tank and the backfill surrounding it and (2) at the vapor/liquid interface within the tank, commonly called the product surface. This means that the rate of change of temperature is different at the centerline of the tank than it is in the vicinity of the walls. The rate of change of temperature near the wall of a 190,000-L (50,000-gal) tank is approximately the same as that of a 38,000-L (10,000-gal) tank. However, in a 190,000-L (50,000-gal) tank the volume of product in the region near the wall is five times greater than it is in a 38,000-L (10,000-gal) tank. Thus, small differences in temperature between the centerline and the walls, even though they may be insignificant in terms of their impact on thermal compensation in smaller tanks, cannot be ignored in the case of larger tanks.

The layers near the bottom of the tank are particularly susceptible to large errors because the rate of change of temperature is often greatest in this

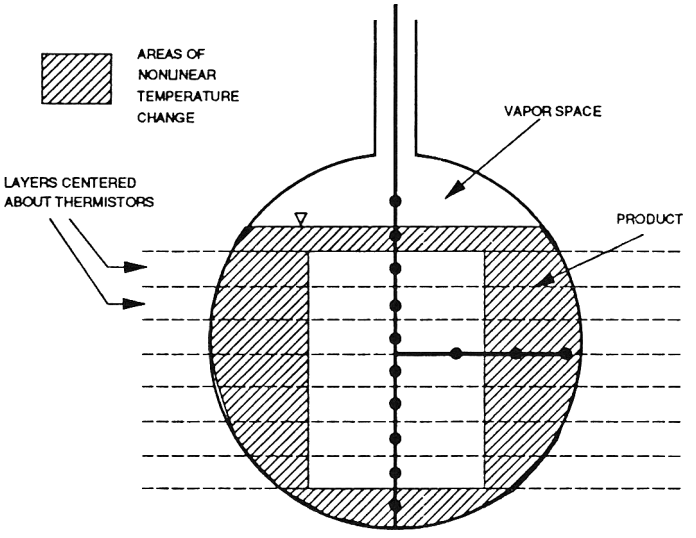

Fig. 1. Accurate temperature compensation requires that the average rate of change of temperature be measured in four regions of the tank.

region. The presence of groundwater at or above the bottom of the tank can complicate the product temperature field, because water has very different thermal diffusivity properties than the backfill and/or soil around the tank. Because of the curvature of the tank, the layers near the bottom are irregularly shaped, and it is difficult to estimate thermally induced volume changes with only one thermistor in the layer. In addition, the mixing that occurs when product is added to the tank in preparation for a test can significantly increase the rate of change of temperature in the bottom region. Large errors also occur in the layers near the surface of the product, especially because the temperature sensor in the uppermost layer is usually not centered in that layer. The greater the volume in the layer (whether at the top or bottom of the tank), the more significant the error will be. In general, the rate of change of temperature decreases over time as a state of thermal equilibrium develops between the product in the tank and the backfill and soil surrounding it. Thus, the accuracy of temperature compensation will improve as the number of temperature sensors increases (i.e., as the number of layers increase and the volume in each layer decreases) and as the waiting period between product addition and the start of the test increases. Increasing the waiting period is the only practical way to reduce the errors due to horizontal gradients. Any errors due to vertical gradients can be reduced by increasing the number of temperature sensors. Increasing the duration of the test and the precision of each temperature sensor reduces the error due to both types of gradients.

Experiments

The experiments were conducted in two nonleaking 190,000-L (50,000-gal) underground steel storage tanks containing JP-4 fuel. The tanks were located at Griffiss Air Force Base in upstate New York and were normally operational. Each tank was taken out of service for several days to support these experiments. Five days of experimental data were collected between 27 and 31 August 1990. The experiments conducted on 28 August had to be repeated because the data collected were lost due to a power outage caused by an electrical storm.

Configuration of the tanks and instrumentation

The two tanks used in these experiments are part of a large, hillside storage facility consisting of five clusters of four tanks. Each of the tanks is cut into the hill, buried under 76 to 91 cm (2.5 to 3 ft) of backfill, and covered by grass. The native soil is sandy and, because of the hillside location, groundwater does not reach the area where the tanks are situated. Fuel is delivered to the tanks by pipeline. A pump house services each cluster of tanks. For the purposes of these experiments, the two tanks were designated as Tank 1 and Tank 2. Figure 2 is a cross-section of the tanks; each tank is 320.0 cm (10.5 ft) in diameter and 23.62 m (77.5 ft) long and has a nominal capacity of 190,000 L

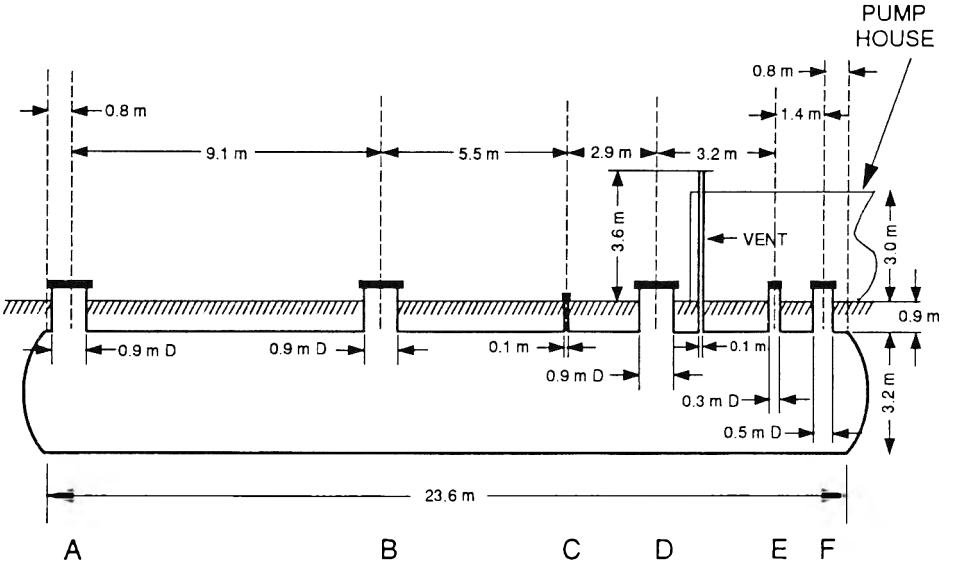

Fig. 2. Cross-section of the 190,000-L (50,000-gal) tanks used in the experiments. The thermistor arrays were located in Manway B and Vent C in Tank 1 and in Manways A and B in Tank 2. The level sensor was located in Manway B in both tanks.

(50,000 gal). Level measurements made in several of the openings of each tank suggest that the tanks are nearly horizontal, with a difference of only about 2.5 cm (1 in.) in height between the two ends.

The pump house, which overlaps the tanks by approximately 5.3 m (17.5 ft), is a single-story, flat-roofed building approximately 305 cm (10 ft) in height. By means of a pump, product can be transferred from one tank to another at a rate of up to 1,500 L/min (400 gal/min). The pump is located 76 cm (2.5 ft) from the end of the tank. Each tank has an overfill protection device that prevents its being filled above a height of 305 cm (10 ft), or beyond approximately 98% of its capacity.

In addition to the pump, there are six other openings into the tanks. There are three 76-cm (30-in.)-diameter manways, a 10-cm (4-in.)-diameter fill hole, and a 10-cm (4-in.)-diameter, 3.7-m (12-ft)-high vent located outside the pump house; a 25-cm (10-in.)-diameter level control port is located inside the pump house. The manways provide entry into the tanks. They are connected to the top of the tanks by flanges located 15 cm (6 in.) above the tanks. This connection is not liquid-tight and, as a consequence, the tanks could not be overfilled in these experiments. The first manway (A) is located 76 cm (2.5 ft) from the end of the tank, and the other two manways (B and D) are located 9.1 and 17.5 m (30.0 and 57.5 ft) away. A ladder is permanently installed in each manway.

Experiments in Tank 1 were conducted between 10:30 h on 27 August 1990 and 08:00 h on 30 August and those in Tank 2 between 10:15 h on 30 August and 14:50 h on 31 August. Thermistor arrays were inserted into Tank 1 at Manway B (Array A) and the vent hole at C (Array B) and into Tank 2 at Manways A (Array B) and B (Array A). The arrays were separated by 5.5 m (18 ft) in Tank 1 and by 9.1 m (30 ft) in Tank 2. The horizontal arms of the arrays, which extend from the center of the tank to the wall, were located on opposite sides of the tank in Tank 1 and on the same side of the tank in Tank 2. During the tests, the level and pressure sensor measurements in both tanks were made at Manway B. All of the level changes in the tanks were done by adding or removing product by means of the pump located 8.5 m (28 ft) away from the nearest thermistor array in Tank 1 and 14.0 m (46 ft) away from the nearest thermistor array in Tank 2; at these distances, it is not likely that the pump would have any affect on the temperature measurements. In both tanks, the inlet and outlet of the pump were located near the bottom. A 2,470-ml cylindrical bar used to experimentally determine the height-to-volume conversion factor was inserted into and removed from the liquid in the tank at Manway A in Tank 1 and Manway C in Tank 2; these openings were selected because they contained no temperature or level measurement equipment. All stick measurements were made in these same openings. The small-volume product additions, whose purpose was to simulate the effects of topping, were done at the opening where Array B was located. With the exception of a limited number of experiments conducted to measure surface fluctuations at 1 sample/s (1 Hz), all data were collected at a rate of 1 sample/min (0.017 Hz).

The analysis of the data assumes that the tanks are not leaking and that all valves isolating the piping from the tanks seal sufficiently so that no leakage of product back into the tank occurs during the test. Once every three years the tanks are emptied and visually inspected for leaks; the last inspection was done within 12 months of these tests and no leaks were found. Although a formal volumetric leak detection test was not done, the five days of data suggest that the tanks are tight, or at the very least, the tanks or piping are not leaking at any significant rate. The temperature-compensated volume rates that were estimated from 2.5 to 3 h of data beginning 21 and 17 h after the start of the overnight tests on 29 August and 30 August, respectively, were both less than 0.05 L/h (0.013 L/h) [9]. Furthermore, many of the observations and conclusions derived from these experiments are independent of whether or not the tank or piping is leaking. As part of the analysis, the possible effect of the pump house and the large manways on the tank temperature field (vapor and product) was recognized and investigated; these effects are described in this paper and in more detail in [9].

Temperature and level measurement systems

The following data were required for the experiments: (1) the change in the temperature of the product and (2) the height and change in level of the product. The product-temperature data were analyzed to estimate the thermally induced volume changes in the tank. The level-change data were converted to volume-change data using the experimental estimates of the height-to-volume conversion factor. The height data were used to estimate the volume of product in the tank during a test.

The data quality objective for the instrumentation was based upon the EPA performance standard for tank tightness tests [1] and is more fully described in [11]. All of the temperature and level measurement systems that were used in the experiments had sufficient precision to detect a leak of 0.38-ml/h (0.1-gal/h) with a P_D of 0.95 and a P_{FA} of 0.05 in a 2-h measurement period [12]. The sensors were calibrated according to the procedures described in [11], and all sensors used in the analysis were within specification.

Two types of product level measurements were required. The first was a measurement of the height of the product from the bottom of the tank; a pressure sensor with a precision of 0.5 cm (0.2 in.) or better was used for this. The second was a measurement of the level changes in the tank; an electromagnetic sensor developed by Vista Research prior to these experiments was used for this second measurement. The precision of this sensor was 0.00025 cm (0.0001 in.). The pressure and electromagnetic sensors were located at the bottom and top of Thermistor Array A, respectively. Each time the level was changed, it was also measured to the nearest 0.25 cm (0.125 in.) with a calibrated stick.

To measure product temperature, two arrays of thermistors were used. Figure 3 shows Arrays A and B and the channel number of the thermistors on each array. The thermistors, attached to a stainless steel tube, were spaced at

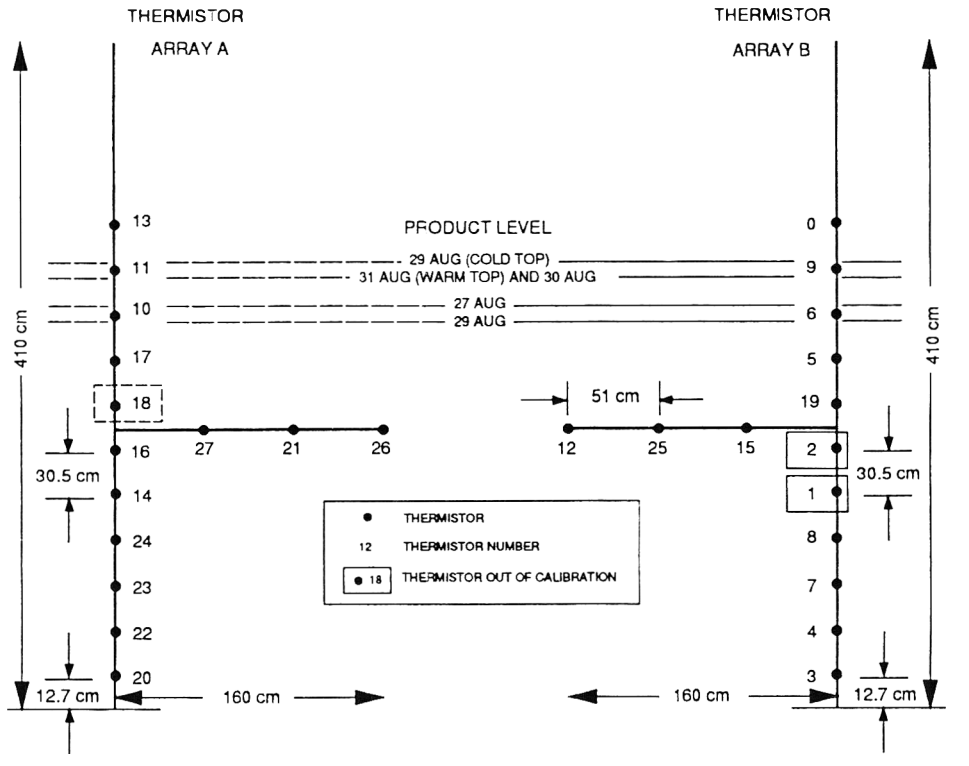

Fig. 3. Configuration of thermistor arrays A and B.

intervals of 31 cm (12 in.) along the vertical axis of the tank. The lowest thermistor was located approximately 13 cm (5 in.) from the bottom of the tank. The vertical portion of the array, containing a total of 11 thermistors, was used primarily to estimate the average thermally induced volume change of the product in the tank. To minimize any contamination of the product temperature measurements from changes in the temperature of the steel tube, each thermistor was inserted in a Teflon collar before being attached to the tube. Each array, placed in the tank through the fill hole or a manway, was equipped with a 1.5-m (5-ft)-long pivoting "arm" that could be lowered to a horizontal position after the array had been put in place. The pivoting arm provided for the measurement of horizontal thermal gradients between the tank's centerline and its walls. The arm contained three thermistors located at intervals of approximately 51 cm (20 in.); the thermistor located farthest from the centerline was within 7.6 cm (3 in.) of the tank wall. Each thermistor was accurate to within 0.64 cm (0.25 in.). Table 1 shows the nominal height of each thermistor from the bottom of the tank and shows the volume of product in the 31-cm (12-in.)-high layer centered about each thermistor. The thermistors had been calibrated in a well-mixed water bath to attain a precision of 0.001 °C or

better over a range of 0 to 30 °C. The accuracy of the thermistors was better than 0.02 °C.

Test conditions

Two "topping" tests and three "overnight" tests were conducted. The topping tests simulated the topping off of a tank prior to a test, whereas the overnight tests simulated the effects of a delivery or removal of product preparatory to a leak detection test. To simulate the effects of topping, 19 L (5 gal) of product that was either colder or hotter than the extant product was added to the tank. Figure 4 summarizes the nominal product level and the product additions and removals during the measurements. Also shown are the times of the overnight and topping tests and the height-to-volume calibrations. Table 2 gives more detailed information about the overnight tests.

During the first two overnight tests, initiated on 27 and 29 August in Tank 1, the levels were dropped by 29 and 39 cm, respectively, by removing 14,712 and 20,911 L (3,886 and 5,524 gal) of product from the tank, respectively. During the third test, the level in the tank was raised 70 cm by adding 44,054 L (11,637 gal)

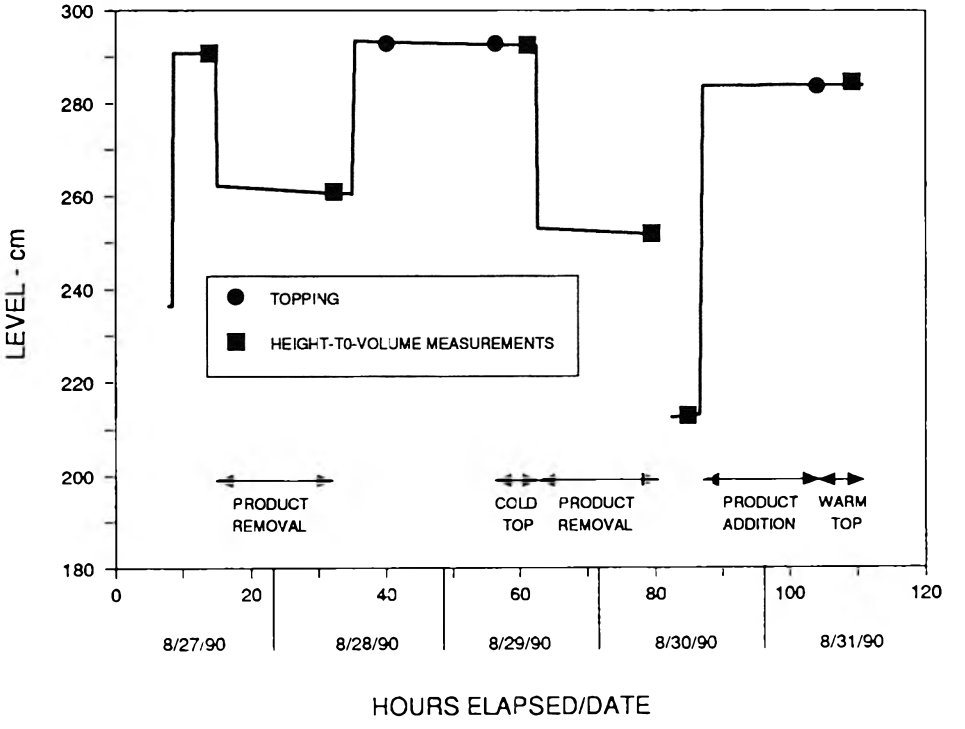

Fig. 4. Summary of the product level measurements between 27 and 31 August 1990 and of the analyses performed on the data.

TABLE 2

Height of thermistors closest to product surface

Tank	Start date	Start time	Nominal product level (cm (in.))	Thermistors closest to surface (Array A/B)	Nominal thermistor height from bottom (cm (in.))	Nominal product above thermistor (cm (in.))	Volume of product in upper layer[a] (L (gal))
1	Aug. 27	15:10	262.25 (103.25)	10/6	256.5 (101)	5.7 (2.25)	12,956 (3,422)
1	Aug. 29	14:41	253.0 (99.6)	17/5	226.0 (89)	26.9 (10.6)	28,346 (7,488)
1	Aug. 30	15:05	283.8 (111.75)	10/6	256.5 (101)	27.3 (10.75)	24,473 (6,465)

[a] Volume of product in the surface layer.

of product. All three overnight tests began late in the afternoon, between 14:30 h and 15:30 h, and ended between 07:00 h and 08:00 h the next morning. The nominal height of the product in the 3.2-m (10.5 ft)-diameter tanks and the number and location of the uppermost submerged thermistors are summarized in Table 2 and Fig. 3. The magnitude of the temperature effects induced by the removal or addition of product to the tank is discussed in the next section. The two topping tests, done on 29 August (with 19 L (5 gal) of product 8 °C colder than the product in the tank) and 31 August (with 19 L (5 gal) of product 5 °C warmer than the product in the tank) are described in [9].

Test results

Figure 5 shows, for each overnight test, profiles of the temperature field generated with the thermistor data from Array A. These profiles were generated 4 h after any addition or removal of product so that the strong temperature fluctuations associated with such volume additions or removals would have time to subside. All three profiles are similar and are consistent with summer ground conditions. There is a very strong gradient in the bottom 50 cm (20 in.) of the tank and another near the top of the tank. The strength of these gradients suggests that, especially during the summer, the thermistors must be more densely spaced than they were in these tests if the rate of change of temperature is to be accurately measured. During the winter, when the profile tends to be more uniform from the top to the bottom of the tank, less dense spacing would suffice.

The temperature-compensated volume time series for each overnight test was computed from the level and temperature data. First, the volume changes due to thermal expansion or contraction of the product were estimated from the temperature data, and the total volume changes were estimated from the level data. The two types of volume changes were then differenced to obtain the

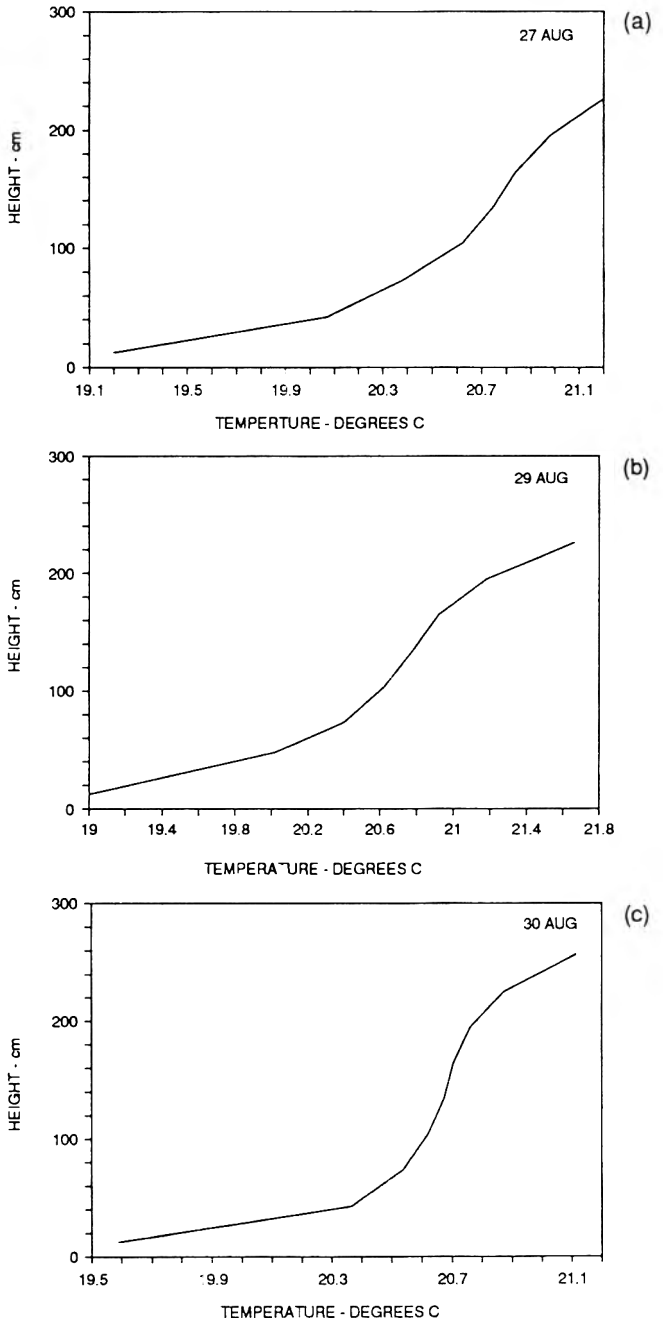

Fig. 5. Vertical temperature profile computed 4 h after the initial level change at (a) 15:10 on 27 August, (b) 14:41 on 29 August, and (c) 15:05 on 30 August.

temperature-compensated volume time series. The level data were converted to volume by means of an experimental estimate of the height-to-volume conversion factor. The thermally induced volume change, obtained from the temperature data from Array A, was computed from eq. (1). Samples of product were taken from the tank on 27 August 1990, and an estimate of the coefficient of thermal expansion was made from measurements of the API gravity and from the API tables. The coefficient of thermal expansion obtained, 0.000104/°C, was used in all volume calculations.

Figure 6 shows the time series of the thermally induced volume changes and the temperature-compensated volume changes. Only the volume changes that occurred immediately after the completion of the product transfer are shown. Figure 7 shows a portion of the temperature-compensated volume time series from Fig. 6 in greater detail. When product is removed from the bottom of the tank, as it was during the first two tests, the warmer product in the upper layers of the tank replaces the cooler product in the lower layers. The temperature of the product recorded at each layer showed a "step" increase that was associated with the removal. As shown in Fig. 6, once the product removal was completed, the temperature of the product began immediately to decrease in an attempt to come into equilibrium with the colder backfill and soil outside the tank. In the third overnight test, in which cold product was taken from the bottom of one tank and added to the other tank, a step increase in temperature was observed in the upper layers of the tank and a step decrease was observed in the lower layers. The step decrease in the upper layers occurred as the temperature of the colder product in the lower layers was raised; once the addition of product was completed, the temperature in these upper layers began to increase in an attempt to reach equilibrium with the temperature of the backfill and of the ground at that elevation. The step increase in the temperature at the bottom of the tank meant that the added product was warmer than the product and backfill/soil at the bottom of the tank. As shown in Fig. 6, a net increase in the temperature field was observed over time. The nature of these step changes in temperature is illustrated in Fig. 8 (for the bottom three thermistors in the 30 August overnight test) and Fig. 9 (for the thermistors on the horizontal arm located in the middle of the tank during the 29 August overnight test).

There is an initial "step" change in volume due to the addition or removal of product whose temperature differs from that of extant product, the backfill, and the soil beyond the backfill. This step change is not shown in Fig. 6. The thermally induced step change in the volume of product increased by 13.5 and 39.5 L (3.6 and 10.4 gal) in the first two tests, initiated on 27 and 29 August, respectively, and decreased by 93 L (24.6 gal) in the test initiated on 30 August. Calculation of the temperature difference between the added/removed product and the extant product is not straightforward, because the former was not of uniform temperature; in addition, the temperature of the product added to the tank on 30 August was not monitored. An estimate of the mean temperature of

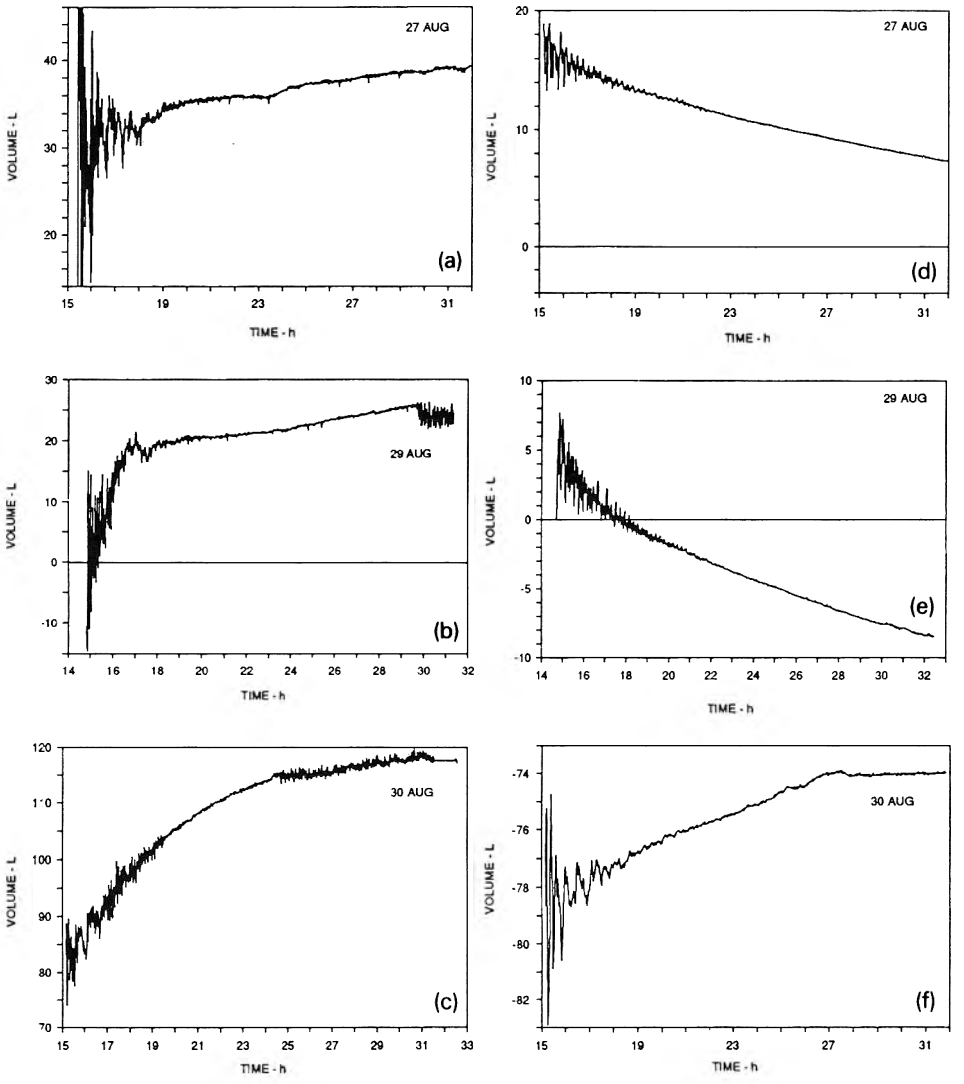

Fig. 6. Time series of the temperature-compensated volume changes (a–c) and the thermally induced volume changes measured by Array A (d–f) beginning *immediately after* the initial level change done at (a) 15:10 on 27 August, (b) 14:41 on 29 August, (c) 15:05 on 30 August, (d) 15:10 on 27 August, (e) 14:41 on 29 August, and (f) 15:05 on 30 August.

the added/removed product is necessary to effect the measured volume change. This estimate was made from

$$\Delta v = C_e(\langle T_2 \rangle - \langle T_1 \rangle) V_1 - C_e(\langle T_2 \rangle - \langle T_a \rangle) V_a \tag{2}$$

and

$$\langle T_j \rangle = \Sigma(\Delta v_i / V_j)(T_j) \tag{3}$$

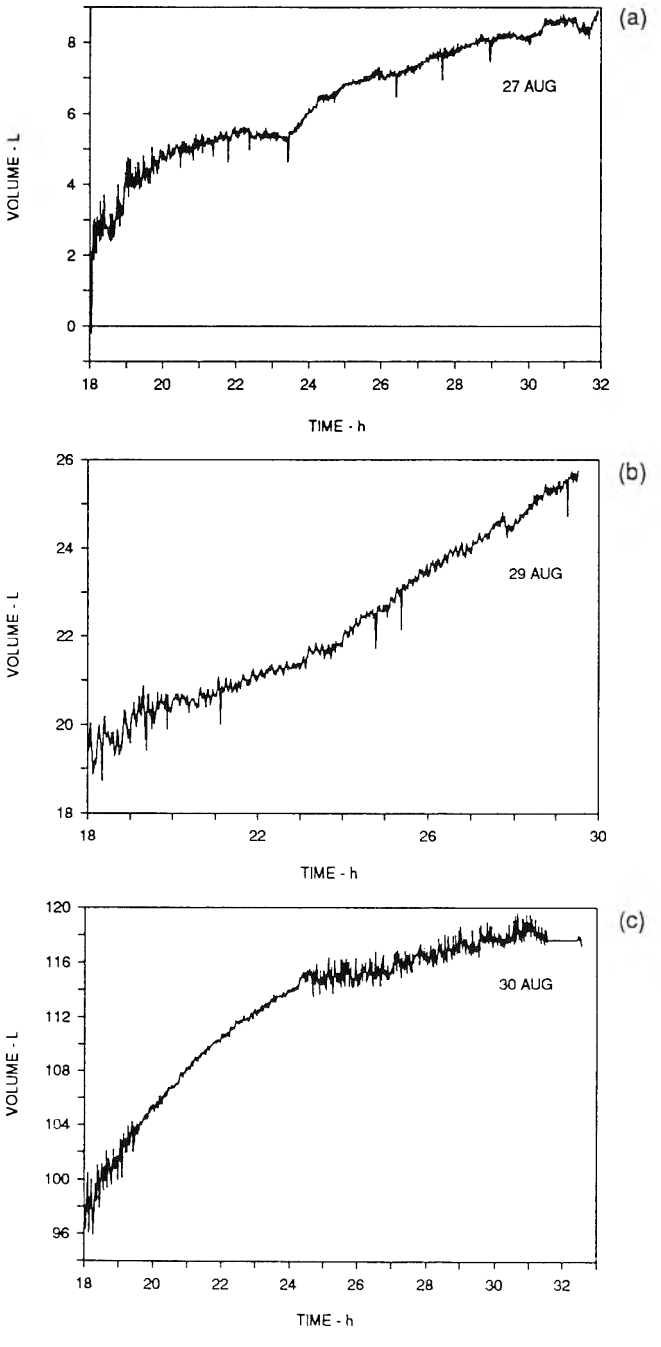

Fig. 7. Time series of the temperature-compensated volume changes estimated from Array A beginning approximately 3 h after the initial level change done at (a) 15:10 on 27 August, (b) 14:41 on 29 August, and (c) 15:05 on 30 August.

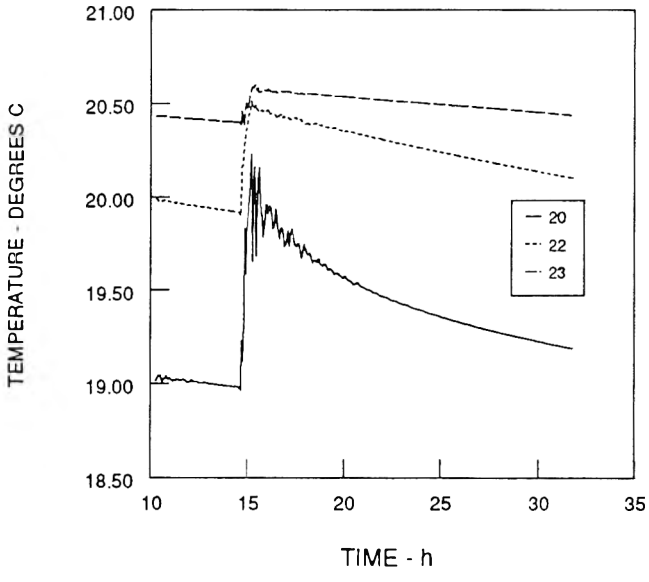

Fig. 8. Time series of the product temperature changes for the bottom three thermistors on Array A collected after the addition of product at 15:05 on 30 August.

where $\langle T_{j=2} \rangle$ is the volumetrically weighted mean temperature of the product in the tank immediately *after* the addition or removal of product; $\langle T_{j=1} \rangle$ is the volumetrically weighted mean temperature of the product in the tank immediately *before* the addition or removal of product; $\langle T_a \rangle$ is the mean temperature of the product added or removed, and necessary to effect the measured "step" volume change; Δv is the volume of product in the tank; V_1 is the volume of product in the tank immediately *before* addition/removal; V_2 is the volume of product in the tank immediately *after* addition/removal; and V_a is the volume added or removed. For each of the three overnight tests, an estimate of $\langle T_a \rangle$ was made by solving eq. (2) for $\langle T_a \rangle$, given the measured Δv and estimates of $\langle T_1 \rangle$ and $\langle T_2 \rangle$ made graphically from the time series generated for each thermistor (cf. Vol. II of [9]). The results are shown in Table 3. The mean difference in temperature between the extant product and the added/removed product was 1.6, 0.6, and $-3.9\,^{\circ}C$, respectively, in each of the three overnight tests.

Estimates of the thermally induced volume changes were made with five thermistors spaced at 61-cm (24-in.) intervals as well as with ten thermistors. Direct comparison of the temperature-compensated time series made with five and ten thermistors showed significant differences. The analysis suggests that five thermistors do not provide adequate coverage for accurate temperature compensation.

Several observations can be made about the temperature-compensated volume time series shown in Fig. 6.

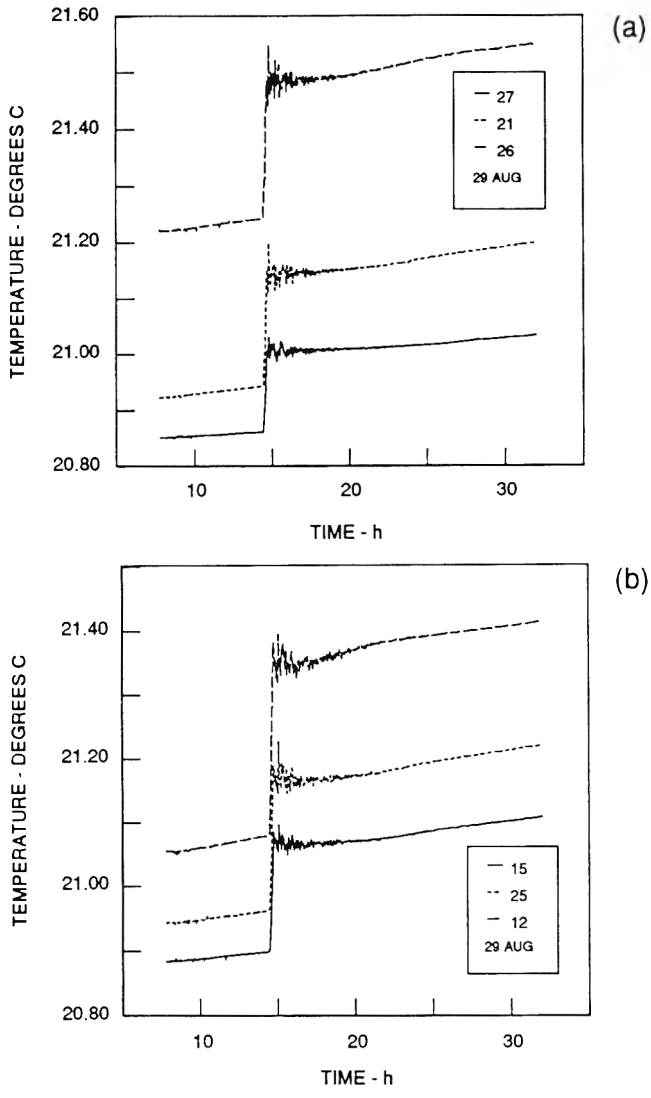

Fig. 9. Time series of the product temperature changes on the horizontal arm extending from the center of the tank (a) on Array A and (b) on Array B. The arm, located at a height of approximately 180 cm (71 in.) from the bottom of the tank, is located at the midpoint between Thermistors 16 and 18 on Array B and Thermistors 2 and 10 on Array A.

- Large volume fluctuations, which are tens of liters in magnitude, are present during the first 4 h or more of *each* overnight test.
- During the first 5 to 10 h after the addition or removal of product, an exponential increase in the temperature-compensated volume time series is observed. This behavior is especially definitive in the 30 August data.

TABLE 3

Estimate of the difference in temperature between the product added to or removed from the tank in each overnight test

Parameter	Dimension	August 27	August 29	August 30
Δv	L	13.5	39.5	93.0
V_1	L	47,911	48,092	134,735
V_a	L	14,712	20,911	44,054
$\langle T_1 \rangle$	°C	20.57	20.48	21.08
$\langle T_2 \rangle$	°C	20.76	20.73	20.63
$\langle T_a \rangle$	°C	22.20	21.09	17.23
$\langle T_a \rangle - \langle T_1 \rangle$	°C	1.63	0.61	−3.85

- A distinct change in the temperature-compensated volume time series is observed at approximately 24 h in all three overnight tests; this change in volume rate is especially evident in the 29 August test.
- Estimates of the temperature-compensated volume rate made 10 h after product has been added to or removed from the tank (Table 4) suggest that product is flowing into the tank. This is indicated by the size of the residual volume changes, which still persist after the exponential changes have subsided. Assuming that the inflow is not caused by an inadequately sealed valve, it would seem that the thermally induced volume changes have not been adequately compensated for, that the deformation of the tank has not subsided, and/or that condensation is occurring. Even if the tank did have a hole or fissure, no inflow of groundwater could occur because the water table is located below the level of the tank.
- The fluctuations in the temperature-compensated volume time series have periods of 2 to 4 h. These fluctuations are best observed in Fig. 7. Short leak detection tests, 1 to 2h in duration, would be adversely affected by these fluctuations, because they do not accurately represent the long-term trend.

After an extensive analysis, which is more fully described in [9], it was concluded that each of the five observations noted above can be explained by changes in the temperature of the product stored in the tank that have not been adequately measured. A discussion of each observation is provided below.

Large temperature fluctuations after product addition or removal

The large volume fluctuations observed in the calculated temperature-compensated volume time series are produced by the addition or removal of product. Any additions or removals will alter the temperature field. The horizontal and vertical mixing of the product creates large temperature fluctuations that last for many hours. During this period, an accurate leak detection test can not be conducted. It is significant that while the level of the temperature fluctuations observed in these tests is greater than those observed in

TABLE 4

Summary of results of overnight tests

Tank	Start date	Start time (h)	Nominal level (cm (in.))	TCVR[a] (L/h (gal/h))
1	Aug. 27	24–29	262.3 (103.25)	0.36 (0.094)
1	Aug. 29	24–29	252.1 (99.25)	0.66 (0.172)
2	Aug. 30	25.5–29.5	283.8 (111.75)	0.22 (0.057)

[a] TCVR is the abbreviation for temperature-compensated volume rate.

tests conducted on the 30,000-L (8,000-gal) tanks at the Test Apparatus [5, 8, 12], the duration is almost identical. The data suggest that it takes at least 4 h for the temperature fluctuations to subside.

Thermally induced exponential volume changes

The initial inspection of the temperature-compensated volume time series suggested that the exponential changes in volume were due to deformation induced by an abrupt change in the level of the product. While this could explain the volume changes during the first 4 to 6 h of the 27 and 29 August tests, the sense of the change is incorrect in the 30 August test. If deformation had been a dominant noise source in the 30 August test, the temperature-compensated volume time series would have decreased over time.

A more comprehensive analysis of the temperature data immediately after product addition to or removal from the tank showed that the exponential increase in the temperature-compensated volume time series seen in all three tests can be explained by inadequate estimation of the thermally induced volume changes in the bottom layer. Figure 8 displays the temperature time series for the bottom three thermistors on Array A recorded during the 30 August test. The rate of change of temperature measured by the bottom thermistor (No. 20) is exponential and significantly greater than that measured by the thermistor located immediately above it. As illustrated by the profiles in Fig. 5 and the shape of the bottom layer (see Fig. 1), this is a region where the temperature gradient is very strong and the volume of product surrounding the thermistor is large and asymmetrical. Simply locating the thermistor a few centimeters higher could result in a significantly lower rate of change of temperature, which would explain the exponential increase in volume. Additional thermistors, spaced at intervals of 15 cm (6 in.) or less, would be required for an accurate estimate of the mean rate of change of temperature-volume in this region of the tank. About 27 h after the product transfer, the rate of change measured by the bottom two thermistors is approximately the same, suggesting that this source of error has decreased sufficiently that an accurate leak detection test can be conducted.

The temperature fluctuations recorded by the bottom thermistor (No. 20) and observed during the first two hours after the product addition are large enough to explain most of the thermally induced volume changes in Fig. 6(f). These volume changes are probably produced by internal waves that developed on the steep temperature gradient located near the bottom of the tank during the product addition.

Distinct change in the temperature-compensated volume rate

In Fig. 7, a distinct change in the temperature-compensated volume rate was observed during the 29 August test between 19.0 and 23.5 h and 23.5 and 31 h. The rate increased from 0.38 L/h (0.099 gal/h) to 0.70 L/h (0.18 gal/h). We believe that this increase in rate is due to the presence of horizontal gradients in the rate of change of temperature between the centerline and the walls of the tank. This mechanism is illustrated in Fig. 9, which displays the time series of the thermistors located on the horizontal arms of Arrays A and B. A distinct shift in the rate of change of temperature is observed at 23.5 h; this coincides with the distinct change in the temperature-compensated volume time series. The difference in the rate of change of temperature observed before and after 23.5 h for the middle thermistors (Thermistors 21 and 25) on each horizontal arm is approximately 0.00175 °C/h. Assuming that this 0.00175 °C/h increase in rate affects 113,500 L (30,000 gal) of product, this would account for 0.21 L/h (0.055 gal/h) of the 0.32-L/h (0.085-gal/h) increase.

Uncompensated thermally induced volume changes

An attempt was made to explain and quantify the residual volume changes presented in Table 4. An analysis of each test is presented in [9]. This paper includes a brief discussion of the residual changes observed in the 29 August test. A portion of the error can be accounted for by the difference in the rate of change of temperature between the centerline and the walls of the tank. The temperature change measured at Thermistors 26 and 21 on Array A was 0.004 °C/h, while at Thermistor 27, located closest to the middle of the tank, it was 0.0022 °C/h. Similar differences were observed on Array B. Assuming that this 0.0018 °C/h increase in rate affects 113,500 L (30,000 gal) of product, this would account for 0.21 L/h (0.056 gal/h) of the error. Another portion of the error can probably be accounted for by the rate of increase in temperature near the surface of the product, which is not accurately represented by Thermistor 17, located 25 cm (10 in.) below the surface. An analysis of the 27 August data, in which the upper thermistor (No. 10) was only 5.7 cm (2.25 in.) below the surface, showed a difference of 0.02 °C/h in the rate of change of temperature measured by this thermistor and the one located 31 cm (12 in.) below it. This suggests that additional thermistors are required in this region if the estimate of the volume changes in this layer is to be accurate. Assuming the same rate of change of temperature in the upper 11.5 cm (4.5 in.) of the product (7,258 L (1,915 gal)) that was observed in the 27 August overnight test, this rate of change of 0.02 °C/h would account for 0.15 L/h (0.039 gal/h) of the error. These

estimates of the measurement errors in the surface region and in the region between the centerline and wall of the tank account for only about half of the total residual volume change. However, they could easily be off by a factor of two. This factor-of-two uncertainty is derived from the lack of temperature measurements in these regions of the tank.

The additional residual volume changes could also be explained by condensation and by horizontal gradients in the rate of change of temperature along the long axis of the tank. An estimate of the condensation could not be made, but the temperature conditions measured at the vapor/liquid/wall interface are consistent with those that would produce condensation. Errors due to the horizontal gradient in the rate of change of temperature along the long axis of the tank were also examined. The temperatures measured by each thermistor on Array B were differenced with those measured by the thermistors on Array A that were located at the same height. The largest differences in temperature were generally less than $\pm 0.001\,^{\circ}C/h$, 4 h or more after product additions or removals and were randomly distributed in the vertical. Thus, the sum of all temperature differences along the vertical axis was less than $0.001\,^{\circ}C/h$, which corresponds to an error of less than 0.19 L/h (0.05 gal/h) in a 190,000-L (50,000-gal) tank filled with product.

An analysis of the temperature-compensated volume data approximately 20 h after the product removal on 29 August and the product addition on 31 August showed that the residual volume changes had decreased to 0.036 and -0.043 L/h (0.009 and -0.011 gal/h), respectively. An analysis of the temperature data obtained on the horizontal arms of Arrays A and B showed that the gradient in the rate of change of temperature had completely dissipated by that time, suggesting that this gradient was the dominant error.

Instrumentation and ambient fluctuations

The minimum duration of a test depends on the magnitude and period of the instrumentation and ambient noise fluctuations. A leak detection test must be long enough that the trend in the temperature-compensated volume rate can be accurately estimated. The data in Fig. 7 suggest that a 4-h test would yield a good estimate of the trend. Previous calculations indicated that to meet the data quality objectives with the precision of the level and temperature sensors used in these experiments a test had to be at least 2 h long [12]. Thus, the ambient fluctuations would be the controlling factor in determining the appropriate duration of a leak detection test performed with these sensors. A 1-h test, typical of many tightness tests used on small tanks, would simply track the ambient volume fluctuations and would not yield a good estimate of the trend. A detailed discussion of how to estimate the minimum duration of a test based on the precision of the level and temperature sensors is presented in [11, 12]. When the instrumentation is less precise, the test duration must be commensurately longer. For example, if the level sensor had a precision of 0.0025 cm (0.001 in.), the test would have to be at least 4 h long.

Conclusions and recommendations

This study showed that the procedures currently used to compensate for temperature when testing 30,000- and 38,000-L (8,000- and 10,000-gal) tanks will not suffice when the tanks are as large as 190,000-L (50,000-gal). The most important cause of errors in testing large tanks with volumetric leak detection systems, which consist of a level or volume measurement system and a vertical array of temperature sensors, appears to be inaccurate temperature compensation. Five things are necessary for successful temperature compensation. First, a test must not be started until the horizontal gradients in the rate of change of temperature between the centerline and the tank walls have dissipated. Second, the number of temperature sensors must be sufficient that the volume of product in the layer around each sensor is not too great; the smaller the volume in each layer, the less likely it is that a temperature measurement error, when summed with measurements from the other layers, will adversely affect the test. Third, the duration of the test must be long enough that (1) the fluctuations observed in the temperature-compensated volume 4 to 6 h or more after any product additions or removals can be averaged and (2) the precision of the temperature and level instrumentation is sufficient to detect a leak with a specified performance. Fourth, a test should not begin unless the average rate of change of temperature in the tank as a whole or in any one of the layers is small enough to allow accurate temperature compensation. Fifth, an accurate experimental estimate of the constants necessary for converting level and temperature changes to volume is required: these constants include the coefficient of thermal expansion, the height-to-volume conversion factor, and the volume of product in each layer of the tank.

Horizontal gradients in the rate of change of temperature between the centerline and the walls appear to be the controlling source of error in temperature compensation. A waiting period of at least 24 h is recommended so that these gradients have time to subside. If the initial temperature difference between the *in situ* product and that added or removed is greater than it was in the tests conducted as part of this study, a longer waiting period might be required. More data are required before the adequacy of a 24-h waiting period in such cases can be verified. The 24-h waiting period appears to be more than adequate for structural deformation of the tank to subside and for the violent temperature fluctuations that occur immediately after any transfer of product to or from the tank to dissipate. Unless the temperature is sampled with a horizontal array of temperature sensors similar to the one used in these experiments, however, it will not be possible to assess whether even a 24-h wait is long enough. There are alternatives to direct measurement of the horizontal gradient. One is to conduct additional tests to determine if the rate of change of volume is approaching a constant value, and the other is not to begin a test until the thermal volume change in the tank as a whole, or in a single representative layer, is small enough that it cannot adversely affect the results of a test.

A total of at least 10 temperature sensors spaced vertically at 31-cm (12-in.) intervals or less is recommended; this recommendation assumes that the waiting period is at least 24 h. If more than 10 temperature sensors are available, these additional temperature sensors should be more closely spaced at the bottom of the tank and near the product surface, because in these two regions the rate of change of temperature and the vertical gradient in the rate of change of temperature are generally greater than they are elsewhere in the vertical. During the 24-h waiting period, the 31-cm (12.-in.) spacing used in these experiments was insufficient at times to accurately measure the rate of change of temperature near the bottom of the tank and near the surface of the product. If a waiting period shorter than 24 h is used, which may be possible, for example, if horizontal measurements of temperature are made as part of the test procedure, then a spacing of 15 cm (6 in.) or less is suggested.

The data collected in these experiments suggest that the minimum duration of a leak detection test should be at least 4 h so that the ambient volume fluctuations that occur in the tank can be averaged. The actual duration of a test might be longer if the precision of the instrumentation is less than it was in this study. In these experiments, however, the precision of the temperature and level sensors was sufficient to support a shorter test.

Ultimately, the performance achieved with a leak detection system is controlled by the precision of the instrumentation and the accuracy of estimating the constants. The best way to minimize the effect of instrumentation errors is to wait until the rate of change of temperature in the tank or in a layer is small. An uncertainty of 0.001 °C/h in the measurement of the average rate of change of temperature, which is typical of the types of uncertainties achieved during most leak detection tests, results in an error of 197 ml/h (0.052 gal/h) in a 190,000-L (50,000-gal) tank containing JP-4 fuel. This is large enough to exceed most detection thresholds used to conduct a tank tightness test. Assuming that 95% of the temperature changes can be compensated for, this means that a test should not be started until the rate of change of temperature in the tank is less than 0.02 °C/h, which is typical of the type of changes observed in tanks. An uncertainty of 5% in either the coefficient of thermal expansion or the volume of the product in the tank would result in a bias of 197 ml/h (0.052 gal/h). Clearly, temperature compensation that is sufficiently precise to meet the tank tightness regulatory standards (i.e., to detect a leak of 0.1 gal/h with a P_D of 95% and a P_{FA} of 5%) is difficult to achieve.

The following procedure is recommended for compensating for the thermal expansion or contraction of the product.

- Place the top and bottom temperature sensors approximately 8 cm (3 in.) from the product surface and from the bottom of the tank, respectively.
- Space the temperature sensors at intervals of 15 to 31 cm (6 to 12 in.) or less along the vertical axis of the tank; space the sensors at intervals of 15 cm (6 in.) or less in the bottom 46 cm (18 in.) of the tank and in the 15 to 31 cm (6 to 12 in.) of product located immediately beneath the surface. (A 31-cm

(12-in.) spacing can be used if the rate of change of temperature between adjacent layers of product throughout the entire tank is nearly identical.)

- Partition the tank into layers, each of which is centered about a temperature sensor. Then calculate the volume of product in each layer.
- Wait at least 24 h for horizontal gradients in the rate of change of temperature to dissipate. (These horizontal gradients occur between the centerline and the wall of the tank.) Alternatively, measure these horizontal gradients directly, and do not attempt to compensate for temperature until they have dissipated. If the compensated volume rate exceeds the threshold, continue to test until the measured volume rate ceases to decrease and remains constant.
- Using real-time measurements, wait for the rate of change of temperature to diminish sufficiently that the maximum potential error in measuring the average rate of temperature for each test is known. The acceptable rate of temperature change depends on the number of thermistors, the precision of each thermistor, and the degree of compensation that can be achieved with the array of thermistors. A very conservative approach is to incorporate the following analysis tests.
  (i) Do not begin a test if the rate of change of temperature is great enough in any one layer to produce a volume change that will exceed the detection threshold. (When using a threshold of 0.05 gal/h in a tank containing JP-4 fuel, this would limit the rate of change of temperature to less than 0.008 °C in the largest layers of a 10.5-ft-diameter, 190,000-L (50,000-gal) tank divided into 10 layers.)
  (ii) Do not begin a test if the average rate of change of temperature throughout the tank is great enough to produce volume changes that exceed the threshold based on an average level of compensation to be achieved. (When using a threshold of 0.05 gal/h in a tank containing JP-4 fuel, this would limit the rate of change in temperature to less than 0.019 °C throughout a 10.5-ft-diameter, 190,000-L (50,000-gal) tank if on average the method is able to compensate for 95% of the temperature changes.)
- Use the most precise temperature and level measurement systems available and calibrate them frequently and properly. It is recommended that temperature sensors have a precision of 0.001 °C and level sensors a precision of 0.00025 cm (0.0001 in.). The trade-offs in instrumentation precision and test duration are described in [12].
- Check that all sensors function properly during a test. If a sensor malfunctions, the test should be repeated.
- Make sure the test is at least 4 h long so that ambient fluctuations will be properly averaged and will not affect the test. Longer tests may be required depending on the resolution and precision of the level and temperature sensors.
- Measure the coefficient of thermal expansion *experimentally*.

- Determine the height-to-volume conversion factor used to convert level measurements to volume measurements *experimentally*.

It must be emphasized that the conclusions and recommendations drawn from these experiments are based upon a very limited set of data. These recommendations, however, are based on the well-known and well-understood basic features of a volumetric test developed for smaller tanks (30,000 to 38,000 L (8,000 to 10,000 gal)); these are features that have been shown to be necessary for high performance through tens of evaluations of systems offered commercially and through many controlled experiments in underground test tanks. Whether the temperature-compensation procedure recommended for volumetric tests *conducted on 190,000-L (50,000-gal) tanks* is sufficient to meet the EPA's regulatory standard for a tank tightness test (or a monthly monitoring test) will not be known until a number of actual performance evaluations have been conducted on one or more systems that incorporate some or all of these procedures. Despite the fact that there were not enough data in this study to fully evaluate the effect of longer waiting periods, it is our opinion that a waiting period of at least 24 h is the key to high performance.

Acknowledgements

We gratefully acknowledge the coordination and operational assistance provided by the civilian and military staff at Griffiss Air Force Base, who provided the tanks for these experiments, and the New York State Department of Environmental Conservation. This work was funded by the U.S. Environmental Protection Agency.

References

1 U.S. Environmental Protection Agency, Underground Storage Tanks; Technical Requirements and State Program Approval; Final Rules, Federal Register, 40 CFR Parts 280 and 281, v53, n185 (1988).

2 J.W. Maresca, Jr., N.L. Chang, Jr. and P.J. Gleckler, A Leak Detection Performance Evaluation of Automatic Tank Gauging Systems and Product Line Leak Detectors at Retail Stations, Final Report, American Petroleum Institute, Vista Research Project 2022, Vista Research, Inc., Mountain View, CA, 1988.

3 J.W. Maresca, Jr., R.D. Roach, J.W. Starr and J.S. Farlow, U.S. EPA evaluation of volumetric UST leak detection methods, In: Proc. 13th Annu. Res. Symp., Hazardous Waste Engineering Research Laboratory, Office of Research and Development, U.S. Environmental Protection Agency, Cincinnati, OH, 1987.

4 R.D. Roach, J.W. Starr, C.P. Wilson, D. Naar, J.W. Maresca, Jr. and J.S. Farlow, Discovery of a new source of error in tightness tests on an overfilled tank, In: Proc. 14th Annu. Res. Symp., Risk Reduction Engineering Laboratory, Office of Research and Development, U.S. Environmental Protection Agency, Cincinnati, OH, 1988.

5 U.S. Environmental Protection Agency, Evaluation of Volumetric Leak Detection Methods for Underground Fuel Storage Tanks, Vol. I (EPA/600/2-88/068a) and Vol. II (EPA/600/2-88/068b), Risk Reduction Engineering Laboratory, U.S. Environmental Protection Agency, Cincinnati, OH, 1988.
6 J.W. Maresca, Jr., J.W. Starr, R.D. Roach and J.S. Farlow, Evaluation of the Accuracy of Volumetric Leak Detection Methods for Underground Storage Tanks Containing Gasoline, Proc. of the 1989 Oil Spill Conf., U.S. Coast Guard, American Petroleum Institute, and the U.S. Environmental Protection Agency, San Antonio, TX, 1989.
7 J.W. Maresca, Jr., J.W. Starr, R.D. Roach, J.S. Farlow and R.W. Hillger, Summary of the results of EPA's evaluation of volumetric leak detection methods, In: Proc. 15th Annu. Res. Symp., Risk Reduction Engineering Laboratory, Office of Research and Development, U.S. Environmental Protection Agency, Cincinnati, OH, 1990.
8 J.W. Maresca, Jr., J.W. Starr, R.D. Roach, D. Naar, R. Smedfjeld, J.S. Farlow and R.W. Hillger, Evaluation of volumetric leak detection methods used in underground storage tanks, J. Hazardous Mater. 26 (1991) 261–300.
9 U.S. Environmental Protection Agency, Volumetric Leak Detection in Large Underground Storage Tanks, Vol. I (EPA/600/2-91/044a) and Vol. II (EPA/600/2-91/044b), Risk Reduction Engineering Laboratory, U.S. Environmental Protection Agency, Cincinnati, OH, 1991.
10 U.S. National Bureau of Standards, Volume Correction Factors, In: Manual of Petroleum Measurement Standards. American Petroleum Institute, Washington, DC, 1980.
11 J.W. Starr and J.W. Maresca, Jr., Quality Assurance Project Plan: Evaluation of Leak Detection Methods for Large Underground Storage Tanks, Vista Research Project 1026, Vista Research, Inc., Mountain View, CA, 1990.
12 J.W. Maresca, Jr., J.W. Starr, R.F. Wise, R.W. Hillger and A.N. Tafuri, Evaluation of internal leak detection technology for large underground storage tanks, In: Proc. 16th Annu. Res. Symp., Risk Reduction Engineering Laboratory, U.S. Environmental Protection Agency, Cincinnati, OH, 1990.

Journal of Hazardous Materials, 38 (1993) 363–384
Elsevier Science Publishers B.V., Amsterdam

Future risk from a hypothesized RCRA site disposing of carcinogenic metals should a loss of societal memory occur

David Okrent* and Leiming Xing

Department of Mechanical, Aerospace and Nuclear Engineering, 48-121 Engineering IV, University of California at Los Angeles, Los Angeles, CA 90024 (USA)

(Received September 21, 1992; accepted in revised form December 14, 1992)

Abstract

The future risk of a hypothesized Resource Conservation and Recovery Act (RCRA) site disposing of carcinogenic metals, arsenic, chromium, nickel, cadmium, and beryllium in the U.S. is assessed. Societal memory is assumed to be lost regarding the site. A human intrusion scenario on the site and a residential scenario one kilometer down-gradient of the groundwater flow direction from the site are assumed, starting at 1000 years after the site's closure. For the human intrusion scenario, the exposure pathways considered are fruit and vegetable intake, soil ingestion, and dermal contact with soil. The quantitative results obtained for the three pathways are as follows: lifetime excess cancer risk due to fruit and vegetable intake is 0.18; risk due to dermal contact with the soil is 0.12; and risk due to soil ingestion is 2.6×10^{-3}. For the residential scenario, only qualitative discussion of exposure via groundwater is presented due to the large uncertainties. The U.S. EPA (Environmental Protection Agency) attention to and requirements concerning long-term risk from RCRA sites containing metal carcinogens, which never change due to radioactive decay, stand in sharp contrast to the stringent requirements over 10,000 years posed by EPA for geologic disposal of high level radioactive wastes, and the long-term requirements posed by the U.S. Nuclear Regulatory Commission for low level radioactive waste disposal sites.

1. Introduction

Toxic metals are usually considered persistent in the environment in that, unlike radioactive isotopes, metals do not decay in the environment. This raises a serious concern about whether and how we can dispose of the wastes containing such toxic metals, given that society chooses to use them. As is well known, in 40 CFR 191 (remanded), EPA poses stringent requirements, including loss of societal memory, over 10,000 years for geologic disposal of high level radioactive wastes, despite the presence of markers at the site [1]. Also, the

*To whom correspondence should be addressed.

0304-3894/93/$06.00

U.S. Nuclear Regulatory Commission (USNRC) requires long-term risk assessment for low level radioactive waste disposal sites [2]. This paper is to address the disparity between the EPA regulation regarding carcinogenic metals and the requirements posed on high level radioactive wastes.

Five metals with potential carcinogenicity are the focus of this paper. These are arsenic, cadmium, chromium, nickel, and beryllium. The future risks of a hypothesized Resource Conservation and Recovery Act (RCRA) site which disposed of these metals are assessed herein using similar scenarios and assumptions to those of a high level or a low level radioactive waste disposal site risk assessment [2]. Among the important assumptions, societal memory is assumed lost regarding the hypothesized RCRA site; human intrusion may occur at the site; and there may be a residential scenario down-gradient of the groundwater flow direction.

Section 2 is a description of the hypothesized RCRA site. Section 3 is a review of toxicity and current usage of five carcinogenic metals. Section 4 discusses the waste treatment and treatment standards imposed by EPA. Section 5 hypothesizes a RCRA site inventory that meets the current EPA requirements. Section 6 assumes scenarios for the future risk analysis; these include the human intrusion scenario and residential scenario. Section 7 discusses models of several exposure pathways as well as presents qualitative discussion on groundwater contamination. Section 8 presents results for the human intrusion scenario. Section 9 is a discussion concerning the implications of this analysis.

2. Site description

Figure 1 shows a hypothesized RCRA site. This site is assumed to be used to dispose of wastes containing several carcinogenic metals and their compounds. These wastes need to be treated before being disposed of. After treatment, different kinds of containment, such as Above Grade Mound, Above Grade Vault and Above Grade Building as well as Below Grade Landfill [3], can be used to hold the wastes. The difference between above grade and below grade containment is that the below grade containment holds the wastes below the ground surface. In this analysis, it is assumed that the RCRA site uses a Below Grade Landfill with double liners and leachate collection system. The basic design features of the hypothesized site are similar to those of the waste sites reported by the Minnesota Waste Management Board [3]. As shown in Fig. 1, the lower most layer is recompacted clay with at least three feet thickness. This layer of clay has low permeability. On top of the clay is a secondary flexible membrane liner which is at least 30 mils (0.03 inch) thick [3]. Above the liner is the secondary leachate collection system which is able to drain off fluid which would reach the liner. Above the secondary leachate collection system is the primary flexible membrane liner. It is also required to be at least 30 mils thick. On the top of this liner lies the primary leachate collection system. The

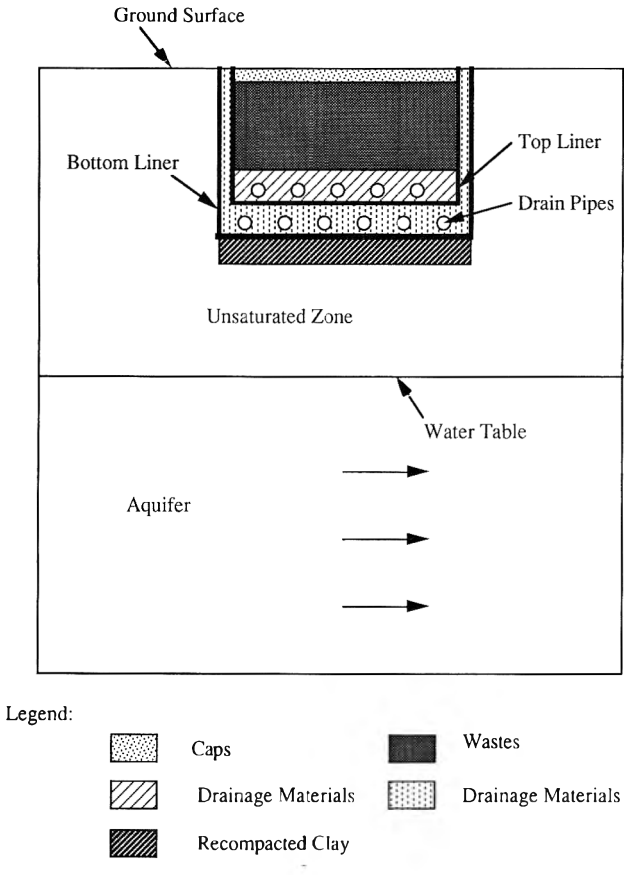

Fig. 1. A hypothesized RCRA site.

primary leachate collection system is covered by a permeable membrane over which the waste is placed. Above the wastes, there are vegetative caps. The caps might consist of three layers, as used in a low level radioactive waste site [2]. The bottom layer is a low-permeability clay, the middle layer a silt loam, and the top layer is the original undisturbed soil. The total thickness of these layers might be 2 m.

About the location of the hypothesized site, the EPA requirement is the following according to Wagner [4]: "Currently, the only location restrictions are: The facility must be at least 200 feet from an active (during the last 10,000 years) Holocene fault; Facilities in a 100-year flood plain must be designed to prevent washout from 100-year floods."

"More stringent location standards, as mandated by HSWA (Hazardous and Solid Waste Amendments), were expected to be issued in 1992. The purpose of these standards will be to create national requirements for the location of the

TABLE 1

Parameters for the hypothesized site (adapted from Table 4–1 of Ref. [2])

Parameter	Value
Average annual infiltration	25 cm/y
Thickness of unsaturated zone	24 m
Saturated hydraulic conductivity of unsaturated zone	115.3 m/y
Porosity of unsaturated zone	0.52
Thickness of aquifer	25 m
Hydraulic conductivity of aquifer	115.3 m/y
Hydraulic gradient of aquifer	0.02
Porosity of aquifer	0.52
Average pore velocity of aquifer	4.44 m/y
Longitudinal dispersivity of aquifer	2 m
Transverse dispersivity of aquifer	0.2 m

hazardous waste management facilities. These requirements will contain restrictions based on proximity to populations, vulnerable hydrogeology, seismic zones, 100-year flood plains, poor foundation areas, subsidence-prone areas, landslide-prone areas, wetlands, and karst terranes (limestones areas with fissures, sink-holes, underground streams, and caverns)."

While not violating the current site requirements, the site is assumed on a local topographic high point. The water table is located about 24 m below the land surface. The aquifer is 25 m thick and is confined from below by an impermeable bedrock.

Table 1 lists the geological parameters which could be used to characterize the hypothesized site if groundwater contamination were to be studied. The choice of this parameter set is consistent with a hypothesized site used for disposal of low-level radioactive wastes [2]. The characteristics are permissible under the current RCRA regulations [4]; of course, a wide variety of sites are in actual use.

Actual sites would vary in their characteristics from that of the hypothesized site. For example, porosity might be 0.35. However, such differences are not important herein since these site characteristics were not used in these calculational results. A groundwater source was not modeled quantitatively in the risk assessment.

3. Carcinogenicity and current usage of several metals

The contaminants considered in the sites are several metals and their compounds. Five metals which are carcinogenic are listed in Table 2 [5]. In the EPA weight-of evidence classification system for carcinogenicity, A stands for human carcinogen, B1 stands for probable human carcinogen, and B2 stands

TABLE 2

Carcinogenic group of metals (adapted from Ref. [5])

Metal	EPA Group	Description
As	A	Human carcinogen, sufficient human evidence
Be	B2	Probable human carcinogen, inadequate human evidence, sufficient animal evidence
Cd	B1	Probable human carcinogen, limited human evidence
Cr(VI)	A	Human carcinogen, sufficient human evidence
Ni (subsulfide)	A	Human carcinogen, sufficient human evidence

TABLE 3

Annual production of the four metals (data collected from Ref. [6])

Metal	Total annual world production (metric tons)	Year of production
As	60,000	1975–1977
Be	10,000	not specified
Cd	12,000	1980
Cr	8,600,000	1976
Ni	660,000	1973

for probable human carcinogen with limited human evidence, but with sufficient animal evidence. Arsenic, chromium (VI), and nickel (subsulfide) are considered by EPA to be sufficient for them to be labeled as carcinogens. For cadmium, EPA considers human evidence as to its carcinogenicity to be limited; hence cadmium is ranked lower (category B1) in Table 2. Beryllium belongs to category B2.

Annual production of these five metals are listed in Table 3 [6]. It can be seen that the amount of metals used is large. After the technologically useful lifetime of those products containing these metals, one or more RCRA sites is needed to dispose of them. Recycle of all the metals is impractical. The costs to separate and encapsulate the vast tonnage of most of these widely used carcinogens would be very large, even more so for existing wastes.

Carcinogenicity data of these five metals are listed in Table 4. The slope factor is usually, but not always, the upper 95th percent confidence limit of the slope of the dose–response curve and is expressed as $(mg/kg\text{-}day)^{-1}$ [7]. It represents the lifetime excess cancer risk per unit dose. Usually, the slope factors are different for inhalation and ingestion. They are related to the unit risks as follows [7]:

$$\text{air unit risk} = \text{risk per } \mu g/m^3 = \text{slope factor} \times 1/70\ kg \times 20\ m^3/day \times 10^{-3}$$

TABLE 4

Unit risks and slope factors of five metals

Metal	Air unit risk[a] $(\mu g/m^3)^{-1}$	Slope factor for inhalation[b] $(mg/kg\text{-}day)^{-1}$	Water unit risk $(\mu g/L)^{-1}$	Slope factor for ingestion $(mg/kg\text{-}day)^{-1}$
As	4.3×10^{-3}	15	5.1×10^{-4}[c]	18[d]
Cr(VI)	1.2×10^{-2}	42	–[e]	–[e]
Ni (subsulfide)	4.8×10^{-4}	1.7	–[e]	–[e]
Cd	1.8×10^{-3}	6.3	–[e]	–[e]
Be	2.4×10^{-3}	8.4	1.2×10^{-4}[f]	4.3[f]

[a] Data in this column is taken from IRIS [8].
[b] Calculated from air unit risk, using 20 m^3/day as the inhalation rate.
[c] Calculated from slope factor for ingestion, using 2 L/day as the ingestion rate.
[d] Calculated based on data from Smith et al. [9].
[e] No data is available.
[f] Taken from IRIS [8].

and

water unit risk = risk per $\mu g/L$ = slope factor $\times$ 1/70 kg $\times$ 2 L/day $\times 10^{-3}$

Several aspects of these five metals are discussed in the following.

3.1 Arsenic

Epidemiological studies have indicated that exposure via ingestion to inorganic arsenic compounds in drugs and drinking water is causally related to the development of skin cancer in humans. Exposure to arsenic trioxide by inhalation is clearly related to the development of lung cancer in certain smelter workers [5]. The Integrated Risk Information System (IRIS) [8], an EPA on-line data base, gives an air unit risk of 4.3×10^{-3} $(mg/m^3)^{-1}$. Therefore an inhalation slope factor of 15 $(mg/kg\text{-}day)^{-1}$ can be calculated. The IRIS also gives a water unit risk of 5×10^{-5} $(\mu g/L)^{-1}$ for skin cancer due to ingestion of arsenic in water. A corresponding ingestion slope factor is 1.8 $(mg/kg\text{-}day)^{-1}$. However, Smith et al. [9] reported that arsenic can also cause liver, lung, kidney, and bladder cancer. They estimated that at the current EPA drinking water standard of 50 $\mu g/L$, the lifetime risk of dying from cancer of the liver, lung, kidney, or bladder from drinking 1 L/day of water could be as high as 13 per 1000 persons. A ingestion slope factor of 18 $(mg/kg\text{-}day)^{-1}$ can be calculated; this value is listed in Table 4. Also, Anderson [10] gave a ingestion slope factor of 14.0 $(mg/kg\text{-}day)^{-1}$ for arsenic.

The major current uses of arsenic [6] are as pesticides, e.g., lead arsenate, calcium arsenate, and sodium arsenite, herbicides, and cotton desiccants. Elemental arsenic is utilized as an additive in the production of several alloys

to increase hardness and heat resistance. Gallium arsenide, an artificial crystal, has become an important material in the manufacture of integrated circuits.

3.2 Chromium (VI)

Epidemiologic studies of chromate production facilities in the United States, Great Britain, Japan, and Germany have established an association between chromium exposure and lung cancer [8]. According to IRIS, chromium-exposed workers are exposed to both chromium III and chromium VI compounds. However, only chromium VI has been found to be carcinogenic in animal studies. Therefore, only chromium VI is concluded as carcinogenic. The inhalation unit risk of chromium is 1.2×10^{-2} $(\mu g/m^3)^{-1}$ [8], which corresponds to a inhalation slope factor of 42 $(mg/kg\text{-}day)^{-1}$. No data is reported in IRIS regarding the ingestion slope factor for chromium. However, in the National Primary Drinking Water Regulations (40 CFR parts 141, 142, 143), EPA concludes that the presence of chromium (VI) in drinking water should be minimized in recognition of its biological reactivity including its potential for a carcinogenic hazard, and recommends that the uncertainty regarding chromium (VI) carcinogenic risk in drinking water warrants additional investigation. Cohen used a ratio of oral slope factor/inhalation slope factor of 1/10 to derive an oral slope factor for chromium [11].

The principal industrial consumers of chromium are the metallurgical, refractory and chemical industries [6]. The U.S. figures for consumption by these industries were 60%, 20% and 20%, respectively.

3.3 Nickel

Increased risks of lung and nasal cancer have been reported in humans exposed to nickel refinery dust, most of which was believed to have been nickel subsulfide [8]. The IRIS gives an air unit risk of 4.8×10^{-4} $(\mu g/m^3)^{-1}$, which corresponds to an inhalation slope factor of 1.7 $(mg/kg\text{-}day)^{-1}$ for nickel (subsulfide). No data has been reported regarding the ingestion slope factor.

About 40% of the nickel produced is used in steel production [6]. Nickel is also used in the production of other alloys, for which reason nickel can be found in coins and household utensils. Electroplating using nickel sulfate accounts for 20% of the nickel produced. Nickel hydroxide is used in nickel–cadmium batteries. Nickel carbonate serves in electronic components, such as vacuum tubes and transistor cans.

3.4 Cadmium

Limited evidence from occupational epidemiologic studies of cadmium is consistent across investigators and study populations [8]. Occupational exposure to cadmium (primarily as the oxide) increases the risk of prostate, respiratory, and genitourinary cancers in humans [5]. Excess cancer risk of lung cancer was observed in cadmium smelter workers [8]. There is sufficient evidence of carcinogenicity in rats and mice by inhalation and intramuscular and

subcutaneous injection [8]. Seven studies in rats and mice wherein cadmium salts (acetate, sulfate, chloride) were administered orally have shown no evidence of carcinogenic response [8]. The IRIS gives an air unit risk of 1.8×10^{-3} $(\mu g/m^3)^{-1}$, which corresponds to an inhalation slope factor of 6.3 $(mg/kg\text{-}day)^{-1}$. According to 40 CFR parts 141, 142, 143, "chronic oral animal studies with cadmium have shown kidney damage but no carcinogenic activity and ingestion-specific human data are not available". Also, "those comments that conclude that cadmium is a carcinogen provide no new evidence that cadmium is carcinogenic via drinking water but rather, argue that it is prudent to assume that cadmium is carcinogenic via ingestion". Cohen gives a ratio of oral slope factor/inhalation slope factor of 1/3 in his study [11].

Cadmium is used in a number of industrial processes, but for most of its uses there are alternatives of lower toxicity [6]. In the U.S., 60% of the cadmium produced or imported was used for plating, 11% in color pigments, 19% as stabilizers in plastics, 3% in accumulators, and 7% for other purposes.

3.5 Beryllium

Beryllium has been shown to induce lung cancer via inhalation in rats and monkeys and to induce osteosarcomas in rabbits via intravenous or intramedullary injection [8]. Human epidemiology studies are considered to be inadequate [8]. The IRIS gives an air unit risk of 2.4×10^{-3} $(\mu g/m^3)^{-1}$, which corresponds to an inhalation slope factor of 8.4 $(mg/kg\text{-}day)^{-1}$. The water unit risk of 1.2×10^{-4} $(\mu g/L)^{-1}$ and ingestion slope factor of 4.3 $(mg/kg\text{-}day)^{-1}$ are both taken from IRIS. Anderson [10] reported the ingestion slope factor of 4.9 $(mg/kg\text{-}day)^{-1}$ derived from the linearized multistage model and 3.4 $(mg/kg\text{-}day)^{-1}$ derived from the one-hit model.

About 20% of the world production of beryllium is used as free metals. Beryllium alloys account for about 72% of the total production. The master alloy is 96% copper and 4% beryllium. The remaining 8% of beryllium produced is used as the oxide in ceramic formulations [6].

4. Wastes treatment and treatment standards

As mentioned, the hazardous waste has to be treated before land disposal. Stabilization and Solidification are commonly used treatment methods. For inorganic wastes stabilization/solidification, there are two recommended methods which are used for setting Best Demonstrated Alternative Technology (BDAT) standards for many wastes [12]. These are cement-based stabilization/solidification and pozzolanic stabilization/solidification. Descriptions about these two technologies are adapted from reference [12] as follows:

"Cement-based stabilization/solidification is a process in which waste materials are mixed with portland cement. Water is added to the mixture to ensure proper hydration reactions necessary for bonding the cement. The wastes are

incorporated into the cement matrix and, in some cases, undergo physical-chemical changes that further reduce their mobility in the waste–cement matrix. Typically, hydroxides of metals are formed, which are much less soluble than ionic species of the metals. The final product may vary from a granular, soil-like material to a cohesive solid, depending on the amount of reagent added and the types and amounts of wastes stabilized/solidified. The Cement-based stabilization/solidification has been applied to plating wastes containing various materials such as cadmium, chromium, copper, lead, nickel, and zinc, etc."

"Pozzolanic stabilization/solidification involves siliceous and aluminosilicate materials, which do not display cementing action alone, but form cementitious substances when combined with lime or cement and water at ambient temperatures. The primary containment mechanism is the physical entrapment of the contaminant in the pozzolan matrix. Examples of common pozzolans are fly ash, pumice, lime kiln dusts, and blast furnace slag. Pozzolans contain significant amounts of silicates, which distinguish them from the lime-based materials. The final product can vary from a soft fine-grained material to a hard cohesive material similar in appearance to cement. Pozzolanic reactions are generally much slower than cement reactions. Waste materials that have been stabilized/solidified with pozzolans include oil sludges, plating sludges containing various metals (aluminium, nickel, copper, lead, chromium, and arsenic), waste acid, and creosote."

Both cement-based and pozzolanic stabilization/solidification aim at immobilizing the metals in the wastes, instead of removing the metals permanently. The choice of treatment technology as well as achievable standards are much waste type dependent.

The land disposal restrictions, codified in 40 CFR 268, place stringent controls on the land disposal of hazardous wastes [4]. Congress set forth a schedule of land disposal restrictions in HSWA. The statute automatically prohibited the land disposal of hazardous wastes if EPA failed to set a treatment standard by the statutory deadline. The statute also required EPA to make determinations on prohibiting land disposal, within the indicated time frames, for the following:

1. At least one-third of all ranked and listed hazardous wastes by August 8, 1988.
2. At least two-thirds of all ranked and listed hazardous wastes by June 8, 1989.
3. All remaining ranked and listed hazardous wastes and all hazardous wastes identified by a characteristic by May 8, 1990.

Within the first third wastes, there are K101 and K102 wastes. K101 wastes are distillation tar residues from the distillation of aniline-based compounds in the production of veterinary pharmaceuticals from arsenic or organo-arsenic compounds (40 CFR 268.10). K102 wastes are residues from the use of activated carbon for dechlorization in the production of veterinary pharmaceuticals from arsenic or organo-arsenic compounds (40 CFR 268.10).

TABLE 5

BDAT Treatment standards for K101 waste [12] (nonwaste waters) (Low arsenic subcategory — less than 1% arsenic)

Constituent	Maximum for any single grab samples	
	Total composition (mg/kg)	TCLP (mg/L)
Ortho-nitroaniline	14	(1)
Cadmium	(1)	0.066
Chromium (total)	(1)	5.2
Lead	(1)	0.51
Nickel	(1)	0.32

(1) Not applicable.

On August 17, 1988, EPA promulgated treatment standards for hazardous wastes listed in 40 CFR 268.10. For K101 and K102 wastes (ash residues), the Best Demonstrated Available Technology chosen is stabilization [12]. EPA also established BDAT treatment standards. The BDAT standards for K101 waste are shown in Table 5. While these standards are derived based on BDAT, they are concentration standards. In other words, any technology satisfying this standard is acceptable. The BDAT standards for K102 wastes are the same as given in Table 5.

In Table 5, TCLP is the Toxicity Characteristic Leaching Procedure (Federal Register 1986). It presumably represents the maximum leaching concentration of the waste. It can be seen from the table, for metals cadmium, chromium, and nickel, only TCLP is specified. No limits are given on the total composition of these metals.

5. The waste inventory of the hypothesized RCRA site

Based on the above discussion, we can hypothesize a RCRA site containing considerable amounts of arsenic and other metals. For simplicity, it can be assumed that the waste consists mainly of distillation tar residues from the production of veterinary pharmaceuticals (i.e., K101 wastes), which can have up to 1% weight content of arsenic. Also, other kinds of waste which contains more of chromium, cadmium, nickel, and beryllium have been mixed with the K101 waste. The stabilization process has been chosen to treat the mixture of these wastes. The treated wastes are assumed fine grained, soil-like in form and meet the TCLP standards as discussed above. So conceivably, one can have a RCRA site of the inventory as shown in Table 6. The maximum allowed leachate concentration of arsenic is set to comply with the Toxicity Characteristic Level of 5.0 mg/L [4].

TABLE 6

Inventory of the hypothesized RCRA site

Metal	Weight content (mg/kg)	Maximum allowed leachate concentration (mg/L)
Arsenic	1,000	5.0
Beryllium	100	N.A.
Cadmium	100	0.066
Chromium	100	5.2
Nickel	100	0.32

6. Scenarios for future risk assessment

It should be acknowledged that EPA indeed considers the near future situation of a RCRA site. For example, EPA currently requires that a site is not in a seismic active region and it should not be in a 100 year flood plain. Also, leachate collection and post-closure monitoring for groundwater contamination should last for 30 years.

However, in contrast to the stringent standards EPA imposed on the geological disposal of high level radioactive wastes [1] as well as the long term consideration of low level radioactive waste disposal [2], the requirement of long term risk assessment for RCRA site disposal of persistent carcinogenic metals is lacking. The authors believe there is an inconsistency in current regulation practices. Therefore in this text, an effort is made to do a future risk assessment of the hypothesized RCRA site, given that the societal memory has been lost in a distant future, e.g., a thousand years later.

Two scenarios are considered in this study. One is a human intrusion scenario, the other is a residential scenario down-gradient of the site.

6.1 Human intrusion

A human intrusion scenario similar to that analyzed for a low-level radioactive waste disposal site [2] is considered. It is assumed that 1000 years after the site closure, a group of farmer families intrude the site. During this 1000 years, there is a thousand-year flood which washes out the caps of the site. The farmers excavate the disposal facility area and build houses directly on the site as shown in Fig. 2. The farmers dig wells just down gradient of the waste disposal facility. The groundwater serves for their family's drinking water and is also used to irrigate the fruits and vegetables in case the weather is dry. The families consume part of the fruits and vegetables produced on the site. The farmers contact the soil during various activities.

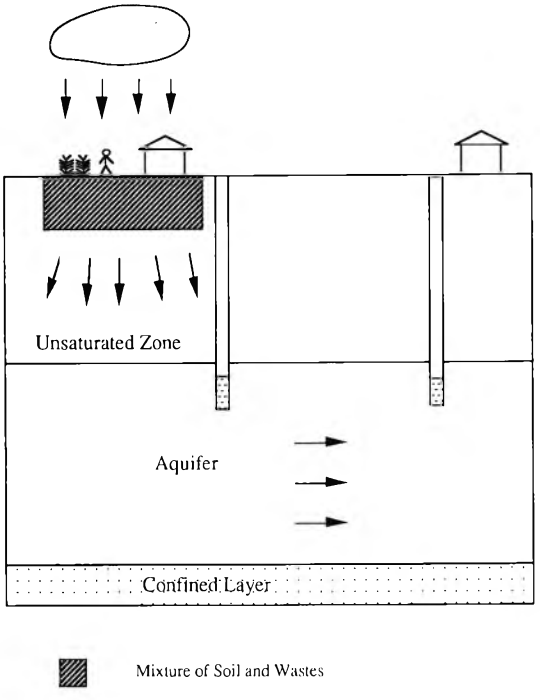

Fig. 2. Intrusion and residential scenarios.

6.2 Residential scenario (1000 m down-gradient of the site)

It is assumed that present day precipitation and infiltration data do not change dramatically in the future. The precipitation at the site will cause percolation of water through the cover system of the facility into the disposal units. The double liners and leachate collection system are assumed to lose functionality after 100 years of site closure. The wastes might be transported down into the aquifer and be further transported in the aquifer.

Suppose at 1000 years a community resides 1000 m down-gradient of the groundwater flow direction from the site and people use groundwater as their drinking water. The cancer risk should be considered.

7. Exposure pathway modeling

7.1 Inventory losses

We assume the site inventory can be approximated by an exponential loss equation as follows

$$m_i(t) = m_{i,0}\, e^{-\lambda t} \tag{1}$$

where $m_i(t)$ is the mass inventory of metal i at time t after the liners lose their functions. Here, i refers to five metals arsenic, chromium, cadmium, nickel, and beryllium. $m_i(t)$ accounts for all the forms of metal i; $m_{i,0}(t)$ is the initial mass inventory of metal i. The inventory loss rate, λ, can be expressed as

$$\lambda = \ln 2/T_{1/2} \tag{2}$$

where $T_{1/2}$ is the half time of inventory losses. The basic loss mechanism is leachate into the soil and then groundwater. If metal i changes from one chemical form to another, it is not counted as a loss.

It can be assumed that the total volume of the wastes does not change with time, so the metal concentration also observes an exponential law, i.e.

$$C_{s,i}(t) = C_{s,i,0}\, e^{-\lambda t} \tag{3}$$

where $C_{s,i}(t)$ (mg/kg) is the concentration of metal i at time t. The value of $C_{s,i,0}$ has been listed in Table 6.

The loss rate λ depends on many factors, such as pH level of the soil, the infiltration rate, total metal inventory in the site, the area of the site, etc. In this analysis, we assume that after liners lose their functions, the initial leachate concentration does not exceed that given in column 3 of Table 6. This assumption gives a very small loss rate λ. As a result, the metal concentration at 1000 years does not change very much from the initial concentration; this is effectively the case with $\lambda = 0$. We thus use the initial weight concentration in column 2 of Table 6 for $C_{s,i}$ in the human intrusion scenario. It is noted that the treatment of λ herein neglects the groundwater contamination, which might be an important pathway. A realistic value of the loss rate λ is needed for more elaborate models on this topic.

7.2 Human intrusion scenario

In principle, there are at least five pathways considered possible for the human intrusion scenario. They are: ingestion of contaminated groundwater, inhalation of dust containing metal carcinogens, ingestion of contaminated fruits and vegetables, dermal contact with contaminants in the soil, and ingestion of metals in the soil.

There are large uncertainties in modelling groundwater contamination for carcinogenic metals. These include the effect of retardation, uncertainties about the influence of chemical reactions, and uncertainties in geological configuration. The groundwater ingestion pathway is not modeled herein because: (1) we use a zero loss rate λ; (2) the heavy metals are believed to have low mobility in the ground. But groundwater contamination may be a significant contributor to risk for the human intrusion scenario. The inhalation of dust pathway is not considered quantitatively, either, due to large uncertainties.

7.2.1 Fruit and vegetable ingestion

Homegrown vegetables and fruits are classified into three groups, i.e. leafy vegetables, exposed produce, and protected produce [5]. Leafy vegetables present a broad, flat leaf surface for direct interception of depositing pollutant. Exposed produce such as tomatoes, apples, etc. present edible portions for direct deposition pathway, but edible portions generally have reproductive functions and are associated with significantly different soil–plant uptake parameters than leafy vegetables. Protected produce such as potatoes and citrus fruits do not have edible portions exposed to direct atmospheric deposition. Like exposed produce, edible portions are not vegetative in nature. Therefore, the soil–plant transfer coefficient of a pollutant for vegetative portions is applied to the soil–plant uptake for leafy vegetables while the transfer coefficient of the pollutant for reproductive portions is applied to the soil–plant uptake for exposed or protected produce.

Neglecting the atmospheric deposition, the concentration of contaminant in homegrown fruits and vegetables can be calculated as [5]

$$C_{P,i}=(B_v \text{ or } B_r)C_{s,i} \tag{4}$$

where $C_{s,i}$ (mg/kg) is the contaminant concentration as calculated in (3). B_v is the soil–plant elemental transfer coefficient for vegetative portions (unitless), B_r is the soil–plant elemental transfer coefficient for reproductive portions (unitless). Table 7 [5] represents the soil-to-plant transfer coefficient for different metals.

The fruit and vegetable intake can be estimated as [5]

$$IT_{FV,i}=\frac{C_{P,i}\times IR\times FI\times EF\times ED}{BW\times AT} \tag{5}$$

where $IT_{FV,i}$ is the fruit and vegetable intake of contaminant i (mg/kg · day), $C_{P,i}$ (mg/kg) is contaminant concentration in fruits and vegetables as calculated in (4), and IR (kg/day) is the ingestion rate. Total daily consumption rate for each category of vegetable and fruit is assumed to be 38 g/day for leafy vegetables, 82 g/day for exposed produce and 153 g/day for protected produce,

TABLE 7

Soil-to-plant transfer coefficient (adapted from Ref. [5])

Pollutant	B_v	B_r
As	0.040	6.0×10^{-3}
Be	0.01	1.5×10^{-3}
Cd	0.55	0.15
Cr	7.5×10^{-3}	4.5×10^{-3}
Ni	0.060	0.060

respectively [5]. Therefore, the ingestion rate for vegetative portions is 0.038 kg/day (leafy vegetables and fruits), and the ingestion rate for reproductive portions is 0.235 kg/day (sum of exposed produce and protective produce). FI is fraction ingested from a contaminated source. The home grown portion of total vegetable and fruit consumed is assumed to be 25% regardless of the category [5]. Therefore FI is taken 0.25 for both vegetative and reproductive portions. EF (days/year) is the exposure frequency, for which a value of 365 day/y is assumed. $ED = 70$ years is exposure duration; $BW = 70$ kg is body weight; and $AT = 70\ \text{y} \times 365$ days/y is the averaging time. It is noted that no allowance is made for contaminated water in this calculation.

To calculate the lifetime cancer risk, a proper dose–response model should be used. For extrapolating from high dose to low dose, "EPA's guidelines recommend that the linearized multistage model be employed in the absence of adequate information to the contrary. Among the other models available are the Weibull, probit, logit, one-hit, and gamma multihit models, as well as various time-to-tumor models" [7].

Since the intake in this analysis might be high, we choose the one-hit equation for risk calculation. The lifetime excess cancer risk due to fruit and vegetable intake can be calculated as [7]

$$R_{\text{FV},i} = 1 - \exp(-IT_{\text{FV},i} \times SF_i) \tag{6}$$

where $R_{\text{FV},i}$ is the cancer risk posed by metal i; and SF_i is the ingestion slope factor for metal i. as shown in Table 4.

7.2.2 Dermal contact with metals in soil

The absorbed dose due to dermal contact with chemicals in soil $IT_{\text{AD},i}$ (mg/kg day) can be calculated as [7]

$$IT_{\text{AD},i} = \frac{C_{\text{S},i} \times CF \times SA \times AF \times ABS \times EF \times ED}{BW \times AT} \tag{7}$$

where $C_{\text{S},i}$ is the chemical concentration in soil (mg/kg) as calculated in (3); $CF = 10^{-6}$ kg/mg is the conversion factor; SA is the skin surface area available for contact (cm^2/event), the 50th percentile body part-specific surface areas for males is 0.23 m^2 for arms, 0.082 m^2 for hands and 0.55 m^2 for legs, hence SA is assumed to be the sum of these areas, i.e., 8620 cm^2; AF is the soil to skin adherence factor (mg/cm^2). It is assumed that a layer of soil with particle size 0.01 mm forms on the skin, the soil density is assumed to be 2 g/cm^3, the product of thickness and soil density gives an AF value of 2 mg/cm^2; ABS is the absorption factor, a value of 0.1 is assumed; EF is the exposure frequency, a value of 100 events/year is assumed; ED, BW, and AT have the same values as discussed above.

The risk due to dermal contact with chemical i in soil $R_{\text{DC},i}$ is

$$R_{\text{DC},i} = 1 - \exp(-IT_{\text{AD},i} \times SF_i) \tag{8}$$

7.2.3 Ingestion of metals in soil

The intake of metal i, $IT_{SI,i}$ (mg/kg day), due to ingestion of soil can be expressed as [7]

$$IT_{SI,i} = \frac{C_{S,i} \times IR \times CF \times FI \times EF \times ED}{BW \times AT} \tag{9}$$

where $C_{S,i}$ is the chemical concentration in soil (mg/kg) as calculated in (3); $IR = 100$ mg/day is the ingestion rate for the age group greater than 6 years old; $CF = 10^{-6}$ kg/mg is the conversion factor; FI is the fraction ingested from contaminated sources, a value of 0.1 is chosen for FI; $EF = 365$ days/year is the exposure frequency. ED, BW, and AT have the same meaning and values as discussed before.

The risk due to soil ingestion can be calculated as

$$R_{SI,i} = 1 - \exp(-IT_{SI,i} \times SF_i) \tag{10}$$

7.3 Residential scenario

For the residential scenario, it is assumed that the groundwater intake is the primary concern.

According to Wagner [4], RCRA section 3004(d) requires that petitioner for a RCRA site demonstrate, to a reasonable degree of certainty, that there will be no migration of hazardous constituents from the disposal unit or injection zone for as long as the waste remain hazardous. It seems to the authors that this requirement might not be met, given the current RCRA regulation imposed by EPA. First, carcinogenic metals are persistent, their toxicity might remain forever. Secondly, many compounds of these metals are soluble, thereby it is conceivable that the metal compound may be transported down into the aquifer by infiltration if some conditions are met (e.g., pH becomes small), and they might be transported further down gradient in the aquifer. Table 8 lists some metal compounds with high solubility [13].

In a report to the Congress [14], EPA assessed the potential health effects of the waste disposal sites of the U.S. coal power plants. These power plants generate fly ash, bottom ash, boiler slag, and flue gas desulfurization wastes which contains the carcinogenic metals we have discussed. According to the report, "while most of the laboratory results indicated that coal combustion wastes do not possess RCRA hazardous characteristics, in some instances, data on actual field observations indicates that migration of potentially hazardous constitutes from utility wastes disposal sites has occurred. For example, observed concentrations of contaminants found in groundwater down-gradient from the sites exceed the primary drinking water standards about 5% of the time".

Based on the above discussion, groundwater contamination down-gradient of our hypothesized site might be possible. However, due to large uncertainties about models and available data, a quantitative assessment of the residential scenario has not been performed in this analysis.

TABLE 8

Some soluble metal compounds [13]

Name	Formula	Solubility (g/dL)
Ortho-arsenic	$H_3AsO_4 \cdot \frac{1}{2}H_2O$	302
Arsenic tri-iodide	AsI_3	6.0
Arsenic penta-oxide	As_2O_5	150
Arsenic trioxide	As_2O_3	3.7
Chromate	$(NH_4)_2CrO_4$	40.5
Dichromate	$(NH_4)_2Cr_2O_7$	30.8
Chromium chloride, hexahydrate	$[Cr(H_2O)_4Cl_2]Cl \cdot 2H_2O$	58.5
Chromium sulfate	$Cr_2(SO_4)_3 \cdot 18H_2O$	120
Nickel bromide, trihydrate	$NiBr_2 \cdot 3H_2O$	199
Nickel perchlorate	$Ni(ClO_2)_2 \cdot 6H_2O$	222.5
Nickel chloride, hexahydrate	$NiCl_2 \cdot 6H_2O$	254.0
Nickel nitrate, hexahydrate	$Ni(NO_3) \cdot 6H_2O$	238.5
Cadmium borotungstate	$Cd_5(BW_{12}O_{40})_2 \cdot 18H_2O$	1250
Cadmium chlorate	$Cd(ClO_3)_2 \cdot 2H_2O$	298
Cadmium nitrate	$Cd(NO_3)_2$	109
Cadmium sulfate hydrate	$3CdSO_4 \cdot 8H_2O$	113
Beryllium oxalate	$BeC_2O_4 \cdot 3H_2O$	38.22
Beryllium oxide	BeO	0.00002
Beryllium selenate	$BeSeO_4 \cdot 4H_2O$	56.7
Beryllium sulfate, hydrate	$BeSO_4 \cdot H_2O$	42.4

8. Results for human intrusion scenario

This section presents the calculational results of lifetime excess cancer risk for the human intrusion scenario. In order to see the influence of carcinogenicity data, we show results for two cases herein, one is denoted as the "base case", the other is denoted as the "revised base case". These two cases differ in the use of oral slope factors, as shown in Table 9. The oral slope factors in the base case are the same as listed in Table 4. In the revised base case, we add the arsenic oral slope factor of 1.8 $(mg/kg\text{-}day)^{-1}$ due to skin cancer [8] to the base case arsenic oral slope factor of 18 $(mg/kg\text{-}day)^{-1}$, which accounts for cancer in liver, lung, kidney, and bladder, and get an arsenic oral slope factor of 19.8 $(mg/kg\text{-}day)^{-1}$ for all cancer sites. Also in the revised case, the oral slope factor of chromium is assumed one tenth of its inhalation slope factor. And the oral slope factor of cadmium is assumed one third of its inhalation slope factor. These ratios are taken from a study by Cohen [11]. EPA itself professes uncertainty about the ingestion carcinogenicity path for chromium. For cadmium, EPA's non-carcinogenic conclusion via the ingestion is not based on strong, conclusive data; hence, we use Cohen's estimate for illustrative purposes.

TABLE 9

Slope factors for ingestion pathway

Metal	Oral slope factor for the base case (mg/kg-day)$^{-1}$	Oral slope factor for the revised base case (mg/kg-day)$^{-1}$
As	18	19.8[a]
Cr (VI)	–	4.2[b]
Ni (subsulfide)	–	–
Cd	–	2.1[c]
Be	4.3	4.3

[a] Summation of the base case slope factor (18) and the slope factor for skin cancer (1.8), the latter is calculated from water unit risk of 5×10^{-5} (μg/L)$^{-1}$, which is taken from IRIS [8], an ingestion rate of 2 L/day is used in the calculation.
[b] Value taken as one tenth of the slope factor for inhalation, this ratio is taken from Cohen [11].
[c] Value taken as one third of the slope factor for inhalation, this ratio is taken from Cohen [11].

TABLE 10

Excess cancer risk due to fruit and vegetable intake — vegetative portion

Metal	Soil concentration (mg/kg)	C_{pv} (mg/kg)	Intake (mg/kg day)	Risk
As	1,000	40	5.43×10^{-3}	9.31×10^{-2}
Be	100	1	1.36×10^{-4}	5.85×10^{-4}
Cd	100	55	7.46×10^{-3}	–
Cr	100	0.75	1.02×10^{-4}	–
Ni	100	6	8.14×10^{-4}	–

8.1 Base case results

Table 10 and Table 11 represent the risk calculation for fruit and vegetable intake. Table 10 shows the risk due to the vegetative portion intake and Table 11 shows the risk due to the reproductive portion intake. Total risk for the vegetative portion is 9.37×10^{-2} and that for the reproductive portion is 8.72×10^{-2}. Total risk due to fruit and vegetable intake is 0.18.

Table 12 represents the result for dermal contact with metals in soil. The total risk for this pathway is 0.12.

Table 13 represents the risk due to ingestion of metals in soil. The total risk of this pathway is 2.6×10^{-3}.

Table 14 lists the summary results for the base case. The total risk of the human intrusion scenario is 0.30. It is clear that the risk for the human

TABLE 11

Excess cancer risk due to fruit and vegetable intake—reproductive portion

Metal	Soil concentration (mg/kg)	C_{pr} (mg/kg)	Intake (mg/kg day)	Risk
As	1,000	6.0	5.04×10^{-3}	8.67×10^{-2}
Be	100	0.15	1.26×10^{-4}	5.42×10^{-4}
Cd	100	15	1.26×10^{-2}	–
Cr	100	0.45	3.78×10^{-4}	–
Ni	100	6.0	5.04×10^{-3}	–

TABLE 12

Excess cancer risk due to dermal contact with contaminants in soil

Metal	Soil concentration (mg/kg)	Absorbed dose (mg/kg day)	Risk
As	1,000	6.75×10^{-3}	0.114
Be	100	6.75×10^{-4}	2.90×10^{-3}
Cd	100	6.75×10^{-4}	–
Cr	100	6.75×10^{-4}	–
Ni	100	6.75×10^{-4}	–

TABLE 13

Excess cancer risk due to ingestion of metals in soil

Metal	Soil concentration (mg/kg)	Intake (mg/kg day)	Risk
As	1,000	1.43×10^{-4}	2.57×10^{-3}
Be	100	1.43×10^{-5}	6.15×10^{-5}
Cd	100	1.43×10^{-5}	–
Cr	100	1.43×10^{-5}	–
Ni	100	1.43×10^{-5}	–

intrusion scenario is large, and might be significantly enhanced by drinking contaminated groundwater and inhalation of the dust containing metals.

8.2 Results for the revised base case

Results for the revised base case are summarized in Table 15. The total risk of the revised case is 0.38. It can be observed that arsenic dominates the calculated risk in this study.

TABLE 14

Risk summary for base case

Metal	Fruit and vegetable ingestion (vegetative)	Fruit and vegetable ingestion (reproductive)	Dermal contact with soil	Ingestion of metals in the soil	Total risk for each metal
As	9.31×10^{-2}	8.67×10^{-2}	0.114	2.57×10^{-3}	0.296
Cr	–	–	–	–	–
Ni	–	–	–	–	–
Cd	–	–	–	–	–
Be	5.85×10^{-4}	5.42×10^{-4}	2.90×10^{-3}	6.15×10^{-5}	4.09×10^{-3}
Total risk	9.37×10^{-2}	8.72×10^{-2}	0.117	2.63×10^{-3}	0.30

TABLE 15

Risk summary for revised base case

Metal	Fruit and vegetable ingestion (vegetative)	Fruit and vegetable ingestion (reproductive)	Dermal contact with soil	Ingestion of metals in the soil	Total risk for each metal
As	0.102	9.50×10^{-2}	0.125	2.83×10^{-3}	0.325
Cr	4.28×10^{-4}	1.59×10^{-3}	2.83×10^{-3}	6.01×10^{-5}	4.91×10^{-3}
Ni	–	–	–	–	–
Cd	1.55×10^{-2}	2.61×10^{-2}	1.42×10^{-3}	3.00×10^{-5}	4.31×10^{-2}
Be	5.85×10^{-4}	5.42×10^{-4}	2.90×10^{-3}	6.15×10^{-5}	4.09×10^{-3}
Total risk	0.119	0.123	0.132	2.98×10^{-3}	0.38

9. Discussion

While there is uncertainty in modeling the various pathways, this study indicates that the future risk for the human intrusion scenario for a hypothesized RCRA site is potentially intolerable, if one adopts the general rationale used in 40 CFR Part 191 for high level radioactive waste disposal [1]. The risk of the residential scenario has not been obtained quantitatively due to the large uncertainty, but potentially significant risk for this scenario can not be excluded. Although the risk calculated is one thousand years away in the future, as in 40 CFR 191, it is not assumed that the future generations would be more advanced in technology. Furthermore, societal memory regarding the site is assumed to be lost. This degree of conservatism is along the same lines as that chosen by U.S. EPA for high level radioactive waste disposal in a geological repository [1] and by the U.S. NRC for disposal of low level radioactive wastes [2].

In Superfund cleanup programs, consideration of risk into the far future is also lacking. Doty and Travis [15, 16] reviewed 50 EPA Records of Decisions made in Fiscal Year 1987. Among them, less than half (22) of the Records of Decisions documented quantitative future risk assessment. It is obvious that risk a thousand years away did not play a role in the superfund decision making process.

In summary, the U.S. EPA requirements concerning long-term risk from RCRA sites containing metal carcinogens which never change due to radioactive decay stand in sharp contrast to the stringent requirements over 10,000 years posed by EPA for high level radioactive waste disposal in 40 CFR 191 (remanded), and the long-term requirements posed by U.S. Nuclear Regulatory Commission for low level radioactive waste disposal sites.

Acknowledgments

This work was supported in part by the Toxic Substances Research and Teaching Program of the University of California. Dr. William E. Kastenberg and Mr. Don Browne have offered beneficial comments on this paper. We would like to express our gratefulness to both of them.

References

1 U.S. Environmental Protection Agency, Environmental Standard for the Management and disposal of Spent Nuclear Fuel, High-Level Waste, and Transuranic Radioactive Waste, Final Rule, Federal Register, 50, No.182, Washington, DC, 1985.
2 M.S.Y. Chu, M.W. Kozak, J.E. Campbell and B.M. Thompson, A Self-Teaching Curriculum for the NRC/SNL Low-Level Waste Performance Assessment methodology, NUREG/CR-5539, SAND90-0585, Albuquerque, NM, January 1991.
3 Minnesota Waste Management Board, Stabilization and Containment Draft Report on Facility Development, May 28, 1987. Obtained through personal communication with Mr. Don Browne.
4 T.P. Wagner, The Complete Guide to the Hazardous Waste Regulations, 2nd edn., Van Nostrand Reinhold, New York, 1991 (copyright by T.P. Wagner).
5 J. Lee, Health Risk Assessment of Incinerator Stack Emissions: Trace Metals, Ph.D. Dissertation for Doctor of Philosophy in Engineering, UCLA, 1990.
6 L. Friberg, G.F. Norberg and V.B. Vouk, Handbook on the Toxicology of Metals, Vol. II, Elsevier, Amsterdam, 1986.
7 U.S. Environmental Protection Agency, Risk Assessment Guidance for Superfund, Vol. I, Human Health Evaluation Manual (Part A), Interim Final, EPA/540/1-89/002, Dec., 1989.
8 U.S. Environmental Protection Agency, Integrated Risk Information System (IRIS), Accessed on-line in January, 1993.
9 A.H. Smith et al., Cancer risks from arsenic in drinking water, Environ. Health Perspectives, 97 (1992) 259–267.
10 E.L. Anderson et al., Quantitative approaches in use to assess cancer risk, Risk Anal., 3(4) (1983) 277–295.
11 B.L. Cohen, Long-term consequences of the linear-no threshold dose–response relationship for chemical carcinogens, Risk Anal., 1(4) (1981) 267–275.

12 U.S. Environmental Protection Agency, Stabilization/Solidification of CERCLA and RCRA Wastes, Physical Tests, Chemical Testing Procedures, Technology Screening, and Field Activities, EPA/625/6-89/022, May 1989.
13 R.C. Weast (Ed.), CRC Handbook of Chemistry and Physics, 70th edn., CRC Press, Boca Raton, FL, 1989–1990.
14 U.S. Environmental Protection Agency, Report to Congress, Wastes from the Combustion of Coal by Electric Utility Power Plants, EPA/530-SW-88-002, PB88-177977, Feb. 1988.
15 C.B. Doty and C.C. Travis, The Superfund Remedial Action Design Process, ORNL/M—780, DE 89 010160, Oak Ridge National Laboratory, Oak Ridge, TN, 1989.
16 C.B. Doty and C.C. Travis, The Superfund Remedial Action Process: A review of fifty Records of Decisions, J. Air Waste Manag. Assoc., 39(12) (1989) 1535–1543.

Journal of Hazardous Materials, 34 (1993) 385–391
Elsevier Science Publishers B.V., Amsterdam

Static charge development and impact sensitivity of high explosives

K. Raha* and J.S. Chhabra

Explosives Research and Development Laboratory, Sutarwadi, Pune-411 008 (India)

(Received December 6, 1989; accepted October 26, 1992)

Abstract

One of the causes of accidental explosion of explosives is due to static electricity. The present study deals with the development of static electric charge resulting from compression of single crystals of pentaerythritol tetranitrate (PETN), trinitrotoluene (TNT), *N*-2,4,6-tetranitro-*N*-methyl aniline (tetryl) and cyclotrimethylene trinitroamine (RDX). The charge developed on PETN and TNT is "true piezoelectric", whereas on tetryl and RDX, it is tensorial piezoelectric in nature. Measurement of the piezoelectric coefficient, dielectric constant and compressibility of these explosive crystals reveals the anisotropic character of these crystals. The static field developed under the laboratory experimental conditions, when extrapolated to the condition of detonation, bears an inverse relation with the figure of insensitivity of the respective high explosives.

1. Introduction

The development of piezoelectric charge on crystals of high explosives is a phenomenon of fundamental importance [1–6]. The molecular structure and the spatial orientation of the molecule in the three-dimensional periodic array of crystals determine the extent of polarization of the molecule under an applied stress. Some accidental explosions have been ascribed to static electricity [7–10]. Therefore, a study of the development of charge and the field produced thereby under an applied stress was considered important. Such studies made on PETN, RDX, TNT and tetryl are reported here.

2. Experimental methods

2.1 Growth of crystal

Large single crystals of PETN, RDX, TNT and tetryl were grown from their saturated solutions in acetone. Initially each explosive was purified by

*To whom correspondence should be addressed.

repeated crystallization from acetone solution. A saturated solution of each individual purified explosive was made at room temperature. Some seed crystals were obtained after a few days of storage in a clean environment. Large single crystals of approximately 3–5 cm in length were grown in 2–3 months using these seed crystals [11]. Good, blemishless portions of the crystals were chosen, cut and polished to get crystals of the desired shape and habit.

2.2 Measurement of charge

A special cell for measurement of charge developed on a crystal face under varying loads was designed and fabricated [11]. The crystal was held between two electrodes, one of which was grounded. The charge developed on the face was measured using a Kistler dual mode charge amplifier, Model 503-D 145 and recorded on a strip chart recorder. The quantity of charge generated under varying loads from 100 g to 2 kg was plotted graphically as charge *vs.* load. The piezoelectric coefficient d, viz. charge per unit force (picocoulombs/g) was obtained from the slope of the linear plot.

$d = \text{Charge (pC)}/\text{Load (g)}$

2.3 Measurement of dielectric constant

The dielectric constants of the crystals were calculated along each direction by measurement of the capacitance of the crystals. A Wayne–Kerr capacitance bridge and a specially designed point electrode assembly [11] were used for this purpose. The voltage generated in a given direction is calculated as:

$$V(\text{volts}) = \frac{Q(\text{coulombs})}{C(\text{farads})} = \frac{d \times \text{load}}{0.088\,54\,\varepsilon A/t}$$

where A is the area in cm^2, t is the thickness in cm and ε is the dielectric constant of the crystal.

2.4 Measurement of mechanical property

Compressibility of the crystals was measured with the Instron testing machine, Model No. TICM.

3. Results

Table 1 presents the average values of piezoelectric coefficients, dielectric constants and Young's modulus of single crystals of PETN along the directions perpendicular to (110) and (001) for over 25 crystals in each direction. It is observed that opposite charges are generated on opposite faces confirming the crystal's true piezoelectric nature. Secondly, the direction perpendicular to (110) is more compressible and develops more charge. Table 1 also presents the values for single crystals of TNT, RDX and tetryl. TNT is a "true piezoelectric"

TABLE 1

Piezoelectric coefficient, dielectric constant and Young's modulus for single crystals of PETN, RDX, Tetryl and TNT

Explosive	Directions perpendicular to	Piezoelectric coefficient ($\times$ 10 pC/g)	Dielectric constant	Young's modulus ($\times 10^{-6}$ g/cm^2)
PETN	(110)	(3.20 $\pm$ 0.40)	(3.50 $\pm$ 0.12)	(1.24 $\pm$ 0.30)
	(001)	(1.50 $\pm$ 0.30)	(4.57 $\pm$ 0.17)	(3.80 $\pm$ 0.80)
	(001)	(0.75–0.01)	(4.29 $\pm$ 0.04)	(1.25 $\pm$ 0.15)
RDX	(120)	(0.50–0.01)	(4.70 $\pm$ 0.02)	(4.80 $\pm$ 0.50)
	(110)	(0.50–0.05)	(4.25 $\pm$ 0.11)	(2.65 $\pm$ 0.30)
Tetryl	(011)	(0.30–0.05)	(4.88 $\pm$ 0.16)	(2.65 $\pm$ 0.50)
	(010)	(0.25 $\pm$ 0.05)	(3.19 $\pm$ 0.07)	(1.20 $\pm$ 0.40)
TNT	(001)	(0.07 $\pm$ 0.02)	(3.89 $\pm$ 0.23)	(3.20 $\pm$ 0.30)

TABLE 2

Maximum static electric field across the explosive crystals

Properties of the crystals	PETN	RDX	Tetryl	TNT
	Directions perpendicular to			
	(110)	(001)	(100)	(010)
Piezoelectric constant, ($\times 10^3$ pC/g)	3.20	0.75	0.50	0.25
Capacitance across 1 cm^3 crystal (pF)	0.31	0.38	0.38	0.28
Static field under 1 kg load (volt/cm)	10.33	1.97	1.33	0.89
Static field at threshold pressure ($\times 10^{-5}$ volt/cm)	94.0	29.9	27.9	22.3

in nature and the direction perpendicular to (010) develops more charge and is more compressible. The Young's modulus of TNT along the direction perpendicular to (010) has been found to vary from 1.20×10^6 to 0.40×10^6 g/cm^2. Single crystals of RDX and tetryl behave in a unique way, which is reflected in the varying values of piezoelectric coefficients. The piezoelectric coefficients for RDX were found to vary from 0.75×10^{-3} to 0.01×10^{-3} pC/g and 0.50×10^{-3} to 0.01×10^{-3} pC/g for the directions perpendicular to (001) and (120) respectively. Similarly for tetryl, the static charge development was found to vary over a wide range. Both RDX and tetryl develop like charges on opposite faces. Further, it has been found that the directions perpendicular to (001) and (100) respectively develop more charge and are more compressible.

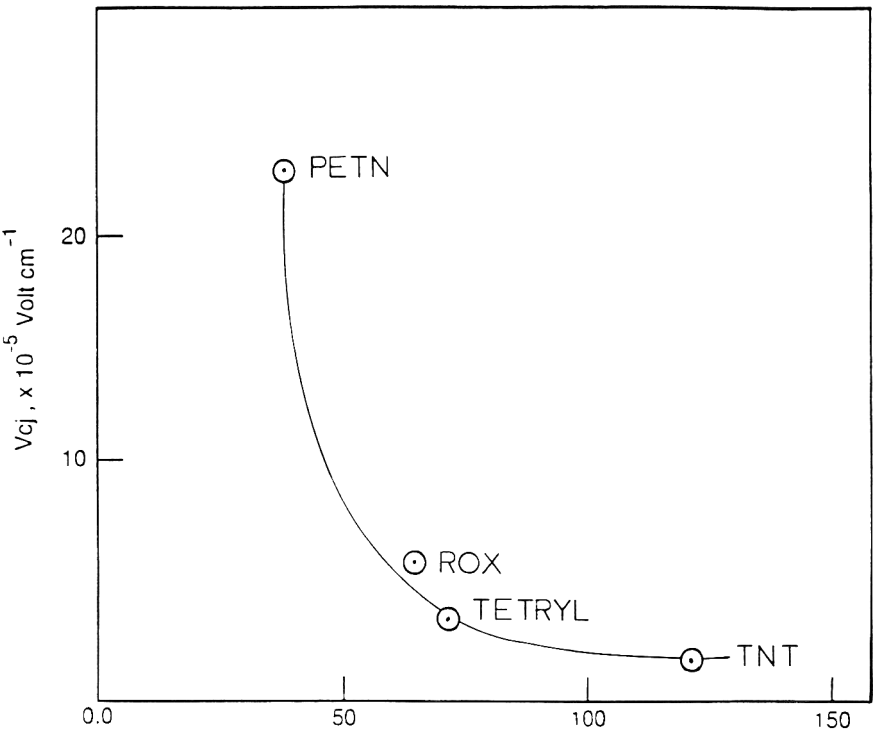

Fig. 1. Computed voltage at detonation pressure (V_{cj}) of high explosives vs. figure of insensitivity.

Table 2 presents the computed values of maximum static field developed under 1 kg load and at reported values of threshold pressure for the initiation of detonation. The experimental observation when extrapolated to the condition of detonation results in a very high field of the order of 10^5 volt/cm. The average values over 25 crystals at CJ (Chapman–Jouguet) pressures are 21.0×10^5, 5.31×10^5, 3.01×10^5 and 1.75×10^5 volt/cm for PETN, RDX, tetryl and TNT crystals respectively. Figure 1 shows the graphical relationship between the field generated at detonation pressure and the figure of insensitivity of the explosives.

4. Discussion

The results presented in Table 1 refer to the physical phenomenon, viz. piezoelectric charge development, dielectric constant and Young's modulus of the crystals along different directions. The charge development on PETN and TNT is "true piezoelectric" in nature which can be explained on the basis of crystal symmetry. PETN belongs to the tetragonal [12] class with symmetry $\bar{4}2\,m$ which falls under the piezoelectric category [13]. TNT crystallizes in

either orthorhombic or monoclinic structures. The orthorhombic class has point group *mm2*, which falls into the pyroelectric class. A pyroelectric crystal necessarily possesses piezoelectric properties, so TNT shows true piezoelectric charge. RDX is orthorhombic [14] with space group *mm*, and tetryl is monoclinic [15] with space group $2/m$; these do not fall under the "true piezoelectric" category. The charge developed on RDX and tetryl may be attributed to the deformation of quadrupoles which is observed in tensorial piezoelectric materials [16]. The variation in magnitude of the piezoelectric constant, on RDX and tetryl is possibly due to variation in structural imperfections in the crystals. The variation in Young's modulus of TNT along the direction perpendicular to (010) is attributed to the twinning nature of the crystals [13]. The anisotropic characteristics of the crystals are obvious from the data presented in Table 1. This characteristic of nonequivalent properties based on the direction of measurement results from crystallization in a system of low symmetry. Each molecule under investigation is of a complex structure, and the group orientation in space is even more complex. The nitro groups are linked to the parent molecules in different ways. PETN has four O–NO_2 groups; TNT has three C–NO_2 groups of an aromatic ring; RDX has three N–NO_2 groups in an alicyclic ring; and tetryl, the most complex of all has three C–NO_2 groups of an aromatic ring and an N–NO_2 group. However, physically, these explosives have certain common characteristics. They all form soft crystals of low crystal symmetry. The crystals have low dielectric constants in the range of 3 to 5, and high compressibility in relation to ionic crystals. They have high resistivity, which enables them to develop electrostatic charge. Under compressive force they all develop electrostatic charges which may be either true or tensorial piezoelectric in origin.

It has been observed from Table 1 for single crystals of PETN, RDX, tetryl and TNT that the directions perpendicular to (110), (001), (100) and (010) develop high magnitudes of piezoelectric charge respectively. Koch [17] and Garg et al. [18] observed higher values of velocity of detonation (VOD) along the same direction for PETN, RDX and TNT crystals. Dick [19] has observed that PETN crystals shocked in directions parallel to (110), (001), (101) and (100) give different run distances to detonation, which showed a dependence of shock initiation sensitivity on the crystal orientation. This indicates that charge development along different directions of an explosive crystal may be used as an index to ascertain its sensitivity along the direction. The reported values [20] of sensitivity to mechanical impact (F of I) for PETN, RDX, tetryl and TNT are 38, 64, 72 and 120 respectively (with sensitivity inversion with the value of F of I). It has been noted that the maximum static electric field developed across the crystals under 1 kg force decreases as the F of I increases (Table 2). Further, an interesting correlation of this static field with impact sensitivity was observed by extrapolating this result to the condition of detonation. At detonation pressure the crystal is supposed to undergo mechanical fracture because mechanical fracture occurs [21] even at 10^2 psi but the charge development, being an electrical phenomena, will require less time compared

to the fracture which is a mechanical process [22, 23]. So the field generated across the crystal in the initiating threshold pressure [24] should thus be an index of the sensitivity of the crystal. Thus the static field at threshold pressure shows an increase with the sensitivity of the crystal (Table 2).

The pressure which relates to the detonation pressure of explosives is the Chapman–Jouguet (CJ) pressure. Coleburn [25] reported the CJ pressure for PETN, RDX, tetryl in pressed form and TNT in cast form as 240, 284, 226 and 187 kbar, respectively. Figure 1 shows the graphical relation between the field generated at CJ pressure with the figure of insensitivity.

The extrapolated electrical field developed on these crystals at detonation pressure is of the order of 10^5 to 10^6 volt/cm, compared to 10^7 volt/cm reported by Maycock and Grahenstein [4] for the highly sensitive s-HMX crystal. It is worth noting that dielectric breakdown voltage of some explosive compositions [26] and explosives [27] are of the order of 10^5 volt/cm. Hence, the field generated on the explosive crystal at detonation is sufficiently high to cause dielectric breakdown in them. As a result, a large amount of heat is liberated and the condensed material is vaporized to an ionized condition. This dielectric breakdown in the predetonation stage is supported by the observation of Clay et al. [28], that the ionization is a major factor for initiation of detonation.

Acknowledgement

The authors present this paper in the memory of the late Dr S.R. Yoganarasimhan, Manager, INBRI, Bangalore for his inspiration and valuable guidance. We are thankful to Padmashree N.S. Venketasan, Director, ERDL Pune-411 008 for his kind permission to publish this paper.

References

1 G. Green Wood, Z. Krist, 96 (1937) 81.
2 H.H. Von Liecht and G. Scheverli, ISL-Saint Louis, 1973.
3 F. Baur, Recherche d'un Effect Piezoélectrique sur des Monocristan d'Hexogen et d'Octogen, ISL-Bericht N28/68.
4 J.N. Maycock and D.E. Grahenstein, Science, 152 (1966) 508.
5 K. Raha and J.S. Chhabra, Static charge development on explosives, Def. Sci. J., 41 (1991) 21.
6 K. Raha and J.S. Chhabra, Piezoelectricity in single crystal of pentaerythritol tetranitrate, Def. Sci. J., 41 (1991) 295.
7 P.V. Satyavratan and Kirti, Current Science, 152 (1972) 663.
8 R.D. Boddorf, Pit Quarry, (August) (1976) 64.
9 H.A. Hanna et al., Investigation of Static Electrical Phenomena in Lead Azide Handling, Mason & Hanger-Silas Mason Co. Inc., Burlington, Iowa, TR No. 98-A, (December 1967).
10 C.T. Davy, Explosives Pyrotechnics, 8 (12) (1975).
11 K. Raha, Studies on Single Crystals of High Explosives. PhD Thesis, Poona University, Pune-411 007, India, 1992?

12 C.E. Henry Brown and G. Rotter, Science of Explosives, Part II, Ministry of Supply, London, 1956, p. 1038.
13 W.S. Cady, Piezoelectricity, Dover Publ., New York, 1964, Vol. I, p. 19.
14 L.A. Burkardt and J.H. Bryden, Acta Crystallogr., 7 (1954) 135.
15 W.D. Cady, Acta Cryst., 23 (1967) 601.
16 W.G. Cady, Piezoelectricity, Dover Pub., New York, 1964, Vol. II, p. 711.
17 H.W. Koch, Einführung Symposium, Institute für Chemisch-technische Untersuchungen (CTI), Vol. 13, 1973, p. 478.
18 D.D. Garg et al., Report 23/75, ERDL, Pune-411 021, India (1975).
19 J.J. Dick, Appl. Phys. Lett., 44 (1984) 859.
20 M.A. Cook, The Science of Explosives, Reinhold, New York, 1963, p. 179.
21 W. Elban and R. Armstrong, In: Proc. 7th Symp. (Int.) on Detonation, 1981, p. 976.
22 H. Kolosky, Stress Wave in Solids, Clarendon Press, Oxford, 1953, p. 183.
23 A.A. Vorob'ev and E.K. Zavadovskaya, Docklady Akad. Nauk SSSR, 81 (1951) 375.
24 J. Roth, Fifth Int. Symp. on Detonation, Pasadena, CA, August 18–21, 1970, p. 219.
25 N.L. Coleburn, Chapman–Jouguet Pressure of Several Pure and Mixed Explosives, NOL TR64-58, United States Naval Ordnance Laboratory, White Oak, MD, 1964.
26 T.F. Basil and E.S. Oliver, Encyclopedia of Explosives and Related Items, Picatinny Arsenal, Dover, NJ, 1972, Vol. 5. P.D. 1221.
27 M.A. Melnikov and N.P. Volkov, Izv. Tomsk Politekh. Imt., 180 (1971) 93.
28 R.D. Clay, M.A. Cook, R.T. Keyes, O.K. Shupe and L.L. Udy, Third Symp. on Detonation. Naval Ordnance Laboratory, White Oak, MD, Sept. 26–28, 1960, p. 150.

Journal of Hazardous Materials, 34 (1993) 393–399
Elsevier Science Publishers B.V., Amsterdam

Book Reviews

Drinking Water Advisory: Pesticides, by U.S. Environmental Protection Agency, Office of Drinking Water Health Advisories, Lewis Publishers, Chelsea, MI, 1989, ISBN 0-87371-235-8, 819 pp., $95,00.

The U.S. EPA Office of Drinking Water Health Advisory Program was begun to provide information and guidance to individuals or agencies concerned with potential risk from drinking water contraminants for which no national regulations currently exist. The health advisories found in this book were prepared for pesticide-based contaminants that meet two criteria: (1) the contaminant has the potential to cause adverse effects in exposed humans, and (2) the contaminant is either known to occur or might reasonably be expected to occur in drinking water supplies. The health advisory for each pesticide contains information on the nature of the adverse health effects associated with the contaminant and the concentration of the contraminant that would not be anticipated to cause an adverse effect following periods of exposure. In addition, the health advisory summarizes information on available analytical methods and treatment techniques for the contaminant.

The following data are given for 52 different pesticides:

- General information and properties: CAS No., structural formulas, synonyms, uses, properties, occurrence, and environmental fate.
- Pharmokinetics: absorption, distribution, metabolism, and excretion.
- Health effects: humans and animals.
- Quantification of toxicological effects: one-day health advisory, ten-day health advisory, longer-term health advisory, lifetime health advisory, and evaluation of carcinogenic potential.
- Other criteria, guidance, and standards.
- Analytical methods.
- Treatment technologies.
- References.

GARY F. BENNETT

Ozone in Water Treatment: Application and Engineering, edited by B. Langlais, D.A. Reckhow and D.R. Brink, Cooperative Research Report: American Water Works Association Research Foundation and Compagnie Général des Eaux, Lewis Publishers, Chelsea, MI, 1991, ISBN 0-87374-471-1, 569 pp. ($8\frac{1}{2} \times 11$ in. format), $69.95.

The AWWA and Compagnie Général des Eaux, with the assistance of 35 expert authors collaborated to produce a state-of-the-art scientific manual on

the application of ozone to drinking water treatment. As more concern is expressed about by-products of chlorine treatment (e.g. trihalomethanes) the use of ozone for water disinfection will increase.

This book was written for practicing engineers, water treatment plant managers, and others interested in ozonization. The purpose of this book is to provide guidance on the various applications of ozone, and appropriate system design and operation.

Chapter I provides a historical introduction to ozone use, tracing its roots to Merilens' recognition in 1886 that ozone could disinfect polluted water. Ozone's use in the United States and Europe is discussed.

Chaper II is devoted to the review of aqueous ozone chemistry, toxicology, analytical methods, and the physics of ozone production and gas transfer. Chapter III provides a bridge between fundamental chemistry and physics (Chaper II) and the specifics of design (Chaper IV). In this chapter, 10 different ozone applications are discussed in detail; e.g. iron and manganese removal, taste and odor removal, taste and odor control, etc.

Chater IV presents the basics of ozone system design. Included are performance of treatibility studies, ozone generation, contacting and diffusion, instrumentation, ozone destruction, corrosion consideration, system retrofit, and performance evaluation. Aspects of system operation are discussed in Chapter V. Included are principles of operation, reliability, maintenance, training and safety.

Chapter VI presents information on economics of ozone system design, construction and operation. The emerging process of ozonization combined with hydrogen peroxide and ultraviolet light are briefly discussed.

The book is a comprehensive compilation of the state-of-the-art of ozone technology as applied to drinking water production. It is a monumental work that will be the standard of the field for years to come.

GARY F. BENNETT

Nitrogen Oxides Control Technology Fact Book, compiled by L.L. Sloss, A.K. Hjalmarsson, H.N. Suud, L.M. Campbell, D.K. Stone, G.S. Shareef, T. Emmel, M. Malbodi, C.D. Livengood and J. Markussen, Noyes Data Corporation, Park Ridge, NJ, 1992, ISBN 0-8155-1294-5, 635 pp., $86.00.

This book describes technologies for the control of nitrogen oxides emissions, primarily from the combustion of coal. More than 115 control systems are documented and a section on control costs is included.

The control systems discussed cover NO_X reduction during combustion by flue gas denitrification, and by combined denitrification and desulfurization. NO_X control systems commercially available from various manufacturers and those currently under development by private or governmental research

organizations worldwide are presented. For each system, the following data are given:

- Information on the system
- Process application
- Pollution reduction capability
- System diagrams (if available)
- Supplier/manufacturer

The book is, as many of the Noyes Data books are, a combination of several reports prepared for government agencies (in this case: U.S. EPA, DOE, and IEA Coal Research):

- Systems for Controlling NO_X from Coal Combusion
- Sourcebook: NO_X Control Technology
- Recent Developments in Combined Control of SO_2 and NO_2
- Combined NO_2/SO_2 Removal in Spray-Dryer FGD System
- Opportunities for Integrated Pollution Control Retrofits
- Retrofit Costs for SO_2 and NO_X Control Options at 200 Coal-Fired Plants

GARY F. BENNETT

Hazardous and Industrial Wastes: Proceedings of the 24th Mid-Atlantic Industrial Waste Conference, edited by B.E. Reed and W.A. Sack, Technomic Publishing, Lancaster, PA, 1992, ISBN 0-87762-974-9, 759 pp. $85.00.

Sponsored by 14 universities, this annual conference was held at West Virginia University in Morgantown, West Virginia in July 1992. These proceedings contain 66 of the 80 papers presented at this conference.

Major topics (session theme) and the number of papers published in each were:

Pollution prevention/waste minimization – 6
Groundwater flow – 3
Sludge treatment – 3
Issues – 3
Treatment technology – 20
Site remediation – 21
Waste management – 3
Energy from wastes – 4
Solids disposal – 3

Given the list above it is obvious the papers span a wide range of topics, from laboratory studies to proven technology; from theory to established practice; from a student design contest problem to expert systems for waste treatment.

The papers were photoreproduced yielding variable type fonts. An index is provided for the current volume as well as for the proceedings from the preceding five conferences.

Many (14) of the papers presented at the conference were not published in the proceedings, the editors noting they were unavailable at press time. Although the title and authors of each nonappearing paper was given, sufficient data were not given to allow an interested reader to request a copy from the author. Perhaps the editors could give these data next time.

GARY F. BENNETT

Ethel Browning's Toxicity and Metabolism of Industrial Solvents, 2nd edn., Vol. 3. Alcohols and Esters, edited by R.G. Thurman and F.C. Kaufmann, Elsevier, Amsterdam, 1992, ISBN 0-444-81317-9, xxxviii + 394 pp., $228.50/Dfl. 400.00.

The initial edition of Ethel Browning's Handbook of *Toxicity and Metabolism of Industrial Solvents* was published in 1965. In that pioneering work, Browning discussed both the properties, toxicology, and metabolism mechanisms of toxicity of solvents. This new edition extends that work by emphasizing mechanism of toxicity in an attempt to understand the toxic effects produced by chemicals — but this time the data are published in four volumes (not just one), each volume being devoted to a different group of compounds.

In this (the third volume of the series), the authors have integrated the data, interpreted the results of numerous studies and have provided detailed lists of references to assist use of the original literature.

As noted above, both alcohol and esters are discussed in Volume 3. In the former category, 24 different alcohols (e.g. methanol, ethanol, butanol, etc.) are discussed; in the latter category, 22 different esters (e.g. ethyl acetate, butyl acetate, propyl acetate) are discussed.

Separate chapers (46 in all) are devoted to each chemical or chemical groups. And each chapter follows a standard format with information grouped under the following headings:

- Physical properties
- Economy, sources and use: production, and industrial uses.
- Biochemistry: estimation, and metabolism.
- Toxicology: animal, human, and carcinogenicity and mutagenicity.
- References

As with any multi-authored text, the emphasis given to any one of the above categories is quite varied. As a chemical engineer, I was more interested in the production and industrial use sub-chapters — although I realize they are not the prime focus of the text. The various chemicals, the amount of space devoted to this topic ranged from a few lines to more than a page.

GARY F. BENNETT

State Asbestos Programs. Related to the Asbestos Hazard Emergency Response Act. A Survey of State Laws and Regulations, September 1992. Compiled by D. Farquhar, published by National Conference of State Legislatures, 1560 Broadway, Denver, CO 80202, 1992, ISBN-1-55516-494-3, 358 pp. (paperback), $65.00.

This most useful book results from the fifth survey conducted by the National Conference of State Legislatures in the individual states with respect to the policies of each toward asbestos programs. For those readers who are in a hurry, there are charts in the front of the book outlining the requirements of each state toward inspections, management plans, accreditation and training programs for asbestos removal or remediation, comparisons of U.S. EPA and state regulations, abatement standards, enforcement, monitoring/sampling, funding and other programs in the asbestos area. For more thorough study, there is a section for each state in which the policies/requirements outlined in the preliminary charts are discussed in detail. This portion also has tables on certification programs in each state, a necessity for any organization interested in working on asbestos removal. The material also allows a ready comparison of regulations in any one state versus those in others. Some of the differences between the states are summarized briefly in the "Survey Summary" at the beginning of the book. This volume should be required reading for all organizations and individuals involved in asbestos programs. Another useful item which adds to the value of the book is a listing of the knowledgeable individuals in each state who furnished the information. Plans are to update the volume in 1994 if funding is then available.

ELIZABETH K. WEISBURGER

Environmental Engineering Dictionary, by C.C. Lee, Government Institutes, Rockville, MD, 1992, ISBN 0-86587-328-3, 462 pp. (hardcover), $88.00.

This book is a comprehensive second edition dictionary containing definitions of more than 12,000 technical and regulatory engineering terms used in pollution control technologies, monitoring, risk assessment, sampling and analyses, quality control, and environmental engineering and science. Origins of many of the definitions are provided; approximately 300 references are given as sources of the definitions. Over 20 pages of acronyms (exceeding 1200 entries) are given.

The definitions (at least the ones I need) are excellent and the book should well serve the information needs of both scientists and laymen.

GARY F. BENNETT

In Situ Bioreclamation: Applications and Investigations for Hydrocarbon and Contaminated Site Remediation, edited by R.E. Hinchee and R.T. Olfenbuttel, Butterworth-Heinemann, Stoneham, MA, 1991, ISBN 0-7506-9301-0, 623 pp. (includes following book), $150.00.

This book is one of two volumes (the other is *On-Site Bioreclamation: Processes for Xenobiotic and Hydrocarbon Treatment*) that resulted from an international symposium held in San Diego, California, in March 1991.

The contributions are found in two different formats: articles and technical contributions. Articles (23 in number) represent (according to the editors) a sustantial technical contribution; technical notes (22 in number) are brief technology descriptions or reports of preliminary or less substantial studies. All papers were peer reviewed.

Obviously such a conference covers, by design, a technological wide area. Some of the topics reported include:

- European bioreclamation practices
- Fuel-contaminated soils bioremediation
- Oxygen delivery; hydrogen peroxide sources
- BTEX biodegradation
- Bioventing
- Soil vapor extraction
- Coke oven plant site bioremediation
- Modeling bioremediation
- Metal polluted soils decontamination

The papers range from basic research to engineering design and they cover a wide variety of contaminants (benzene, toluene, ethylbenzene, hydrocarbons, metals, fossil fuel, PAHs, oil, aromatic hydrocarbons and jet fuel): Not neglected is theory, especially numerical modeling.

Unlike most conference proceedings, this book is typeset and contains an extensive index.

GARY F. BENNETT

On-Site Bioreclamation: Processes for Xenobiotic and Hydrocarbon Treatment, edited by R.E. Hinchee and R.T. Olfenbuttel, Butterworth-Heinemann, Stoneham, MA, ISBN 0-7506-9302-9, 1991, 539 pp. (includes above book), $150.00.

This second volume of conference proceedings contains 22 articles and 13 technical notes also covering a wide range of topics as illustrated below.

- U.S. EPA bioremediation program
- Trichloroethylene biodegradation
- Fixed film reactors
- Slurring phase bioremediation
- Packed column bioreactor for air stripper off-gas
- Anaerobic treatment
- PCB degradability
- Phenol biosensors

GARY F. BENNETT

Chemical Oxidation: Technologies for the Nineties, by W.W. Eckenfelder, Jr., A.R. Bowers and J.A. Roth, Technomic Publishing, Lancaster, PA, 1991, ISBN 0-87762-895-5, 313 pp., $65.00.

In the preface the authors write:

"New regulations governing the discharge of toxic pollutants has focussed increased emphasis on physical-chemical technologies which can treat these pollutants in a cost-effective manner. Foremost among these technologies is chemical oxidation.

While chemical oxidation technology has been known and used for many years, the application to wastewater treatment is relatively recent."

Recent this technology is and needed too. More stringent U.S. EPA discharge guidelines for both direct discharges (to bodies of water) and indirect discharges (to sewers), are compelling industry to seek cleanup processes far more efficient than historically used biological systems.

The volume contains 23 papers presented at symposium held at Vanderbilt University in February 1991. They cover a wide range of topics from very basic research to operating system description.

Oxidants discussed include: hydrogen peroxide, ozone, chlorine dioxide, and potassium permanganate. Chemicals destroyed include NO_X, phenols, and other aromatics in the following media: ground water, soil, and industrial wastewater, respectively.

Taken together, the published papers present an excellent overview of the field. The wide variety of papers are certainly up-to-date, generally well written (with the minor exception that some papers could have been improved by editing), and comprehensive. Anyone seriousy interested in the field of chemical oxidation will want to obtain these proceedings — and the successor volume, which I hope will follow a 1993 conference on the same topic.

GARY F. BENNETT

Journal of Hazardous Materials, 34 (1993) 401–402
Elsevier Science Publishers B.V., Amsterdam

Announcement

International Symposium on Remediation and Restoration of Radioactive-contaminated Sites in Europe, 11–15 October 1993, Antwerp, Belgium

Aims and Scope

During the last fifty years, both in Europe and elsewhere, extensive industrial use has been made of radioactive and fissile materials. Large scale nuclear facilities, for civil and defence uses, have been developed, some of which have given rise to significant radioactive contamination of the environment.

Some of these facilities have since ceased to operate and they together with the sites on which they were located, remain under various degrees of surveillance.

There is a need to compile an inventory of contaminated sites in Europe, in terms of the extent, level and nature of the contamination. The need for remedial or restoration work, in order to return these sites to uncontrolled use, should be examined

The main objectives of the present symposium are, therefore, to identify the major contaminated sites in Europe, to assess their environmental impact and to examine possible remediation possibilities and plans. To reach these objectives the following topics will be covered:

1. Identification of the major contaminated sites in Europe (and the Asian part of the CIS). Such sites may include abandoned uranium mining areas, areas contaminated with enhanced levels of natural radioactive material from industrial processes such as radium refineries, areas affected by nuclear accidents, nuclear weapon testing, operation of and discharges from nuclear facilities used for civil and/or defence purposes.
2. Case studies for a limited number of sites of interest. These will be largely restricted to European sites but experience from elsewhere will be addressed where this serves to elucidate the issues to be addressed.
3. Radiation protection concepts and criteria applicable to the remediation and restoration of contaminated sites. This includes the implementation of the optimization principle, both generally and for specific applications.
4. Consideration of social and economic aspects, in particular risk perception and other less tangible factors.
5. Methodologies for environmental impact and risk assessment including problems of measurement and of dose reconstruction.

6. Overview of practicable remediation and restoration techniques.
7. International collaboration in this field.

Scientific Programme Committee
A. Aarkrog, Denmark
J. Barescut, France
P. Carboneras, Spain
E. Ettenhuber, Germany
R. Haworth, United Kingdom
C. Huyskens, Netherlands
Y. Tsaturov, Russia
N. Kelly, CEC, DG XII
A. Janssens, CEC, DG XI
K. Schaller, CEC, DG XI

Organizing Committee
Y. Tsaturov, State Committee of the Russian Federation on Chernobyl Affairs
F. Luykx, CEC-DG XI
J. Sinnaeve, CEC-DG XII
P. Govserts, SCK-CEN Mol, Belgium

Venue
The symposium will be held from 11 to 15 October, 1993, in the Hilton Hotel, Graenplaats, Antwerp, Belgium

Working Languages
The working languages of the synposium will be English and Russian; simultaneous translation will be provided

Further Information
F. Luykx
Commission of the European Communities
DG XI
Wagner Building C-354
L-2920 LUXEMBOURG

Tel: (352) 4301 36391
Telex: 3423 comeur lu
Fax: (352) 4301 36280

Author Index Volume 34

Arya, S.P.S., 271

Castro, I.P., 271
Chen, J.M., 51
Chhabra, J.S., 385
Constant, W.D., 313
Cundy, V.A., 1

Davis, A.P., 51
De Faveri, D.M., 69
Desbordes, D., 123

Glažar, S.A., 199

Hao, O.J., 51
Hill, D.O., 245
Hillger, R.W., 335
Hjertager, B.H., 173

Imide, N.E., 81

Jakway, A.L., 1, 31

Kornhauser, A., 199
Kumar, A., 271
Kuo, C.H., 245

Lannoy, A., 123, 151
Leger, C.B., 1
Leyer, J.C., 123
Li, C., 295

Maloney, S.W., 51
Maresca, Jr., J.W., 335
Montestruc, A.N., 1, 31
Musar, A., 199

Okrent, D., 363
Olorunmaiye, J.A., 81
Owens, W.D., 1, 31

Pastorino, R., 69
Phull, K.K., 51

Raha, K., 385
Reible, D.D., 313
Rhee, S.-W., 313

Saint-Cloud, J.P., 123
Starr, J.W., 335
Sterling, A.M., 1, 31
Snyder, W.H., 271

Tafuri, A.N., 335
Tang, M.-J., 225

Van den Berg, A.C., 151
Vidili, A., 69
Voudrias, E.A., 295

Wise, R.F., 335

Xing, L., 363

Yang, G.C.C., 217, 235

Zhang, G.-S., 225
Zheng, Y., 245
Zonato, C., 69

Contents Volume 34

Vol. 34, No. 1

Field-scale rotary kiln incineration of batch loaded toluene/sorbent. I. Data analysis and bed motion considerations
C.B. Leger, V.A. Cundy, A.M. Sterling, A.N. Montestruc, A.L. Jakway (Baton Rouge, LA, USA) and W.D. Owens (Salt Lake City, UT, USA) 1

Field-scale rotary kiln incineration of batch loaded toluene/sorbent. II. Mass balances, evolution rates, and bed motion comparisons
C.B. Leger, C.A. Cook, V.A. Cundy, A.M. Sterling, A.N. Montestruc, A.L. Jakway (Baton Rouge, LA, USA) and W.D. Owens (Salt Lake City, UT, USA) 31

Factors affecting wet air oxidation of TNT red water: Rate studies
O.J. Hao, K.K. Phull, J.M. Chen, A.P. Davis (College Park, MD, USA) and S.W. Maloney (Champaign, IL, USA) 51

Plume rise of smoke coming from free burning fires
C. Zonato (Venice, Italy), A. Vidili (Milan, Italy), R. Pastorino (Genova, Italy) and D.M. De Faveri (Venice, Italy) 69

Computation of natural gas pipeline rupture problems using the method of characteristics
J.A. Olorunmaiye (Ilorin, Nigeria) and N.E. Imide (Bauchi, Nigeria) 81

Book Reviews 99
Announcements 109
Instructions to Authors 113

Vol. 34, No. 2

Editorial 121

Unconfined deflagrative explosion without turbulence: Experiment and model
J.C. Leyer, D. Desbordes, J.P. Saint-Cloud (Poitiers, France) and A. Lannoy (Saint-Denis, France) 123

Methods for vapour cloud explosion blast modelling
A.C. van den Berg (Rijswijk, The Netherlands) and A. Lannoy (Saint-Denis, France) 151

Review
Computer modelling of turbulent gas explosions in complex 2D and 3D geometries
B.H. Hjertager (Porsgrunn, Norway) 173

Information support for the incineration of chemical waste in cement kilns
S.A. Glažar, A. Kornhauser and A. Musar (Ljubljana, Slovenia) 199

Durability study of a solidified mercury-containing sludge
G.C.C. Yang (Kaohsiung, Taiwan) 217

The investigation of a devastating accident – An accidental explosion of 40 tons of TNT
G.-S. Zhang and M.-J. Tang (Beijing, People's Republic of China) 225

Environmental threats of discarded picture tubes and printed circuit boards
G.C.C. Yang (Kaohsiung, Taiwan) 235

Destruction of cresols by chemical oxidation
Y. Zheng, D.O. Hill and C.H. Kuo (Mississippi State, MS, USA) 245

Book Reviews 261

Vol. 34, No. 3

Removal of slightly heavy gases from a valley by crosswinds
I.P. Castro (Guildford, UK), A. Kumar (Cary, NC, USA), W.H. Snyder (Research Triangle Park, NC, USA) and S. Pal S. Arya (Raleigh, NC, USA) 271

Benzene vapor transport in unsaturated soil: Adequacy of the diffusion equation
E.A. Voudrias and C. Li (Atlanta, GA, USA) 295

Stochastic modeling of flow and transport in deep-well injection disposal systems
S.-W. Rhee, D.D. Reible and W.D. Constant (Baton Rouge, LA, USA) 313

Evaluation of volumetric leak detection systems for large underground tanks
J.W. Maresca, Jr., J.W. Starr (Mountain View, CA, USA), R.F. Wise, R.W. Hillger and A.N. Tafuri (Edison, NJ, USA) 335

Future risk from a hypothesized RCRA site disposing of carcinogenic metals should a loss of societal memory occur
D. Okrent and L. Xing (Los Angeles, CA, USA) 363

Static charge development and impact sensitivity of high explosives
K. Raha and J.S. Chhabra (Pune, India) 385

Book Reviews 393
Announcement 401
Author Index Volume 34 403
Contents Volume 34 405

Nuclear Materials for Fission Reactors

Proceedings of Symposium E , E-MRS Fall Conference,
Strasbourg, France, 4-7 November 1991

edited by **H. Matzke** *and* **G. Schumacher**

Reprinted from the Journal of Nuclear Materials, Volume 188

European Materials Research Society Symposia Proceedings Volume 28

This volume brings together 47 papers from scientists involved in the fabrication of new nuclear fuels, in basic research of nuclear materials, their application and technology as well as in computer codes and modelling of fuel behaviour. The main emphasis is on progress in the development of non-oxide fuels besides reporting advances in the more conventional oxide fuels. The two currently performed large reactor safety programmes CORA and PHEBUS-FP are described in invited lectures. The contributions review basic property measurements, as well as the present state of fuel performance modelling. The performance of today's nuclear fuel, hence UO2, at high burnup is also reviewed with particular emphasis on the recently observed phenomenon of grain subdivision in the cold part of the oxide fuel at high burnup, the so-called "rim" effect. The papers will provide a useful treatise of views, ideas and new results for all those scientists and engineers involved in the specific questions of current nuclear waste management.

Abbreviated contents:
Sections: I. Fuel Fabrication and Performance. Irradiation behaviour of metallic fast reactor fuels *(R.G. Pahl et al.)*. Fission product behaviour in Phenix fuel pins at high burnup *(M. Tourasse et al.)*. Concerning the microstructure changes that occur at the surface of UO_2 pellets on irradiation to high burnup *(C.T. Walker et al.)*. Fuel performance under normal PWR conditions: A review of relevant experimental results and models *(M. Charles, C. Lemaignan)*. **II. Reactor Safety.** The Phebus fission product project (P. von der Hardt). Information on the evolution of severe LWR fuel element damage obtained in the CORA programme *(G. Schanz et al.)*. Transient fuel behaviour of preirradiatec PWR fuels under reactivity initiated accident conditions *(T. Fujishiro et al.)*. On the kinetcs of UO_2 interaction with molten Zircaloy at high temperatures *(M.S. Veshchunov. A.M. Volchek)*.
III. Basic Properties of Nuclear Materials. Neutron irradiation effects in boron carbides: Evolution of microstructure and thermal properties *(K. Froment et al.)*. Thermal conductivity of SIMFUEL *(P.G. Lucuta et al.)*. Vaporization behaviour of uranium-plutonium mixed nitride *(Y. Suzuki et al.)*. Study of the oxidation of a stainless steel under BWR conditions by advanced analytical techniques *(C. Degueldre et al.)*. Structural analysis of oxide scales grown on zirconium alloys in autoclaves and in a PWR *(H. Blank et al.)*.
IV. Modelling of Fuel Performance. TRANSURANUS: A fuel rod analysis code ready for use *(K. Lassmann)*. Mechanistic model of fission gas behaviour in metallic fuel *(Y. Tsuboi et al.)*. Development of the thermal behaviour analysis code DIRAD and the fuel design procedure for LMFBR *(N. Nakae et al.)*. Author index. Subject index.

1992 x + 348 pages
Price: US $ 219.00 / Dfl. 350.00
ISBN 0-444-89571-X

Elsevier Science Publishers
P.O. Box 103, 1000 AC Amsterdam
The Netherlands
in the USA/Canada:
Attn: Judy Weislogel, P.O. Box 945
Madison Square Station
New York, NY 10160-0757

The Dutch Guilder (Dfl.) price is definitive. US$ price is subject to exchange rate fluctuations.

ELSEVIER
SCIENCE PUBLISHERS

SUBMISSION OF PAPERS

Submission of a manuscript implies that it is not under consideration for publication elsewhere and further that, with the exception of review papers, original work not previously published is being presented.

Papers should be submitted to Dr G.F. Bennett, Department of Chemical Engineering, University of Toledo, 2801 W. Bancroft Street, Toledo, OH 43606, U.S.A. or Dr. R.E. Britter, Department of Engineering, University of Cambridge, Cambridge CB2 1PZ, Great Britain. Authors in the Far East should submit papers to Dr. T. Yoshida, Chemical Engineering Laboratory, Department of Mechanical Engineering, Faculty of Engineering, Hosei University, 7-2 Kajino-cho 3-chome, Koganei-shi, Tokyo 184, Japan.

MANUSCRIPT PREPARATION

Three copies of the manuscript (one on floppy disk, when possible) should be submitted in double-spaced typing on pages of uniform size with a wide margin on the left. The top copy should bear the name and the full postal address and fax number of the person to whom the proofs are to be sent. An abstract of 100–200 words is required.

References should be numbered consecutively throughout the text and collected together in a reference list at the end of the paper. Journal titles should be abbreviated. The abbreviated title should be followed by the volume number, year (in parentheses), and page number.

ILLUSTRATIONS

Line drawings should be in a form suitable for reproduction, drawn in Indian ink on drawing paper. They should preferably all require the same degree of reduction, and should be submitted on paper of the same size as, or smaller than, the main text, to prevent damage in transit. Photographs should be submitted as clear black-and-white prints on glossy paper. Each illustration must be clearly numbered. Colour illustrations can be reproduced at the author's expense.

Legends to the illustrations must be submitted in a separate list.

All tables and illustrations should be numbered consecutively and separately throughout the paper.

LANGUAGE

The principal language of the journal is English, but papers in French and German will be published.

PROOFS

Authors will receive page proofs, which they are requested to correct and return as soon as possible. No new material may be inserted in the text at the time of proofreading.

REPRINTS

A total of 50 reprints of each paper will be supplied free of charge to the principal author. Additional copies can be ordered at prices shown on the reprint order form which accompanies the proofs.

A pamphlet containing detailed instructions on the preparation of manuscripts for JOURNAL OF HAZARDOUS MATERIALS may be obtained from the publishers.

0304-3894/93/$06.00

This issue is printed on acid-free paper.

PRINTED IN THE NETHERLANDS

VOL. 34, NO. 3 AUGUST 1993

JOURNAL OF HAZARDOUS MATERIALS

CONTENTS

Removal of slightly heavy gases from a valley by crosswinds
I.P. Castro (Guildford, UK), A. Kumar (Cary, NC, USA), W.H. Snyder (Research Triangle Park, NC, USA) and S. Pal S. Arya (Raleigh, NC, USA) 271

Benzene vapor transport in unsaturated soil: Adequacy of the diffusion equation
E.A. Voudrias and C. Li (Atlanta, GA, USA) 295

Stochastic modeling of flow and transport in deep-well injection disposal systems
S.-W. Rhee, D.D. Reible and W.D. Constant (Baton Rouge, LA, USA) 313

Evaluation of volumetric leak detection systems for large underground tanks
J.W. Maresca, Jr., J.W. Starr (Mountain View, CA, USA), R.F. Wise, R.W. Hillger and A.N. Tafuri (Edison, NJ, USA) 335

Future risk from a hypothesized RCRA site disposing of carcinogenic metals should a loss of societal memory occur
D.Okrent and L. Xing (Los Angeles, CA, USA) 363

Static charge development and impact sensitivity of high explosives
K. Raha and J.S. Chhabra (Pune, India) 385

Book Reviews 393
Announcement 401
Author Index Volume 34 403
Contents Volume 34 405

SUBSCRIPTION INFORMATION

1993 Subscription covers volumes 32–35. Subscription orders can be entered only by calendar year (Jan.–Dec.) and should be sent to: Elsevier Science Publishers B.V., Journals Department, P.O. Box 211, 1000 AE Amsterdam, The Netherlands, Tel. (020) 5803642, Telex 18582 ESPA NL, Fax (020) 5803598, or to your usual subscription agent. Claims for missing issues will be honoured, free of charge, within six months after publication date of the issue. All back volumes are available. Our rate (postage, package and handling) charge includes surface delivery of all issues, except to the following countries where air delivery via S.A.L. (Surface Air Lifted) mail is ensured: Argentina, Australia, Brazil, Canada, Hong Kong, India, Israel, Japan, Malaysia, Mexico, New Zealand, Pakistan, P.R. China, Singapore, South Africa, South Korea, Taiwan, Thailand, and the U.S.A. For Japan, air delivery by S.A.L. requires 25% additional charge; for all other countries airmail and S.A.L. charges are available upon request. Customers in the U.S.A. and Canada wishing information on this and other Elsevier journals, please contact Journal Information Center, Elsevier Science Publishing Co., Inc., 655 Avenue of the Americas, New York, NY 10010, Tel. (212) 633-3750, Fax (212) 633-3764.

0304-3894(199308)34:3;1-6